

Borehole radar for oil production monitoring

Borehole radar for oil production monitoring

PROEFSCHRIFT

ter verkrijging van de graad van doctor
aan de Technische Universiteit Delft,
op gezag van de Rector Magnificus prof. ir. K.C.A.M. Luyben,
voorzitter van het College voor Promoties,
in het openbaar te verdedigen op woensdag 25 januari 2012 om 12:30 uur

door Mattia MIORALI

Master of Science in Geology,
Università degli Studi Milano Bicocca,
geboren te Milan, Italy.

Dit proefschrift is goedgekeurd door de promotoren:

Prof. dr. ir. R.J. Arts

Prof. dr. ir. E.C. Slob

Samenstelling promotiecommissie:

Rector Magnificus,	Technische Universiteit Delft, voorzitter
Prof. dr. ir. R.J. Arts,	Technische Universiteit Delft, promotor
Prof. dr. ir. E.C. Slob,	Technische Universiteit Delft, promotor
Prof. dr. ir. W. Mulder,	Technische Universiteit Delft
Prof. ir. C.P.J.W. van Kruijsdik,	Technische Universiteit Delft
Prof. dr. S. Lambot,	Université Catholique de Louvain
Prof. dr. ir. J. van der Kruk,	RWTH Aachen University
Dr. A. Giannopoulos,	University of Edinburgh

This research was carried out within the context of the ISAPP Knowledge Center. ISAPP - Integrated System Approach Petroleum Production - is a co-operation project of Shell International Exploration and Production BV, TU Delft, and Netherlands Organization for Applied Research TNO.

ISBN 978-90-8570-967-1

Copyright © 2012 by M. Miorali.

All rights reserved. No part of the material protected by this copyright notice may be reproduced or utilized in any form or by any means, electronic or mechanical, including photocopying, recording or by any information storage and retrieval system, without written permission from the copyright owner.

Printed in the Netherlands

Dedicated to my family

Contents

1	Introduction	1
1.1	An introduction to petroleum exploration and production . . .	1
1.2	Closed-loop reservoir management	3
1.3	Overview of smart wells technology	5
1.3.1	Inflow control technology	5
1.3.2	Monitoring sensors	6
1.4	Ground Penetrating Radar	10
1.5	Problem definition	11
1.6	Research objective and outline	12
2	EM wave in oilfield environment	15
2.1	Introduction	15
2.2	Wave propagation	17
2.2.1	EM properties of rocks	19
2.3	Reflectivity of an interface	22
2.4	System Performance of a borehole radar system	24
2.5	SAGD model	25
2.5.1	Wellbore casing	26
2.5.2	Reservoir scenarios	29
2.6	Conclusions	29
3	Coupling reservoir to EM and fluid flow modeling	33
3.1	Introduction	33
3.2	Numerical experiment	34
3.3	Results and discussion	37
3.4	Conclusions	39
4	GPR monitoring of oil displacement by waterflooding: A laboratory study	43
4.1	Introduction	43

4.2	Material and methods	44
4.2.1	Experimental set up	44
4.2.2	Monitoring systems	45
4.2.3	EM Forward and Inverse Modeling	46
4.2.4	Water flooding experiments	48
4.3	Results and Discussion	49
4.3.1	Off-ground radar inversions	49
4.3.2	Impedance measurements	50
4.3.3	Water flooding monitoring	53
4.4	Conclusions	62
5	Uncertainty in GPR	65
5.1	Introduction	65
5.2	Material and Methods	66
5.2.1	EM Forward and Inverse Modeling	66
5.2.2	GPR equipment	67
5.2.3	Antenna transfer function determination	68
5.2.4	Uncertainties in the calibration method	69
5.2.5	Measured and computed Green's functions	70
5.2.6	Inversion experiments	73
5.3	Results and Discussion	73
5.3.1	Uncertainties in the calibration method	73
5.3.2	Measured and computed Green's functions	76
5.3.3	Inversion results	76
5.4	Conclusion	82
6	Conclusions	83
6.1	Recommendations	85
	Bibliography	87
	Summary	101
	Samenvatting	104
	Acknowledgements	107
	About the authour	109

Chapter 1

Introduction

The central theme in this thesis is an evaluation of the potential of radar as a monitoring tool in a borehole environment to support the optimal production of oil through closed-loop control strategies. In this introductory chapter an overview of the most promising applications and production settings will be provided. This includes general background information on oil exploration and production and an explanation of the closed-loop reservoir management concept, that aims at maximizing the oil production through smart control strategies. Particular emphasis is given to the description of smart well technology, since this would be the operating environment of the proposed borehole radar tool. Both measurement and control equipment as currently available in smart wells and still at a research and development stage are considered. More widely the main principles and most common applications of ground penetrating radar technology will be discussed with an outlook to the potential applications in the oil industry. Finally the research objectives and the structure of this thesis are presented.

1.1 An introduction to petroleum exploration and production

A hydrocarbon reservoir consists of a porous rock (mostly clastic) in the subsurface that contains hydrocarbons in the pore space with an overlying cap rock (often shale or salt) that prevents the hydrocarbons from migrating upwards. Important reservoir characteristics are porosity, permeability and a petroleum trap. Porosity, i.e. the fraction of the rock that can be occupied by fluids, and permeability, i.e. a measure of the rock's ability to transmit fluid through the pores, describe the reservoir potential for storage and production of hydrocarbons. Accumulations of hydrocarbons are almost

exclusively in sedimentary rocks, where geological structures or differences in the rock lithology stop the upward migration of hydrocarbons. Any barrier to the upward or later movement of oil and gas allowing them to accumulate is known as a petroleum trap.

The exploration of oil reservoirs is usually carried out through the interpretation of geological information and the use of geophysical techniques, such as seismics. Elastic waves are sent into the subsurface and arrays of sensors are used to measure the energy reflected back to the surface. As differences or contrasts in physical properties, such as compressibility or density, create reflections, an image of the subsurface can be reconstituted by processing the seismic data properly. The interpretation of these images allows the localization of potential oil reservoirs. Currently, another popular geophysical technique for exploration consists of electromagnetic sounding, where a dipole source transmits a low frequency, typically a few tenths of a Hertz to few tens of Hertz, electromagnetic (EM) field into the earth. This field, measured by an array of EM receivers at the surface, is very sensitive to the subsurface resistivity distribution. Since hydrocarbon bearing formations are highly resistive with respect to the surrounding formations, the EM surveys can indicate the presence of oil in the subsurface.

EM sounding is complementary to seismics, as the first is highly sensitive to the pore fluids, whereas the latter is mainly sensitive to layering and the architecture of the rocks. There is an active research effort in joint seismic and EM inversion (e.g. Hoversten *et al.*, 2003; Zhanxiang *et al.*, 2007), but the differences in data densities, resolving power and the lack of unique rock physics relationships between seismic velocity and resistivity make this a challenging problem. Overlying resistivity images on seismic reflection profiles seems to be a common effective approach to integrate the two methods (Constable, 2010). The added value of combining the two methods has been evaluated in Eidsvik *et al.* (2008).

Once a potential oilfield is discovered, exploration wells are drilled and log data are gathered. Well logs, i.e. recordings of physical rock properties by lowering measurement tools in the wellbore, and core samples are used to further characterize the geological environment and to assess the hydrocarbon production potential. In case the oilfield is considered to be economically profitable, a development strategy can be further determined and eventually the field can be taken into production.

Initially, the reservoir pressure is sufficient to force the oil through the production wells to the surface, a stage known as primary recovery. However, in time the decrease of the reservoir pressure resulting from the oil extraction makes this driving mechanism weaker eventually leading to a non-

economic production. To maintain the production economical, it is necessary to re-pressurize the reservoir through the injection of water or gas generally referred to as the secondary recovery phase. When after the second phase the production starts to decrease again, for example if too much of the injection water is reproduced, sophisticated techniques, like steam injection, chemical flooding or miscible displacement methods, referred to as the tertiary recovery are used.

1.2 Closed-loop reservoir management

Nowadays, the continuous increase of oil demand in combination with the decline in production of the relatively easy accessible fields has forced petroleum engineers to maximize the oil recovery and extract more oil from existing fields. A recent trend is to manage the production of a reservoir as a model-based control process, which is referred as “closed loop reservoir management”, or also known as “real-time reservoir management”, “e-fields” or “smart fields” (Jansen *et al.*, 2008, 2009). Figure 1.1 depicts the key elements of the closed loop process.

The concept is relatively simple. Improvements in sensors and hardware over the last decades have made it possible to perform a larger variety of measurements (semi-)continuously in producing fields. Examples are developments in 4D seismics and fibre-optic temperature measurements downhole. In parallel, production technology, especially well technology, has made it possible to better control reservoir management. Examples are discussed in a separate section. The aim is of course to combine both and that all information extracted from the sensor data leads to better decision-making for the control strategy of the field. Examples are controlling the optimal production rate per well or well segment, or controlling water-injection rates in case of Enhanced Oil Recovery (EOR). However, in practice it has proven difficult to incorporate all these data into the decision making process and there is a clear need for (semi-)automatic support and uncertainty handling.

The aim of the closed-loop concept is to incorporate all these data continuously in models while respecting the different uncertainties associated. These models can then be used to optimize the production strategy. Therefore two loops can be discerned in figure 1.1. The first loop, referred to as data assimilation or history matching, consists of a continuous update of the models incorporating all data available. The second loop consists of optimizing the control strategy using the data assimilated models.

Note, that the closed loop concept can be applied at different scales both in time and space. Two major domains are distinguished: daily production,

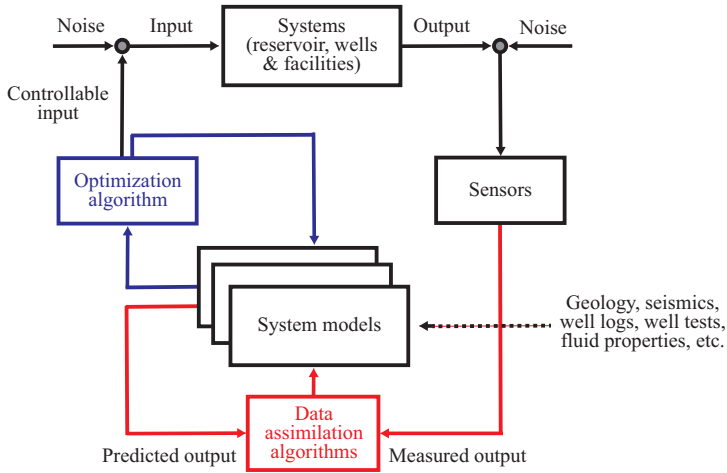


Figure 1.1: Reservoir management depicted as a closed-loop model-based controlled process (from Jansen *et al.* (2009)).

i.e. on a scale of days to weeks, and reservoir management, i.e. on a scale of months to years. The daily production domain concerns mainly the well-bore and near-well region and involves downhole measurements of production variables such as pressure, and oil, gas and water rates (considered output in figure 1.1). The control typically consists of the individual well setting and aims at short term optimization objectives, e.g production targets or utilization rates (considered input in figure 1.1). This is usually decided without the use of extensive reservoir models, whereas models describing the multi-phase flow in the near well region, through the wells and through the surface facilities are used.

Reservoir management concerns the entire reservoir and aims at maximizing the reservoir drainage and the asset revenues. Reservoir imaging sensors, such as time-lapse seismic, are used to get a global picture of the reservoir dynamic processes (output). This information in combination with extensive reservoir modelings is used for long-term optimization and the decision to be taken may involve the placement of new wells or which strategy to be used globally per well (input).

1.3 Overview of smart wells technology

The implementation of closed-loop management is essentially based on smart well technology. Smart wells, also referred to as intelligent wells, are completion systems which allow for zonal production control and monitoring in real time through, respectively, flow control devices and downhole sensors; reviews of smart well applications and achievements are in Glandt (2005), Gao *et al.* (2007), Raw & Tenold (2007) and Nadri Pari & Kabir (2009). Figure 1.2 shows a schematic representation of a smart horizontal well. The perforations connect the reservoir to the annulus, the area between the casing and the tubing, which is divided in individual compartments by rubber elements called packers. Each compartment is equipped with a flow control device that can regulate (at different extent) the fluid flow from the outer well into the inner well and with different downhole sensors. In the next sections a description of the current state-of-the-art of both the flow control devices and the major sensing technology currently used (or still at a research and development stage) is provided.

1.3.1 Inflow control technology

Inflow control technology was introduced with the advent of horizontal wells. These wells have increased the well-reservoir contact improving well productivity, drainage area and sweep efficiency; however, at the same time, they have brought difficulties when reservoir drainage control is required, e.g. in case of premature breakthrough of undesired fluids such as water or gas. Such phenomena usually occur due to:

- reservoir permeability heterogeneity,
- variations in distance between the wellbore and the fluid contacts,
- variations in reservoir pressure in different regions,
- pressure drop along the completion due to friction (the heel-toe effect).

Many of these issues can be mitigated by installation of downhole flow control devices, which can be “passive” Fixed Control Devices (FCDs) or “active” Inflow Control Valves (ICVs). Studies devoted to compare the functionality and applicability of the two technologies have been carried out, e.g., by Al-Khelaiwi *et al.* (2008) and Lauritzen *et al.* (2011).

Fixed Control Devices (FCDs), also known as Inflow Control Devices (ICDs), restrict the fluid flow from the reservoir to the tubing with the intent

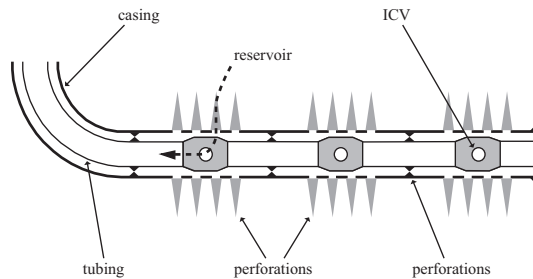


Figure 1.2: Schematic representation of a smart horizontal well. The perforations connect the reservoir to the outer well (annulus). The annulus is divided in individual compartments through rubber elements (packers). Inflow control valves (ICVs) control the flow from the compartments to the inner well (tubing). (from Jansen *et al.* (2008).

of equalizing the wellbore pressure drop to achieve an evenly distributed profile. The location of the devices and the relationship between the rate and the pressure drop cannot be adjusted during production and have to be decided prior to the installation. Therefore, an effective control requires a thorough knowledge of the reservoir' geology in the near well region and its drive mechanisms, so that the inflow can be predicted with confidence using reservoir and well models. FCDs allow for a passive control strategy, characteristic of an open-loop system.

Active or closed-loop control is favored by ICVs, which are operated remotely through hydraulic or electric actuation systems. The adjustable valves may range from on/off to an infinite number of settings. ICVs in combination with the monitoring systems (see next section) allow for two main types of active control strategies: reactive and proactive. Reactive strategies change the ICV settings in response to the breakthrough of displacing phases, such as water or gas, measured within the well. Wellbore sensors, e.g. downhole flow monitoring systems, can be used for this purpose. Proactive control, conversely, is a defensive strategy. Actuation of ICVs takes place prior to the arrival of the displacing phases. These strategies require the deployment of sensors that monitor the fluid flow away from the wellbore. The latter is the focus of the proposed borehole radar tool.

1.3.2 Monitoring sensors

The sensors are a key element in smart well technology because they provide measurements of fluid dynamics inside the wellbore, down-hole sensors, or

more extensively in the reservoir, reservoir-imaging sensors.

Down-hole sensor

Down-hole sensing involves both logging tools lowered during production or shut-in periods and permanent sensors generally deployed inside the completions. Production logging is mainly used to determine the dynamic patterns of flow rates of water, oil and gas inside the well. This is achieved through fluid-flow measurements; for example, turbine flowmeters are used to determine the fluid velocity and gradiometers for density. Additional measurement systems are manometers for pressure and thermometers for temperature.

Permanent sensors include different adapted technologies and are nowadays widely used for closed-loop management because they allow continuous measurements. In this section a brief description of the state of permanent sensor technology is given.

The most commonly used permanent sensors measure temperature and pressure. These measurements were available already before the advent of the smart well technology and were acquired through electrical system, also known as permanent downhole gauges. They are based on resonant quartz crystals, of which the resonant frequency is a function of pressure and temperature.

Recent advances have introduced the optical fiber sensors based on Bragg grating technology. Bragg gratings are intrinsic sensitive elements distributed in the core of an optical fiber and they reflect light at a very narrow frequency. This sensitive element is then built into a sensing head that applies a small stress to the fiber when exposed to the event to be measured (e.g. temperature and pressure). This causes a very small change in the length of the fiber, which results in a detectable change in the reflected frequency. Therefore, the grating can be used as a form of optical strain gauge. Through appropriate calibration and packaging, Bragg grating sensors have been developed to measure a wide variety of wellbore parameters, including temperature, pressure, flow rate, phase fraction, and acoustics (Kragas *et al.*, 2004).

Distributed optical measurements are also an advance available thanks to fiber optic but based on a different principle. An optical cable is deployed along the entire well and the analysis of the backscattered light sent through the cable allows to capture distributed temperature measurements. In fact, small amounts of light are reflected back due to temperature variations in the fiber. The magnitude of the reflected light is a function of temperature and the time taken for the reflected light to reach the surface instrumentation is a measure of the spatial position along the cable (Kluth *et al.*, 2000).

Downhole flow meters based on optical technology are in a development stage (Drakeley *et al.*, 2006); however, downhole multi-phase flow meters that use gamma-ray densitometers and modified arrangements of a “venturi” flow meters are available (Webster *et al.*, 2006).

Reservoir-imaging sensors

Reservoir-imaging sensors aim at mapping the fluid movements away from the well. However, this type of sensing is at a different stage of maturity with respect to down-hole sensors and there is an active research effort in developing and evaluating new monitoring technology.

Though not directly a downhole application, it is important to mention time-lapse seismic, or 4D seismic, since it is the most established technology for fluid monitoring and reservoir management (Jack & Singer, 1997). Although 4D seismic data provide subsurface images at a limited resolution with respect to in-well sensors, it is currently the main source of surveillance information away from the wells. Saturation changes are tracked by observations of the differences in seismic images acquired over time (usually at yearly intervals). An essential requirement for a successful mapping of production induced changes is the quality of the repeatability of the time-lapse seismic surveys. A solution to positioning problems of the seismic sensors are permanent installed onshore and offshore geophones Watts *et al.* (2006). Permanent down-hole geophones using optical seismic sensors (accelerometers) in a Vertical Seismic Profile (VSP) setting have enhanced the imaging potential; however, hardware developments are in an early stage and interpretation techniques are under development Drakeley *et al.* (2006). Other complications concern the spatial resolution limitations, low signal-to-noise ratios, and near surface irregularities.

Electromagnetic measurements are mainly used for exploration purposes; nevertheless, in the beginning of the last decade van Kleef *et al.* (2001) reported a successful use of electrical measurements for monitoring purposes. An array of electrodes permanently cemented at the reservoir level allowed the determination of the saturation field at some distance away from the well. This successful field trial opened up a new monitoring technology referred as Dynamic Reservoir Drainage Imaging (DRDI). The principle of DRDI consists of using each electrode as a low frequency current source (active mode) while monitoring voltage at the other electrodes. The DRDI depth of investigation is principally related to the thickness of the reservoir and to the resistivity contrast between the medium in which the electrode array is installed and the invading medium to be measured. Examples of DRDI

monitoring and control applications have been carried out by Kharghoria *et al.* (2002), Charara *et al.* (2002) and Bryant *et al.* (2004). Recent studies have combined the resistivity measurements with other down-hole sensors to enhance quantitative characterization of fluid movements (Zhan *et al.*, 2010; Kuchuk *et al.*, 2010).

The DRDI permanent electrodes can also be used in passive mode to measure electrokinetic streaming potential in the reservoir. Such potential is generated when ionic fluid flows through rock, a phenomenon included under the term of self-potential, that has been the subject of theoretical (e.g. Revil *et al.*, 1999; Bernabe, 1998) and laboratory studies (e.g. Beamish & Peart, 1998; Fagerlund & Heinson, 2003). Chen *et al.* (2006) were the first to measure streaming potential in oilfield environments. Follow-up studies suggested that measurements of streaming potential can be used to detect water encroachment towards an intelligent well equipped with permanent electrodes (Jackson *et al.*, 2005; Saunders *et al.*, 2006). Saunders *et al.* (2008) indicated that the depth of investigation can be from tens of meters up to hundred meters and that the magnitude of the measured potential depends on the production rate, the coupling parameters between fluids and electrical potential and the salinity of the displacing water front. Further analysis led to a quantification of the relation between the water salinity and the streaming potential coupling coefficient both experimentally (Jaafar *et al.*, 2009; Vinogradov & Jackson, 2011) and numerically (Gulamali *et al.*, 2011): high water salinity reduces the magnitude of the streaming potential signal.

An other sensing technique is 4D gravity, which as 4D seismic is based on differences of the measured signal over time. The gravity sensors have experienced a significant improvement in the last decades, which extended their use (Biegert *et al.*, 2008). 4D gravity proved to be a valuable tool to infer subsurface density changes associated with production from oil and gas reservoirs (M. *et al.*, 2008) with the most common application being monitoring of water influx in gas reservoirs (Stenvold *et al.*, 2008). It is considered a complementary technique, when properly constrained by other subsurface information, that can add significant value for reservoir monitoring. The resolution of 4D gravity strongly depends on the density contrast of the changes to monitor; therefore, it is more suitable for monitoring a water/gas contact rather than water/oil contact. Measurements from the surface result in low resolution images when compared to seismic data. A borehole gravity tool exists as a wireline logging tool. In principle this tool could be used in a time-lapse mode to detect changes related to fluid front movements. However, repeatability of the logging remains an issue for now and no permanent sensor is available yet. The future of this technology might lie in continuous

and downhole observations, which are at an early stage.

1.4 Ground Penetrating Radar

In this thesis we investigate the potential for borehole radar as a monitoring tool to detect fluid fronts. This section provides an overview of general radar technology and its current applications in other domains. Ground Penetrating Radar (GPR) is a general term applied to techniques which employ electromagnetic (EM) waves, typically from 30 MHz to 3 GHz (Annan, 2005b). The fundamental principles of GPR can be described in terms of the transmission, scattering (reflection, refraction, diffraction and resonance), and detection of EM waves propagating through the medium under investigation. A radar system uses a transmitting antenna, which emits an EM wave field into the subsurface and a receiving antenna, that records this field and its reflections. Maxwell's equations describe mathematically the propagation, reflection and transmission of the EM field, which is related to the material properties through the constitutive equations. The material properties include the magnetic permeability, i.e. the ability of the medium to respond to a magnetic field, the dielectric permittivity, i.e. the ability of a medium to become polarized in response to an electric field, and the electric conductivity, i.e. the availability and mobility of the electric charges. These properties control the EM wave propagation in a medium: permittivity and permeability determine the velocity of the wave, while the conductivity determines the energy that is converted into heat, i.e the attenuation.

When a GPR wave encounters changes in the EM properties of a medium, resulting in impedance contrasts, part of the wave is reflected back, while the remainder is transmitted forward. Such contrasts can be detected, imaged and characterized. The following conditions have to be satisfied to detect the desired target: (1) the energy of the EM wave must be sufficient to propagate from the transmitter down to the target and back to the receiver, (2) the impedance contrast at the interface between the target and the surrounding must be sufficient to create a detectable reflection.

GPR has proved to be very sensitive to changes of water saturation in geological materials, due to the high permittivity contrast between water and the other soil and rock components. This explains the numerous applications in environmental and hydrogeological fields (Knight, 2001; Annan, 2005a), such as aquifer characterization (Asprion & Aigner, 1997; Engdahl *et al.*, 2010), mapping water movements (Tsofiias *et al.*, 2001; Talley *et al.*, 2005), measuring water content (Huisman *et al.*, 2003), assessing time varying concentration and distribution of oil derived liquids (Splajt *et al.*, 2003;

al Hagrey, 2004), detecting thawing zones in permafrost (Bradford *et al.*, 2005). Further applications are in stratigraphy and sedimentology (Davies & Annan, 1989), glacier sounding (Plewes & Hubbard, 2001), fracture mapping (Grasmueck, 1996), archeology (Gaffney, 2008), planetary exploration on Mars and the moon (Pettinelli *et al.*, 2007), land-mine and unexploded ordnance detection (dan, n.d.), and non-destructive testing for civil engineering problems (Halabe, 1996; He *et al.*, 2009). The cited references are reviews or case studies of GPR applications, however they do not reflect the complete overview of the literature available on the subject.

The design of GPR is largely application-oriented, i.e. when the desired target is deep in the subsurface, specific antennas that fit the borehole size have to be deployed. Borehole antenna characteristics are quite different with respect to surface GPR because inside the borehole the interaction with the surrounding strongly affects the antenna radiation patterns.

Borehole radar is an active area of research with applications focusing on operating in a single borehole or between boreholes (cross-hole application). As the surface GPR, borehole radar has diverse applications depending on the depth to be investigated. For deep investigations EM logging tools have already proved the GPR potential in imaging the neighborhood of a well (e.g. Liu *et al.*, 2004; Mason *et al.*, 2008). A pioneering radar system based on optical electric field sensors, that can be fixed in the subsurface, have been proposed recently by Ebihara *et al.* (2006); Sato & Takayama (2007).

As the GPR design, the processing of GPR data is application dependent. Minimal processing is required when the detection of a target is the only desired information, while modeling and/or inversion is necessary when some quantification is desired, such as determination of target geometry or retrieval of physical properties of the target.

1.5 Problem definition

The sensing technologies currently used during production of oil reservoirs do not satisfy all the monitoring requirements, in particular the early detection of fluid fronts away from the wells. The most commonly used downhole sensors measure pressure and temperature and sample only the region inside the well, while the reservoir imaging techniques can see far away from the well but at low resolution. Especially 4D seismic, which is the best-established technique cannot image flow processes within ten meters from the well; moreover, it is scarcely sensitive to monitor oil-water contact movements and it cannot be acquired continuously. Downhole electrical measurements are still under development and again cannot resolve the near well

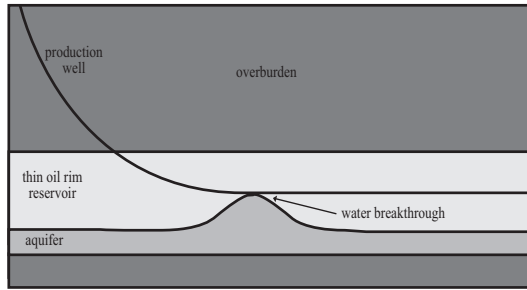


Figure 1.3: Schematic representation of water breakthrough phenomena in a thin oil rim reservoir.

region accurately. Generally the near-well region in the order of ten meter is poorly imaged and although there is active research in developing the current sensing technology, no sensor is envisaged to characterize the first ten meters away from the well. However, in specific reservoir environments the monitoring of this region is strongly required. For example, thin oil rim reservoirs usually have a thickness in the order of few tens of meters and are characterized by early water breakthrough in individual segments of the well (figure 1.3). This has a strong impact because it reduces the oil production and it may cause an early shut-down of the well. Steam Assisted Gravity Drainage (SAGD) is an enhanced oil recovery technique used in heavy oil reservoirs, where oil is extremely viscous and steam injection is used to facilitate the oil flow. A pair of horizontal wells is drilled into the reservoir a few meters from each other to allow the steam injection and the oil production (figure 1.4); however, the steam chamber growth and the oil flow are largely unknown. In both these examples a better understanding of the oil displacement process in the first ten meters from the production well could help preventing early breakthrough of unwanted fluids and allow for an implementation of more effective control strategies.

1.6 Research objective and outline

Following the discussion on the monitoring requirements in the near-well region and the GPR ability in mapping fluid flow in geological media, the research objective of this thesis is to investigate the feasibility of radar technology as a potential reservoir-imaging sensor for oilfield applications. Borehole radar is envisaged as a promising technology for sensing the system described

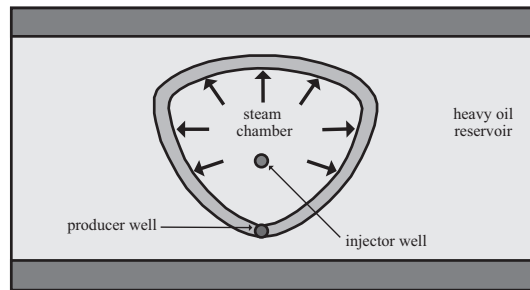


Figure 1.4: Schematic representation of a SAGD process (from Butler (1991)).

in figure 1.1 and as an additional information to include in the data assimilation and optimization loops. The study is mainly based on numerical modeling and laboratory experiments to investigate the feasibility of using this technology in the borehole environment.

The thesis is structured as follows:

- Chapter 2 first reviews the EM wave theory relevant to the application of a radar system in an oilfield environment. One-dimensional modeling is used to investigate the expected signal magnitude and depth of investigation. Potential applications have been restricted to monitor steam chamber growth in steam assisted gravity drainage processes and water front monitoring in thin oil rim scenarios. A numerical analysis of the sensitivity of the signal is carried out through 2D finite difference modeling, taking in consideration wellbore and reservoir constraints. This chapter is based on Miorali *et al.* (2011).
- Chapter 3 is an in-depth analysis through numerical modeling, where EM simulations are coupled to flow simulations. The drainage process of a bottom water-drive reservoir is simulated and the time-lapse radar response has been analyzed. This chapter is based on Miorali *et al.* (2011).
- Chapter 4 shows the experimental results of water flooding experiments performed under laboratory conditions. Two types of dynamic experiments are presented: the first consists of water flooding in residual water saturation conditions and the second in oil saturated conditions. Part of this chapter is based on Miorali *et al.* (2011).
- Chapter 5 discusses the uncertainties of measured and modeled radar signal on quantitative characterization of EM and geometric parameters through full-waveform inversion.

- Chapter 6 summarizes the conclusions and gives recommendations for future developments.

Chapter 2

EM wave in oilfield environment¹

2.1 Introduction

The combination of measurement and control techniques is being increasingly used in the oil industry, because it has the potential to significantly improve the oil and gas production (Robison, 1997; Nyhavn *et al.*, 2000; Brouwer & Jansen, 2004; Glandt, 2005). This is due to the recent development of smart well technology, which allows zonal production control and monitoring in real time through, respectively, inflow control valves (ICVs) and down-hole sensors (Jansen *et al.*, 2008). Each individual compartment of the well is equipped with ICVs capable of imposing a pressure profile along the well that can influence the flow behaviour in the reservoir. Adjusting the setting of the ICVs in response to monitoring data obtained from down-hole sensors enables the implementation of proactive control strategies, which may yield near-optimal recovery (Addiego-Guevara & Jackson, 2008). The advantage of proactive control is that potential problems, such as the approach of unwanted fluids, can be mitigated before they impact the production (Ebadi & Davies, 2006). The efficiency of these strategies is based on the capacity of measuring or predicting changes in the reservoir far away from the well (Jackson *et al.*, 2005; Brouwer *et al.*, 2004). However, predictions always contain uncertainties and the current down-hole monitoring techniques sample only the region immediately adjacent to the wellbore. The most used down-hole sensors measure pressure and temperature and are more suitable for reactive control strategies, where the ICVs are set in response of adverse change in flow measured within the well. Several applications are described in Davies

¹This chapter has been published as journal paper in *Geophysical Prospecting* **127**(4), 120-131 (Miorali *et al.*, 2011). Note that minor changes have been introduced to make the text consistent with the other chapters of the thesis.

et al. (2008), Aggrey *et al.* (2007) and Almutairi & Davies (2008).

There is an intense research effort to discover new monitoring techniques that could capture the fluid dynamics in the far-field of the well. For example, Saunders *et al.* (2006, 2008) have suggested that electrokinetic potential measurements should be sensitive to the movement of an approaching water front at several tens to hundreds of meters from the well. This potential field data would provide optimal control strategies in waterflooding processes where the distance between injection and production wells is in the order of hundreds of meters (Jackson *et al.*, 2005). However, according to the type of reservoir and/or the type of depletion technique used, a different reservoir volume has to be monitored. Consequently, down-hole sensing techniques with different resolutions and depths of investigation are required.

Steam Assisted Gravity Drainage (SAGD) is an Enhanced Oil Recovery (EOR) technique used in heavy oil reservoirs. A pair of horizontal wells is drilled into the reservoir, typically at a few meters distance from each other. The upper well is used to inject steam, which reduces the oil viscosity and makes the oil drain toward the lower production well. A down-hole sensor capable of investigating several meters (near-field) away from the production well would be enough to monitor the steam chamber growth and enable improved control strategies compared to standard production methods. Typically, similar depths of investigation would be required in case of thin oil rim reservoirs. These reservoirs are generally exploited by horizontal wells passing through the thin reservoir making water breakthrough at different intervals a problem. Early detection and consequently prevention of water breakthrough along the borehole trajectory is a major issue.

Chen & Oristaglio (2002) have considered borehole radar as an imaging technique for oilfield applications and they have concluded that a penetration depth of several meters can be realized for relatively low conductive reservoirs. We suggest borehole radar measurements as a potential technique capable of monitoring fluid saturation changes in the near-field of production wells. Electromagnetic (EM) measurements in the radar frequency range, referred to as Ground Penetrating Radar (GPR) technology, have already been applied successfully for fluid flow monitoring applications in the shallow subsurface (Annan, 2005a,b; Lambot *et al.*, 2008b; Slater & Comas, 2009). As the dielectric permittivity of water overwhelms the permittivity of other soil or rock components, changes in water saturation create partial wave reflections that can be picked up by a radar system. An array of down-hole radar sensors located in production wells would satisfy the requirements necessary in SAGD processes and in thin oil rim reservoirs. In figure 2.1 a potential implementation of a radar system in a SAGD process is depicted.

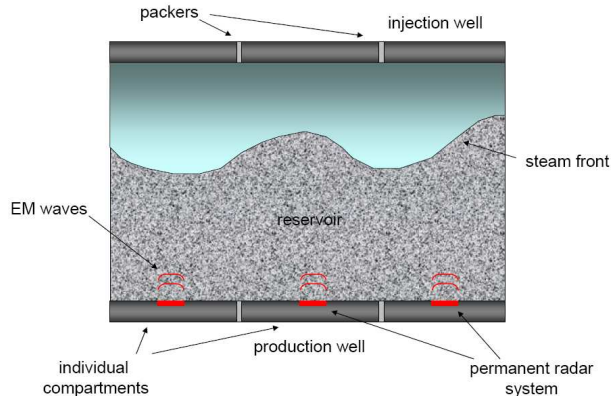


Figure 2.1: Schematic representation of a potential implementation of a radar system as a down-hole permanent sensor in a SAGD process. The steam injection is necessary to reduce the high viscosity of the heavy oil, which is then driven toward the production well by gravity.

The aim of this chapter is to study the feasibility of radar technology as a permanent monitoring method. We first review the EM wave theory relevant to the application of a radar system in an oil reservoir. Then we extend the approach defined by Noon *et al.* (1998) to evaluate the maximum penetration depth and the magnitude of the expected signal received by a radar system. A more sophisticated analysis is carried out through 2D simulations. We use GprMax (Giannopoulos, 2005, 1997), a FDTD EM solver, to simulate different reservoir scenarios.

2.2 Wave propagation

The ability of a borehole radar tool to image the near-well region mainly depends on the applied frequency and on the EM properties of the medium: electrical conductivity σ , electric permittivity $\epsilon = \epsilon_r \epsilon_0$ and magnetic permeability $\mu = \mu_r \mu_0$, where ϵ_r and μ_r are the relative electric permittivity and the relative magnetic permeability respectively, and ϵ_0 and μ_0 are the electric permittivity and the magnetic permeability in free space, $\epsilon_0 = 1/(\mu_0 c_0^2)$ F/m ($c_0 \approx 3 \times 10^8$ m/s is the speed of light in free space) and $\mu_0 = 4\pi 10^{-7}$ H/m. For the geological media we are interested in, $\mu_r = 1$, so the significant EM properties are ϵ_r and σ . In a homogeneous medium the complex wavenumber $\gamma = \gamma_r + i\gamma_i$ has a real component γ_r , which represents the attenuation part, and an imaginary component γ_i , which represents the propagating part;

these are respectively given by:

$$\gamma_r = \frac{\omega}{c} \left[\frac{1}{2} \sqrt{1 + \delta^2} - \frac{1}{2} \right]^{1/2}, \quad (2.1)$$

$$\gamma_i = \frac{\omega}{c} \left[\frac{1}{2} \sqrt{1 + \delta^2} + \frac{1}{2} \right]^{1/2}, \quad (2.2)$$

where ω is the angular frequency, $c = (\epsilon\mu)^{-1/2}$ is the phase velocity and $\delta = \sigma/\omega\epsilon$ is the loss tangent. Values of the attenuation (ATT), in decibels, and of the phase distortion (PH_{err}) are given by the following equations:

$$ATT = 20 \log_{10} (e^{\gamma_r}) \approx 8.68\gamma_r, \quad (2.3)$$

$$PH_{err} = \frac{\gamma_i}{\omega\sqrt{\mu\epsilon}}. \quad (2.4)$$

PH_{err} is the ratio of the actual phase constant to its value in a non-conductive medium. We have considered realistic values of EM properties and we have studied their effect on ATT and PH_{err} . The natural regime for radar measurement occurs when $\delta \ll 1$, so that attenuation becomes independent of frequency, phase distortion can be neglected, and wave propagation prevails over diffusion phenomena. Analysis shows that this requirement is met for frequencies above 100 MHz and the main constraint is given by the conductivity (fig.2.2). Permittivity does not have a relevant impact. In case of 100 MHz frequency and $\epsilon_r = 8$, wave propagation is the dominant factor for all the $\sigma < 0.02$ S/m.

When $\delta \gg 1$, the diffusive character prevails and phase distortion starts to have a strong impact on the pulse shape. This effect is clearer in the time domain. We use a FDTD electromagnetic wave simulator, GprMax (Gianopoulos, 2005), to show how the propagation of a wavelet is affected by different values of σ . The time waveform and the amplitude spectra of the EM source wavelet are depicted in figure 2.3. Figure 2.4 shows the normalized instantaneous amplitude expressed in dB of a direct wave traveling in a medium with a fixed value for ϵ and different values for σ . We can evaluate the attenuation a wave would undergo in different conductive media. After traveling 4 m in a medium with $\sigma = 0.001$ S/m the attenuation is about 15 dB, when $\sigma = 0.01$ S/m, the attenuation increases to 25 dB, around 55 dB for $\sigma = 0.05$ S/m and approximately 70 dB for $\sigma = 0.1$ S/m. Due to the technical limit of the system performance a radar tool could achieve (around 100 dB), a threshold of 100 dB has to be applied to the images of figure 2.4. For the case of $\sigma = 0.01$ S/m, which is the one we investigate in our model, an

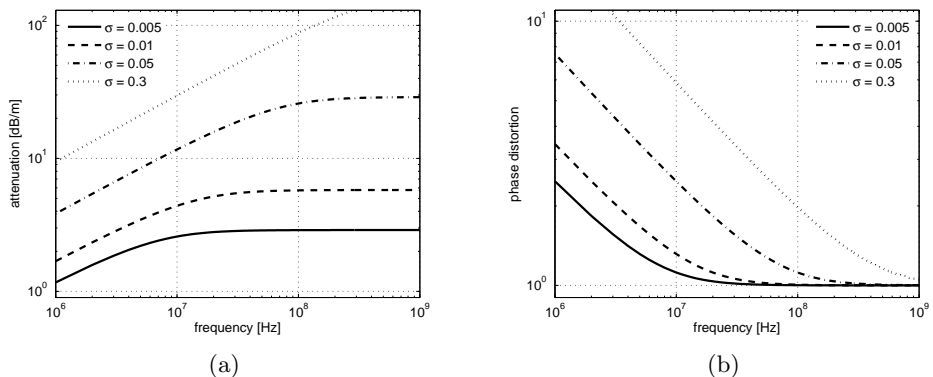


Figure 2.2: Wave attenuation ATT and phase distortion PH_{err} versus frequency for different values of conductivity σ and a fixed permittivity ($\epsilon_r = 8$).

attenuation of 50 dB occurs after a distance of about 8 m, since after 4 m we see a decrease of 25 dB. Moreover, we can observe that σ has a strong effect on the pulse shape of the EM wave. In figure 2.4a, we see that the envelope of the signal is enclosed in a time window of about 15 ns for all the distances shown; in figure 2.4d, instead, we see that the envelope is spread in a time window of 60 ns already at 1 m from the source, and it gets larger and larger with increasing propagation distance. Changes of the pulse shape strongly affect the resolution, which means the minimum distance two reflectors need to be separated for them to be detected as two reflectors. Resolution is usually expressed by $r = Wc/4$, where W is the pulse width at half of the peak amplitude and c is the phase velocity of the material (Annan, 2005b). For the case $\sigma = 0.01$ S/m, $\epsilon_r = 8$ and an applied center frequency of 100 MHz, r is almost independent of distance and is approximately 0.3 m. For the same condition and $\sigma = 0.3$ S/m, r is 0.3 when the wave is 1 m from the source and already about 2 m at a distance of 4 m.

2.2.1 EM properties of rocks

We have used a volumetric model to get effective values of relative permittivity ϵ_{eff} , therefore the dielectric properties of a rock are based on the relative volumes of the different components and their individual dielectric characteristics. The Complex Refractive Index Model (CRIM), proposed by Birchak *et al.* (1974), is the most frequently used mixing model in the radar range of frequencies, since it appears to fit laboratory measurements best (Roth *et al.*, 1990; Seleznev *et al.*, 2004; Knoll *et al.*, 1994); in the case of three

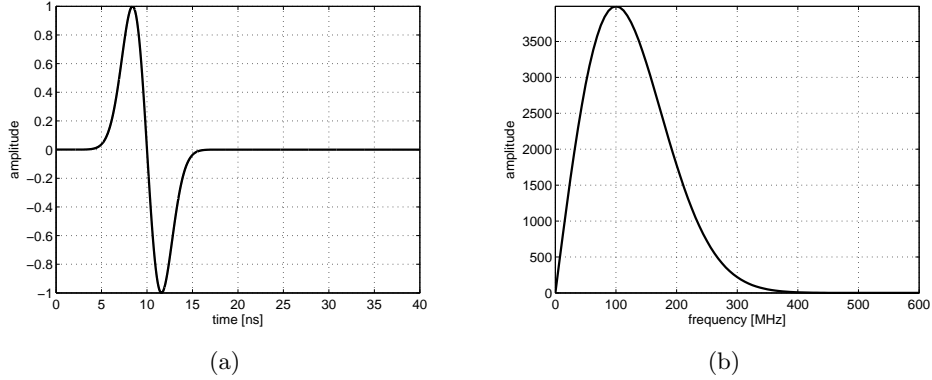


Figure 2.3: Time waveform (fig. 2.3a) and amplitude spectra (fig. 2.3b) of the excitation function. The center frequency is 100 MHz.

components it is given by the following formula:

$$\epsilon_{eff}^{1/2} = (1 - \phi)\epsilon_s^{1/2} + \theta\epsilon_w^{1/2} + (\phi - \theta)\epsilon_o^{1/2}, \quad (2.5)$$

where ϵ_s , ϵ_w and ϵ_o are respectively the relative permittivity of the solid, the water and the oil, ϕ is the porosity, $\theta = \phi S_w$ is the volumetric water content and S_w is the water saturation. To get the effective conductivity σ_{eff} we have used Archie's law (Archie, 1942). A large series of ϵ_{eff} and σ_{eff} was obtained by making the rock and fluid dependent variables of equation 2.5 and Archie's law vary in a broad range of realistic values ($0.05 < \phi < 0.4$, $0 < S_w < 1$, $1.3 < m < 2.2$ and $1.3 < n < 2.2$, where m and n are respectively the cementation and saturation exponents of Archie's law). These values were used for general considerations of the EM wave propagation and reflectivity behavior in a wide range of reservoir conditions. Both ϵ_{eff} and σ_{eff} are mainly controlled by the amount of pore water. In fact, the relative permittivity of water is much higher than the one of the other reservoir components ($\epsilon_w = 80$, $\epsilon_o = 2 - 3$ and $\epsilon_s = 4 - 10$) and just the electrical conductivity of water can reach values that would have strong impact on the EM wave propagation ($\sigma > 0.1$ S/m), σ_o is lower than 10^{-6} and σ_s is scattered over several orders of magnitude but for reservoir material it does not exceed 10^{-4} (Schön, 1998). The EM properties of water, instead, can be strongly affected by temperature and salinity. As temperature increases, thermal agitation reduces the interaction between the dipoles of the water and the electric field, while it facilitates the movement of the ions, so the overall effect is a reduction of ϵ_w and an increase of σ_w . The addition of salt

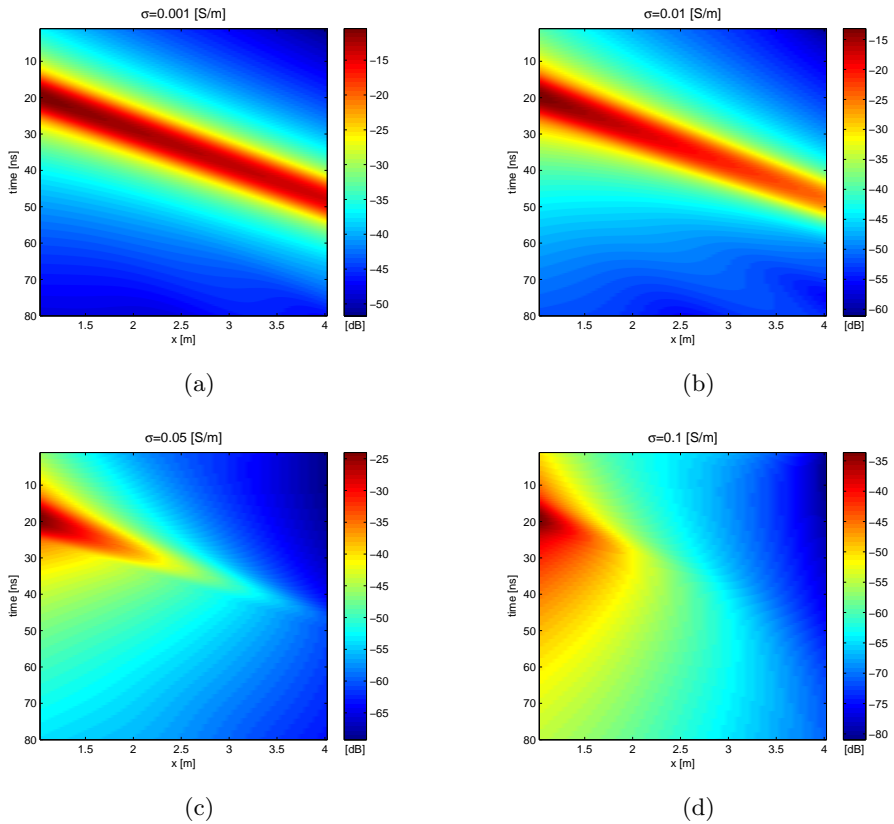


Figure 2.4: EM direct wave in media with a fixed permittivity ($\epsilon_r = 8$) and with different value of conductivity: $\sigma = 0.001$ S/m, $\sigma = 0.01$ S/m, $\sigma = 0.05$ S/m, $\sigma = 0.1$ S/m. The color scale represents the normalized instantaneous amplitude of electric field expressed in dB.

to water decreases ϵ_w , since the amount of the molecules able to polarize is reduced. The electrical conductivity, instead, is directly proportional to the total number of dissolved salt ions, since the conduction of current in an electrolyte depends on the salinity. Consequently, both temperature and saline concentration have a relevant influence on the effective EM properties of a rock (Ellis & Singer, 2007). For the SAGD model discussed in the following session we used the rock and EM properties representative of the Athabasca oil sand. The actual formation temperature in the Athabasca deposits varies from about 10° to 15° C and the formation σ_{eff} and ϵ_{eff} can vary respectively between 0.003-0.02 S/m and 6-10 (Chute *et al.*, 1979). The average porosity is 0.3 and the water saturation is usually less than 0.4. Average values of the cementation and saturation exponents are respectively 1.4 and 1.8 (Carlson, 2003).

2.3 Reflectivity of an interface

An important parameter for the feasibility of a borehole radar system is the reflectivity of the interface to be detected, the steam or the water front. If the reflectivity of the fluid front is weak, a radar system may not be able to detect it. The reflectivity expresses the amount of reflected energy and it depends on the reflection coefficient, which can be split into a transverse electric (TE) mode and into a transverse magnetic mode (TM). For a single planar interface, the plane wave reflection coefficients are given by:

$$r_{TE} = \frac{c_2 \sqrt{\cos^2 \theta - i\delta_1} - c_1 \sqrt{1 - c^2 \sin^2 \theta - i\delta_2}}{c_2 \sqrt{\cos^2 \theta - i\delta_1} + c_1 \sqrt{1 - c^2 \sin^2 \theta - i\delta_2}}, \quad (2.6)$$

$$r_{TM} = \frac{\eta_2 c_2 \sqrt{\cos^2 \theta - i\delta_1} - \eta_1 c_1 \sqrt{1 - c^2 \sin^2 \theta - i\delta_2}}{\eta_2 c_2 \sqrt{\cos^2 \theta - i\delta_1} + \eta_1 c_1 \sqrt{1 - c^2 \sin^2 \theta - i\delta_2}}, \quad (2.7)$$

where the subscript $i = 1, 2$ denotes two different media, θ denotes the angle of incidence, $\delta_i = \sigma_i / \omega \epsilon_i$, c_i is the velocity of the medium and $\eta_i = \sigma_i + i\omega \epsilon_i$ is the medium transverse admittance. Figure 2.5a shows the TE reflected energy $|r_{TE}|^2$ when a plane wave traveling in a relatively resistive medium ($\epsilon_{r1} = 10$ and $\sigma_1 = 0.01$ S/m) strikes an interface, which delimits a second medium with different EM properties. The permittivity contrast dominates the reflected energy when σ_2 is lower or in the same range of σ_1 ; when $\sigma_2 \gg \sigma_1$ the conductivity contrast plays the most important role and it causes a large increase of the reflected energy. Production wells are located

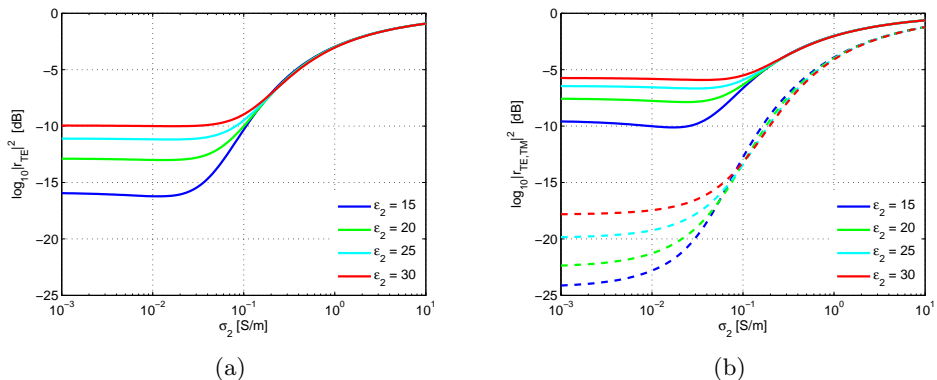


Figure 2.5: Reflectivity of a single planar interface with varying properties of medium 2 at 100 MHz. Medium 1 has fixed properties: $\epsilon_r = 8$ and $\sigma = 0.01$ S/m. Reflection amplitude squared is shown for normal incidence (a) and for an incidence angle of 45° (b), as a function of conductivity of the second medium. Solid lines represent TE mode and dashed lines represent TM mode. Reflectivity is expressed in dB, therefore 0 reflectivity corresponds to total reflection.

in resistive medium (i.e. hydrocarbons), whereas water or steam fronts delimit regions with a much higher permittivity and conductivity. This implies a prior ideal condition for strong reflections. The magnitude of the reflected energy depends on the polarization of the incident wave and the angle of incidence. In case of normal incidence, $|r_{TE}|^2$ is equal to $|r_{TM}|^2$, since both TE and TM waves are polarized parallel to the interface. As soon as the angle of incidence θ is non zero, TE waves present a higher reflectivity, TM waves, instead, are less reflected, because they are polarized in the plane perpendicular to the interface and tend to be transmitted (fig. 2.5b). The difference between $|r_{TE}|^2$ and $|r_{TM}|^2$ is relevant in the region where the permittivity contrast dominates. These considerations make TE wave measurements more powerful than TM measurements. We deduce that an array of sources and receivers would allow to exploit the higher reflected energy of oblique reflections. However, this benefit can vanish, since the signal has to travel for a longer path and consequently the propagation-attenuation increases. A comparison of figures 2.5a and 2.5b shows a reflectivity increase of 5 dB when the incident angle changes from zero to 45 degrees. However, a target located 4 m away for a normal incidence results in an additional path of about 3.2 m for a 45° incidence. This would cause an attenuation of about 30 dB, which results in a net reduction of 25 dB in the contribution from a reflection coming from 45° .

2.4 System Performance of a borehole radar system

The operating performance of a radar tool can be expressed in terms of the Radar Range Equation (RRE). RRE is a simple form of modeling, useful to estimate depth of penetration and signal magnitude that can be expected. Following the approach described by Noon *et al.* (1998), we derive the RRE for smooth planar interfaces:

$$SP = \left[\frac{|\Gamma|^2 e^{-4\alpha R_{\max}} \lambda^2}{64\pi^2 R_{\max}^2} \right]^{-1}. \quad (2.8)$$

The left hand side of equation (2.8) expresses the System Performance (SP) of the radar tool, which is the minimum detectable signal and depends on technical features of the system: transmitting and receiving antenna directional gains, transmitting and receiving antenna coupling efficiencies and transmitted power. On the right hand side are the medium and target-dependent parameters: attenuation α , wavelength λ , reflectivity $\Gamma = |r_{TE}|^2$, which expresses the amount of reflected energy, and maximum penetration depth R_{\max} .

Using equation (2.8), we can estimate the SP that a radar system must satisfy to detect interfaces between two media with different EM properties and for different penetration depths. We use values of α and Γ calculated respectively through equation 2.3 and 2.6. A broad range of EM contrasts at oil-water and oil-steam interfaces in oilfield conditions have been considered, and the calculated SP values are shown in figure 2.6. Medium 1 is modeled with proper ϵ_r and σ of high oil saturation rock, while medium 2 assumes a broad range of values characteristic of rock saturated by undesired fluids like water or steam. Permittivity variation of the remote medium does not affect the SP (fig. 2.6a); instead, conductivity variation does: a conductivity increase causes a reduction of the SP needed to detect the same interface (fig. 2.6b). Therefore, larger penetration depths are feasible if the discontinuity has a strong conductivity contrast; investigation depths slightly larger than 5 meters can be achieved with typical SP of current radar systems being around 100 dB and an operating frequency of 100 MHz. In figure 2.6b we see that a planar interface located 5 m away from the source requires a SP of approximately 100 dB when σ_2 is in the same order or less than σ_1 ($\sigma_2 \leq \sigma_1$); for $\sigma_2 = 1$ S/m, SP reduces to 85 dB, larger values of σ_2 yield a slight decrease of SP. For the model considered in the next section a large contrast between σ_1 and σ_2 may not be realistic and to investigate the worst case

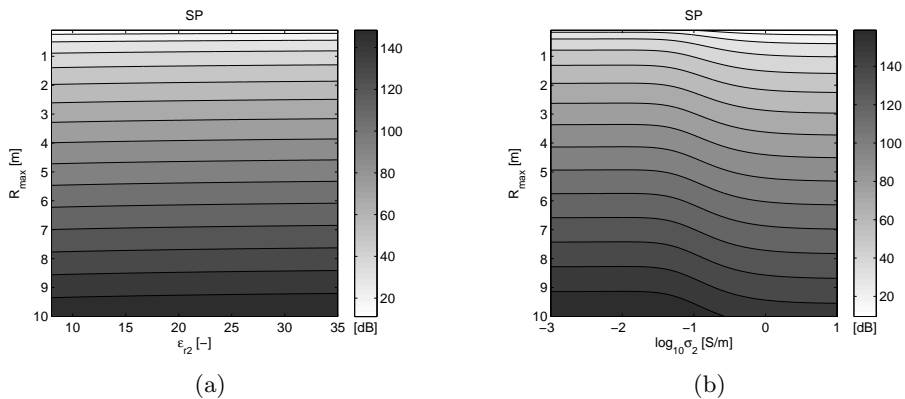


Figure 2.6: System Performance SP of a borehole radar tool operating at 100 MHz. EM properties of medium 1 are fixed ($\epsilon_{r1} = 8$ and $\sigma_1 = 0.01$ S/m); medium 2, instead, has a fixed conductivity $\sigma_2 = 0.5$ S/m and variable relative permittivity ϵ_{r2} (a) and fixed $\epsilon_{r2} = 20$ and variable σ_2 (b).

scenario, we consider σ of the remote medium (σ_2) equal to the one of the oil sand formation (σ_1).

2.5 SAGD model

In this section we analyze the radar feasibility for different stages of a Steam Assisted Gravity Drainage (SAGD) process. We define a typical heavy oil environment, where the oil is located in a sand layer that is embedded in layers of shale. In the upper region of the reservoir there is the injection well, used to inject steam. The steam reduces the high viscosity of the heavy oil and makes the oil drain toward the production well, located in the lower part of the reservoir. We give the formation EM properties in agreement with measured ϵ and σ for representative samples taken from the Athabasca Oil Sand deposits (Chute *et al.*, 1979); for the reservoir: $\epsilon_r = 8$, $\sigma = 0.01$ S/m; for the shale: $\epsilon_r = 14$, $\sigma = 0.2$ S/m; for the reservoir invaded by steam: $\epsilon_r = 20$, $\sigma = 0.01$ S/m). We locate an EM source in the upper part of the production well, which is modeled as a Perfect Electric Conducting (PEC) medium. The EM source is not in contact with the PEC medium, but is surrounded by a dielectric medium ($\epsilon_r = 30$, $\sigma = 1e - 4$ S/m). The receiver is set at the same position as the source, like in a monostatic radar system. The time waveform and amplitude spectra of the EM source are the same as the ones depicted in figure 2.3. The space domain is delimited by absorbing boundary conditions that do not introduce artificial reflections (Giannopoulos, 2008).

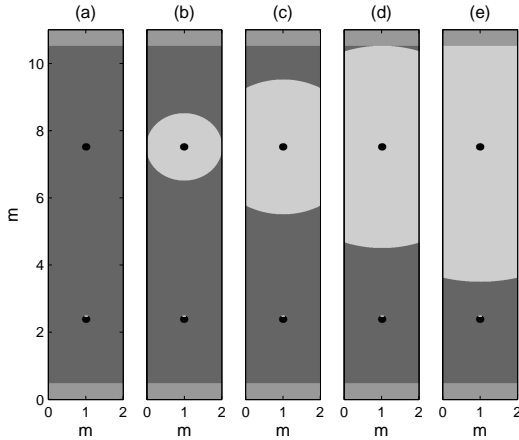


Figure 2.7: Model geometry for different stages of the SAGD process: background condition (a) and steam, respectively, 4 m (b), 3 m (c), 2 m (d) and 1 m (e) from the source.

We simulate the background scenario and four following stages of a SAGD process, when the steam is respectively 4 m, 3 m, 2 m, and 1 m from the source. The steam is modeled spreading homogeneously and isotropic. In figure 2.7 it is possible to see the model geometry for the different stages of the SAGD process.

The results are presented in a time-lapse manner, since we are interested in changes over time. The response of the background medium (i.e. unchanged part of the response) is subtracted from the response of each following stages. Figure 2.8 shows the results for the optimal scenario where the well casing is not considered and the source is located inside the formation. For every panel the steam front reflection, which arrives earlier and earlier as the steam advances, is clearly visible. In the first panel when the steam is 4 m from the well, we see a secondary event at later times. This corresponds to the reflection from the upper boundary of the steam chamber; in the following panels we cannot distinguish this event because the EM wave has to travel a longer path and consequently the event is strongly attenuated. The reflection from the lower shale is removed through the background subtraction.

2.5.1 Wellbore casing

The radar antenna should be at or outside the production well and operate during production, therefore it is necessary to consider the interaction of the metal casing with the emitted signal. With respect to the EM properties

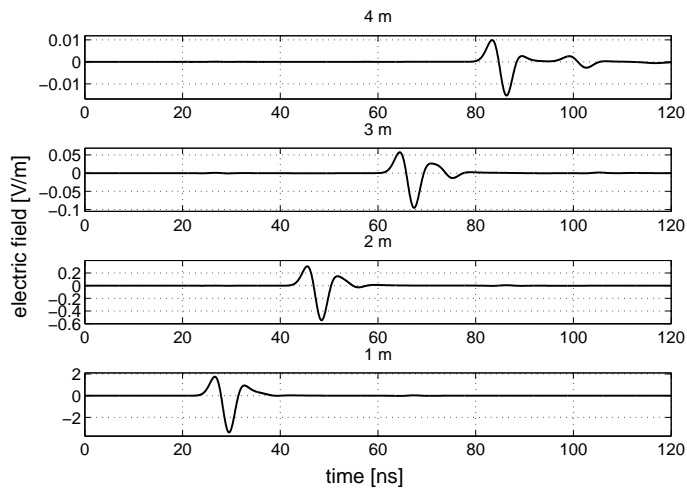


Figure 2.8: Time-lapse EM responses for 4 stages of a SAGD process when the well casing is not considered in the model geometry.

of the geological materials, the metal casing has much higher values of the electric conductivity ($\sigma \gg 10^2$ S/m) and it will generate very strong reflections. If the source is too close to metal components, there will be destructive interference between the emitted signal and the metal reflections. Figure 2.9 shows how the amplitude of the source is affected by the proximity of a metal component: the different curves correspond to increasing distances between source and metal. When the EM source is in contact with the metal component, there is a total destructive interference, due to the fact that metal reverses the polarity of the signal; moving away the source from the metal into the formation, the amplitude increases, since the metal reflections are delayed.

A practical solution can be the employment of a high dielectric medium surrounding the EM source such as used in van Dongen *et al.* (2002). A dielectric shield located inside the wellbore can avoid the destructive interference and its thickness controls the amplitudes of the reflections. In figure 2.10 we show the reflections of a steam front approaching the production well, where the radar sensor is located, for different thickness of the dielectric shield. We plot the time-lapse differences in a different scale for every panel to make the reflections visible in all the scenarios. We calculate an amplitude increase of about 45 dB from the 4 m to the 1 m scenario for all the shield thicknesses considered.

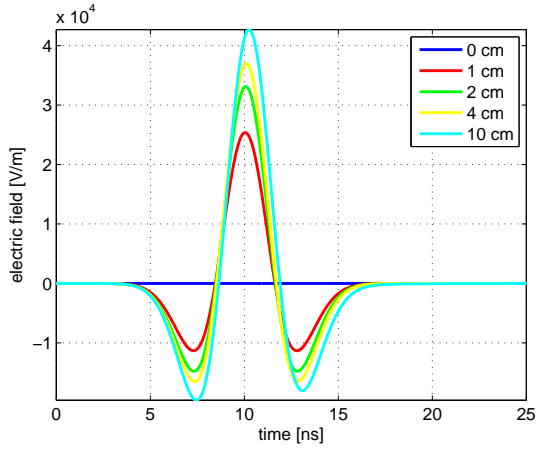


Figure 2.9: Emitted signal as a function of the distance between the EM source and the metal wellbore.

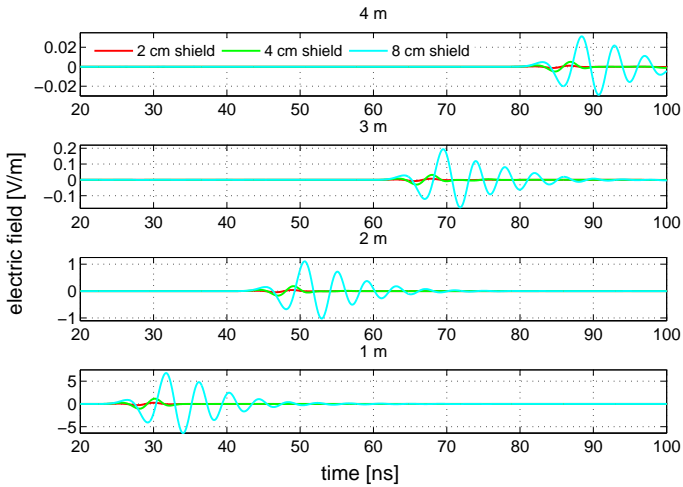


Figure 2.10: Time-lapse differences for different thickness of the dielectric shield, which protects the EM source from the metal reflections.

2.5.2 Reservoir scenarios

Additional constraints can rise due to changes in the heterogeneity of the reservoir background and/or due to gradual fluid saturation transitions. We analyze these scenarios independently. A heterogeneous background itself is not problematic for monitoring applications, as long as it does not change over time. However, the electric properties of the background are mainly controlled by the fluid saturation and the continuous fluid movement during production can cause time-lapse changes in the background heterogeneity. To investigate how these changes affect the target reflections, we consider three levels of time-lapse heterogeneity changes. We make the EM properties of the background medium, the oil saturated rock, randomly vary in ranges of values with the same mean but increasing standard deviations. For the first level of time-lapse changes the relative permittivity varies from 7.8 to 8.2, then 7-9 followed by 6-10. In figure 2.11 each row of images represents a different level of time-lapse changes of the background and each column of images different positions of the steam front. In each image the x-axis describes 10 simulations of different scenarios with the same level of time-lapse change, but different configuration of the heterogeneity. Increasing the level of time-lapse change reduces the visibility of the steam front reflections. In fact, in the first row of images, the target reflections are clear for all the SAGD stages, respectively at 90, 70, 50 and 30 ns. In the second row, instead, the reflection of the steam at 4 m is not clear and in the third row the target reflections are visible just for the last SAGD stages. In reality we expect systematic rather than random changes of the background; therefore, the background subtraction should be more effective in removing the clutter. Anyway, the level of EM changes in the background heterogeneity is an important parameter to consider.

Regarding the transition zone from oil saturated rock to steam saturated rock we consider different lengths of the transition zone. The steam front is located at 2.5 m from the EM source and the EM properties of the transition zone gradually change from the properties of the oil rich rock to the ones of the steam rich rock. Figure 2.12 shows the dependence of the reflected amplitude to the length of the transition zone: the larger the transition zone, the lower the amplitude of the reflection.

2.6 Conclusions

It is well known that the combination of monitoring and control strategies always enhances production and mitigate reservoir uncertainties. We propose that a borehole radar system could be used as a new monitoring tool to

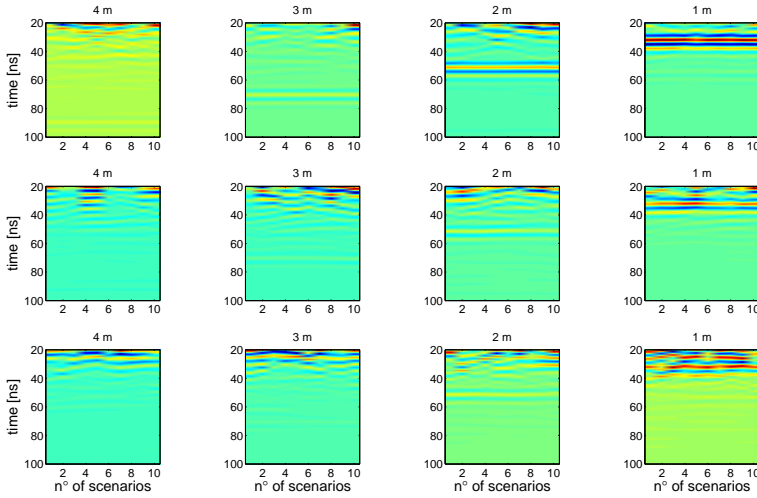


Figure 2.11: Different levels of time-lapse change in the background heterogeneity of consecutive SAGD stages. For each graph the y axis represents the time in ns and the x axis represents 10 simulations of scenarios with the same level of time-lapse change but different configuration of the heterogeneity. The color scale represents the electric field [V/m].

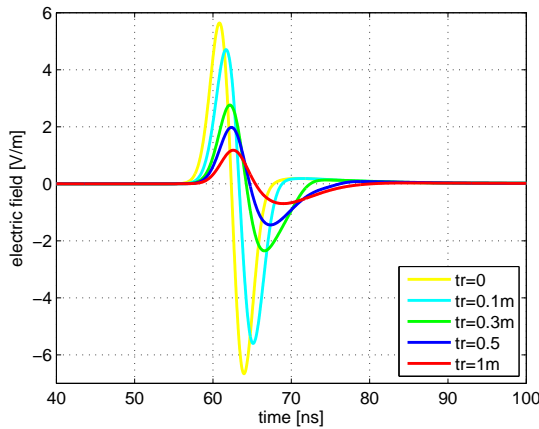


Figure 2.12: Time-lapse differences for different level of transition between an oil saturated rock and a steam saturated rock.

probe the near-well region of several meters. A borehole radar system would provide deeper monitoring data than the ones currently acquired by pressure and temperature sensors, so it would allow choosing better control strategies and sweeping the reservoir in a more effective way. We used 1D modeling in a feasibility study and investigated the effects of EM wave propagation and reflection in a wide variety of possible reservoir conditions. We found that the main constraint is the conductivity of the formation where the radar system is located; a high conductivity makes attenuation and phase distortion too high for wave propagation. Detection of the steam/water front seems possible at 4 m away from the production well, when the reservoir conductivity is below 0.02 S/m. This makes it especially suitable for application in thin oil rims or SAGD processes where the depth to be monitored fits the potential depth of investigation of a radar system. We used 2D FDTD modeling for a more thorough analysis of the main technical limitations and reservoir constraints that could hamper the implementation of this technology. We found that the metal components of the wellbore casing could destructively interfere with the signal emitted by the radar sensor. We suggest that a high dielectric medium around the sensor can increase the amplitude of the reflected signal and overcome the interference problem. Additional reservoir constraints are given by a high degree of time-lapse heterogeneity changes of the EM properties and a steam/water transition zone in the order of the dominant wavelength. These can affect the depth of investigation and the resolution of a radar system. However, for the systematic changes in background EM properties as expected under real field conditions and for realistically estimated thicknesses of the steam/water-oil transition zone, the proposed GPR technology appears a valuable monitoring tool. Further work is necessary to study more sophisticated reservoir models and to evaluate the benefits of a borehole radar implementation in combination with control strategies.

Chapter 3

Coupling reservoir to EM and fluid flow modeling²

3.1 Introduction

Over the past decade, ground penetrating radar (GPR) has become an increasingly popular tool for non-destructive characterization of the soil water content (Huisman *et al.*, 2003; Annan, 2005a). As the contrast between the dielectric constant of water and the other soil and rock components is large, the distribution of water in the subsurface strongly affects GPR wave propagation. As a result, fluid saturation changes can be monitored by time-lapse GPR measurements; successful studies for water monitoring can be found in e.g. Tsoflias *et al.* (2001), Talley *et al.* (2005), Day-Lewis *et al.* (2006), Deiana *et al.* (2008), Tsoflias & Becker (2008) and Kuroda *et al.* (2009) and for steam monitoring in Gregoire *et al.* (2006). Although the mentioned literature is mainly devoted to shallow subsurface environments, knowledge of the fluid distribution and flow is highly desired at larger depths. In the oil industry there is a need for new monitoring techniques that could investigate the neighborhood of production wells (Bachrach *et al.*, 2008; Davies *et al.*, 2008). Smart well sensing technology and conventional geophysical methods like seismics and resistivity sounding can poorly image the near-well region, while the increasing exploitation of unconventional and thin reservoirs requires the monitoring of this zone.

Reservoir heterogeneity and additional factors such as pressure gradients, unexpected compartmentalization and sub-seismic fracturing may cause an

²This chapter has been published as journal paper in *Geophysics* **76**(3), A21-A25 (Miorali *et al.*, 2011). Note that minor changes have been introduced to make the text consistent with the other chapters of the thesis.

uneven fluid front and early breakthrough of undesired fluids like water and steam in a localized section of the well. Mapping reservoir fluid saturation changes offers the possibility to detect fluid fronts sufficiently in time to apply effective control strategies and, for example, reduce production from concerned segments. Early detection and control decrease the unevenness of fluid fronts, leading to potential increased benefits in oil production (Ebadi & Davies, 2006).

Numerical studies have already evaluated the feasibility of GPR technology for different oilfield applications (Chen & Oristaglio, 2002; Heigl & Peeters, 2005). In the previous chapter we have proposed that an array of downhole radar sensors can satisfy the monitoring requirements in suitable oilfield environment. In this chapter we carry out integrated numerical modeling where flow simulations are coupled to EM simulations. We use well established mixing models to relate the evolving fluid saturation distribution and the EM properties, as proposed by Wilson *et al.* (2009). A numerical experiment is performed to quantify the system performance required by a radar system to record water reflection events. We evaluate feasible investigation depths in a bottom water-drive type of reservoir and discuss the challenges of a potential borehole radar implementation.

Pioneering borehole radar tools fixed in the subsurface have been proposed for monitoring the movement of water levels at considerable depths (Ebihara *et al.*, 2006; Sato & Takayama, 2007) and EM logging tools have already proved the GPR potential in imaging the neighborhood of a well (Liu *et al.*, 2004; Mason *et al.*, 2008). We believe our study can stimulate research in order to allow an innovative and promising application for GPR technology.

3.2 Numerical experiment

We run a 2D numerical experiment representative of a bottom water drive reservoir characterized by high permeability streak. Source of inspiration was a conceptual model analyzed by Addiego-Guevara & Jackson (2008), a thin sandstone reservoir containing inter-bedded, laterally discontinuous shale barriers that reduce the effective vertical permeability. The porosity and permeability distributions, shown in Figures 3.1a and 3.1b, were created using an in-house geostatistical modeling software based on Principal Component Analysis; a large number of realizations of typical geological features are used to create the final image (Sarma *et al.*, 2008). We consider a single horizontal production well and we focus on a limited section of the reservoir close to the well; the model domain is 60 m long and 10 m high.

We numerically solve the porous media two-phase flow equations with an implicit pressure explicit saturation (IMPES) scheme (Aziz & Settari, 1979). It is fair to note that this approach reduces the complexity of a real flow process and describes a specific production scenario. The bottom boundary is assumed an infinite aquifer, while the top and sides are no flow boundaries. A horizontal well is located at the top of the domain with a fixed liquid production flow rate along the entire segment. For the EM simulation we use GprMax, a general purpose FDTD GPR simulator (Giannopoulos, 2005). In the model the materials are treated as lossy dielectrics and the constitutive parameters are frequency independent. Perfectly Matched Layer (PML) boundary conditions have been used in order to avoid reflections from the boundaries. The source is modeled as a first derivative of a Gaussian pulse with a center frequency of 100 MHz. The radar sensors are placed in the production well and they are modeled in a monostatic configuration, EM source and receiver in the same place. In figure 3.1 the gray box at the top of the domain represents the production well and the red dots the array of sensors along the well. The key parameters to run the reservoir and EM simulations are presented in table 3.1. The rock and fluid properties for the flow simulations are chosen in agreement with values of similar reservoir models (Addiego-Guevara & Jackson, 2008; Jansen *et al.*, 2002); see chapter 2 for an analysis of the EM properties at reservoir conditions and their effect on radar wave propagation. Archie's parameters are representative of a sandstone reservoir.

The key reservoir property for determining the EM parameters is the water content θ , the product of porosity and water saturation. To obtain the relative permittivity we used the Complex Refractive Index Model (CRIM) proposed by Birchak *et al.* (1974) for two reasons: it is the most widely accepted dielectric mixing model and a remarkably good agreement has been found in modeling the dielectric properties of geological materials (Knight, 2001; Seleznev *et al.*, 2004). To obtain the effective electrical conductivity we have used Archie's law (Archie, 1942). The CRIM model and Archie's law are the key elements in linking the reservoir and the EM simulations. As the water approaches the production well in the reservoir simulation, the distribution of the fluid saturations is extracted at predetermined times and it is converted in EM properties distribution to allow EM simulation at those times.

Table 3.1: Reservoir and EM model properties.

Reservoir rock and fluid properties		
<i>Parameter</i>	<i>Value</i>	<i>Units</i>
Oil compressibility	10^{-9}	1/Pa
Water compressibility	10^{-9}	1/Pa
Rock compressibility	10^{-9}	1/Pa
Oil Density	900	kg/m ³
Water Density	1000	kg/m ³
Oil viscosity	0.5e-3	Pa s
Water viscosity	1e-3	Pa s
Oil end-point relative permeability	0.9	-
Water end-point relative permeability	0.6	-
Corey exponent for oil	2	-
Corey exponent for water	2	-
Residual oil saturation	0.2	-
Connate water saturation	0.2	-
Initial reservoir pressure	40	MPa
EM rock and fluid properties		
Rock relative permittivity ϵ_r	7	-
Water relative permittivity ϵ_w	80	-
Oil relative permittivity ϵ_o	3	-
Water electrical conductivity σ_w	1-5	S/m
Cementation exponent m	2	-
Saturation exponent n	2	-

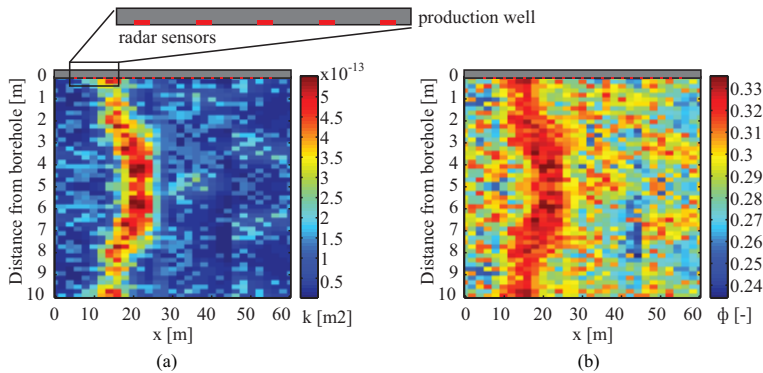


Figure 3.1: Spatial permeability k , expressed in m^2 , (a) and porosity ϕ (b) distribution. The gray box at the top of the domain represents the production well and the radar sensors are depicted by red dots along the x direction with an interval spacing of 2.5 m.

3.3 Results and discussion

For every water content distribution extracted from the reservoir simulation we run the EM simulations. The EM response of the background medium, which is the unchanged part of the response, is subtracted from the response at each of the following stages.

Figure 3.2 shows a snapshot of the linking process for the 200-day reservoir simulation time. We extract the water content distribution (Figure 3.2a), we convert it in EM properties, relative permittivity ϵ_r (Figure 3.2b) and electrical conductivity σ (Figure 3.2c) and we obtain a 2D image of the EM responses (Figure 3.2d). An automatic gain control was applied to enhance the reflection events at later times. As a result of the permittivity increasing between formation and the water flooded rock, the reflections present a positive main lobe, the reverse of the direct wave polarity. A qualitative comparison of Figure 3.2a and Figure 3.2d reveals that the two models are effectively linked. The water front shape can be approximately reconstructed from the radar image.

Nevertheless, to get such an image it would be necessary to equip the well with a dense array of radar sensors and this may not be feasible due to the cost of the implementation. Therefore, it makes more sense to analyze the data that we can acquire from a single sensor. Figure 3.3 shows for a few sensors, located at different x positions, the evolution of the time-lapse differences of the 1D traces. Each image represents an up-dipping event that corresponds to the advance of the water front. The slope of the events expresses the rate of change of the fluid distribution: a significant up-dipping

slope can be interpreted as a fast water advance and a smooth slope as a slow water advance. The highest slope of the up-dipping events is observed in the image obtained from the radar sensor located in the proximity of the high permeable streak, Figure 3.3b.

Both in Figures 3.2d and 3.3 no events are recognizable at times earlier than the water front reflections. This is because in the oil saturated portion of the domain there are no changes of the water content distribution over time. Therefore, the subtraction of the electric field of the following steps with the background condition removes all the small reflections expected from the heterogeneous distribution of the EM properties.

Figure 3.4 shows the normalized instantaneous amplitude of the reflected events of figure 3.3b in a dB scale, which represents the System Performance (SP) a radar system would need to record the reflections. We consider the effect of different values of the formation water electrical conductivity σ_w . Figure 3.4a is generated with the EM paramtetrts shown in table 3.1. All the first arrivals are above -80 dB; this can be achieved with commercially available GPR technology, with system performances of about 120-160 dB (Davies & Annan, 1989). We clip all the SP values below -90 dB, this is a safe assumption for the detectability of the signal. Figures 3.4b, 3.4c and 3.4d show SP for σ_w respectively equal to 2, 3 and 5 S/m. We see that the depth of investigation significantly decreases with increasing σ_w , which results in the main limitation for the implementation of down-hole radar technology.

Down-hole radar systems for oilfield applications are not currently available, but we believe the current technology has the potential to develop such systems. The main practical challenge is the metal casing interference with the EM signal. The antenna has to be in contact with the formation and separated from the metal components by a material with high dielectric constant, in this way no metal hinders the radar wave propagation, but constructively interferes with the emitted signal as discussed in chapter 2. This can be achieved by making suitable slots in the casing or by placing the antennas outside the casing.

Low frequency EM noise generated by cables and the radar system itself is negligible due to the high frequency range of radar waves. Once installed, radar sensors allow semi-continuous acquisition avoiding common 4D seismic issues such as temporal aliasing and spatial shifts. The main source of noise would be time-lapse changes of the EM properties in the background medium; this issue can be solved by increasing the data acquisition frequency relative to the rate of the local temporal changes or by enhancing the up-dipping events with an f-k filter.

Borehole radar measurements would extend the monitoring capability of

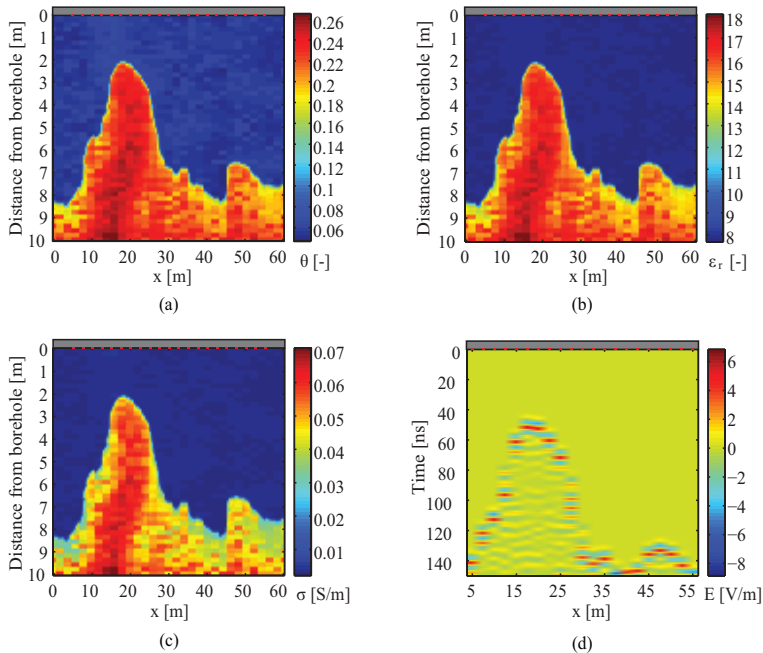


Figure 3.2: Snapshot of the water content θ distribution after 200 days of reservoir simulation (a) and respective relative permittivity ϵ_r (b) and electrical conductivity σ (c) distribution. Figure 3.2d shows the 2D radar scan; the red dots represent the radar sensors.

the sensing techniques currently used in smart wells. This would result in an increase of the efficiency of the control strategies and a reduction of the uncertainties of the dynamic reservoir models (Addiego-Guevara & Jackson, 2008; Jansen *et al.*, 2008). The typical range of detection in the order of ten meters is particularly suitable for bottom water-drive reservoirs with a thin oil layer or for heavy oil reservoir produced by steam assisted gravity drainage. In this study we consider vertical high permeability streaks as the main source of uneven fluid fronts; however, additional factors, such as wellbore friction or sub-seismic fractures may make GPR monitoring suitable in other geological scenarios.

3.4 Conclusions

Borehole radar is a promising technique to image and monitor the near-well region of a production well. However, field trials have to be first validated by a thorough modeling study. By linking reservoir and electromagnetic simulations it is possible to generate radar responses for realistic reservoir

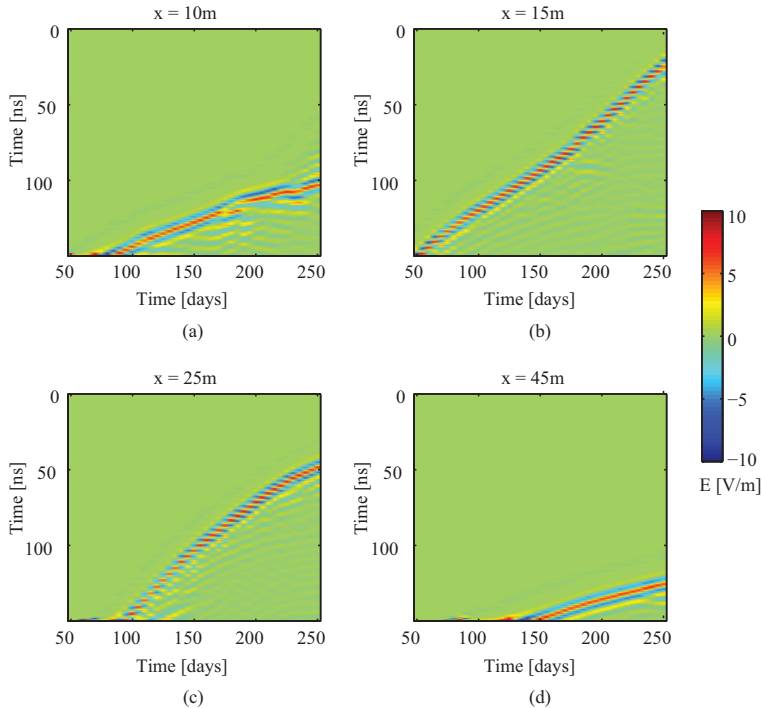


Figure 3.3: Evolution of the time-lapse 1D traces for different x locations of the radar sensors. For every image the y direction represents the time in ns and the x direction the sequential different time steps, the color scale represents the time-lapse amplitudes of the electric field (V/m).

scenarios. The EM simulation results reveal that GPR is capable of monitoring fluid saturation changes and a qualitative analysis is suggested to evaluate the advance of a non-uniform water front. Water front reflections in the range of tens of meters are detectable in a low conductivity reservoir environment ($\sigma < 0.02$ S/m). The electrical conductivity of the formation water is the main limiting factor of the monitoring capability of radar waves. In favorable conditions radar measurements could be used to improve well control strategies and to constrain the reservoir models with semi-continuous monitoring data.

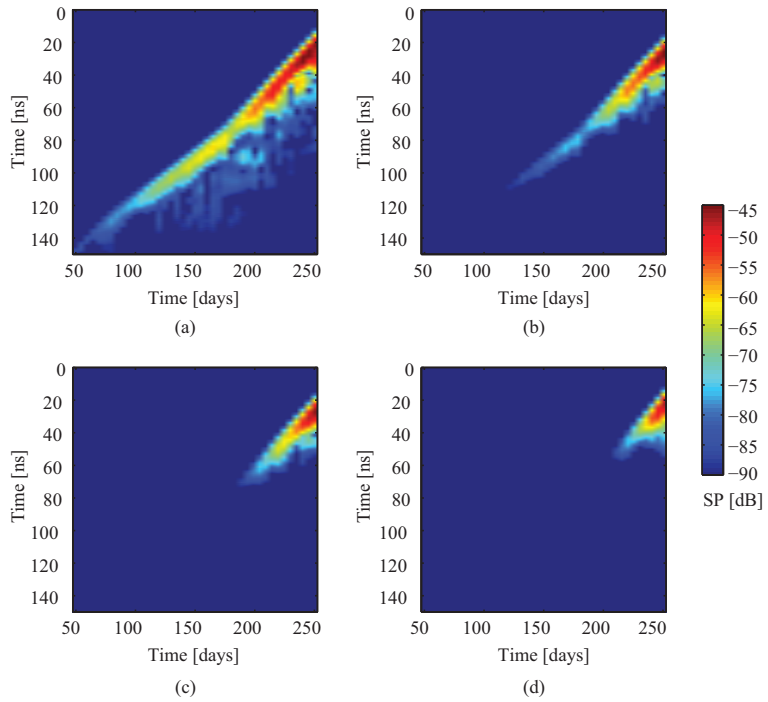


Figure 3.4: System Performance (SP) necessary to record the reflection events at the radar sensor located at $x=15$ m for different values of σ_w , respectively 1 S/m (a), 2 S/m (b), 3 S/m (c) and 5 S/m (d).

Chapter 4

GPR monitoring of oil displacement by waterflooding: A laboratory study³

4.1 Introduction

Ground Penetrating Radar (GPR) has become an increasingly popular tool for non-destructive imaging of the near-surface environment. Due to the high sensitivity to water saturation, successful applications consist of measuring and monitoring the water content distribution in the shallow subsurface. A review of GPR methods for measuring the near-surface water content can be found in Annan (2005a) and Huisman *et al.* (2003), some successful case studies of time-lapse water monitoring are described in Tsoflias *et al.* (2001), Talley *et al.* (2005), Saintenoy *et al.* (2008), Deiana *et al.* (2008), and Kuroda *et al.* (2009).

A related popular use of GPR concerns assessing time-varying concentrations and distributions of oil derived liquids, so called Non-Aqueous Phase Liquids. The low dielectric permittivity of these NAPLs with respect to water makes GPR highly suitable for the detection. A considerable number of papers exists in the literature focused on the application of GPR profiling to the detection and monitoring of NAPL contaminant plumes in the field (e.g. Daniels *et al.*, 1995; Campbell *et al.*, 1996; de Castro & Branco, 2003; Cassidy, 2007; Hwang *et al.*, 2008) and on laboratory studies showing results of controlled release experiments (e.g Kim *et al.*, 2000; al Hagrey, 2004; Bano

³Part of this chapter has been submitted as journal paper in *Geophysics*. Note that major changes have been introduced to make the text consistent with the other chapters of the thesis.

et al., 2009).

Most GPR literature related to oil is devoted to near-surface applications; however, some numerical studies have already evaluated GPR technology as a potential sensing tool for oilfield applications (Chen & Oristaglio, 2002; Heigl & Peeters, 2005; Miorali *et al.*, 2011). For example, a major concern is the undesired premature water breakthrough in localized sections of production wells (Addiego-Guevara & Jackson, 2008). Water usually displaces oil “pushing” it toward the production wells. Techniques that can map fluid saturation changes and water front arrivals in the near-well region can be extremely useful for production optimization purposes. To assess the GPR potential for such an application, an experimental setup has been developed mimicking an oil reservoir swept by waterflooding in a near wellbore environment.

All the experiments were conducted in a meter-scale sand box and with different types of radar systems. An off-ground Stepped Frequency Continuous Wave (SFCW) radar system was used mainly to quantitatively characterize the dry sand conditions, whereas an impulse radar system was used to qualitatively monitor water injection experiments. Two types of dynamic experiments were performed: the first consisting of water flooding the sand box under inhomogeneous low water saturation conditions, the second of waterflooding the mainly oil saturated sand box leading to a displacement of oil out of the box. For calibration purposes, some of the experiments were simultaneously monitored by impedance measurements taken along a vertical profile in the sand box.

4.2 Material and methods

4.2.1 Experimental set up

A plastic cylindrical box (1.05 m in height, 0.55 m radius and a 0.01 m thick wall, with an approximate volume of 1 m³) is used for the water flooding experiments. Approximately 800 kg of fine quartz sand with grain size diameters between 0.3 and 0.5 mm were distributed into the box in layers in an attempt to achieve a layered structure closer to real field conditions; the cumulated thickness was 0.5 m and the average porosity calculated through the volume/density method is 0.3. The box is located 25 cm above the ground surface on a wooden frame. A metal sheet was located between the wooden frame and the sand box bottom to create a significant reflector. The experimental set up is shown in figure 4.1. Note that the thermocouples were not used for the presented experiments.

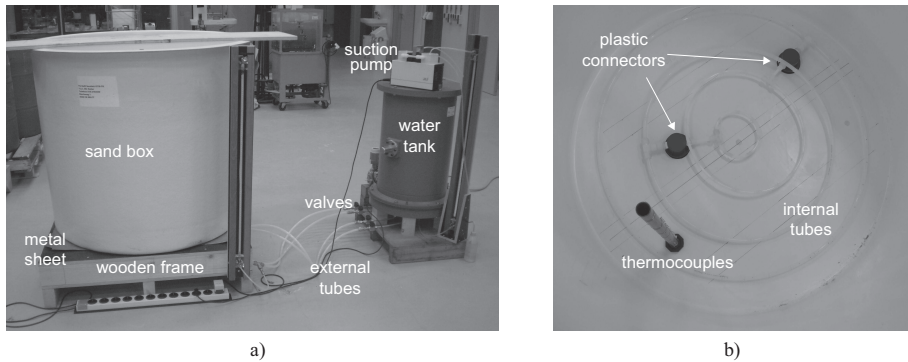


Figure 4.1: Experimental set up (a) and plan view of the internal bottom of the sand box (b).

The water injection is regulated via four circular tubes located at the inside bottom of the box. These tubes were perforated along all their lengths with holes of 3 mm diameter covered by a fine net (mimicking a sandscreen) to prevent the inflow of sand in the tubes. This way the water could spread homogeneously along the bottom surface leading to a uniform water front. The internal tubes were connected to a second cylindrical tank (0.74 m height and 0.2 m radius, with an approximate volume of 93 l), where the water was stored. The bottom of the sand box was perforated at two points, where two plastic connectors linked the internal tubes with four external tubes and the water tank. The amount of water injected was manually measured through a meter scale tube connected to the water tank.

The water injection was performed either at constant pressure or at constant injection rate. A constant pressure was obtained keeping the water height in the water tank (green vessel in figure 4.1) at a fixed height, i.e. higher than the sand surface height. The experiments at constant injection rate were performed manually by increasing the water pressure through a compressor. A hole placed on the side of the sand box was made a few centimeter below the sand surface to allow fluids to spill out (visible in figure 4.2).

4.2.2 Monitoring systems

Two types of ground penetrating radar were used: a commercial impulse system and a SFCW (Stepped Frequency Continuous Wave) in-house system. The impulse system consists of a PulseEKKO PRO connected to 1GHz bi-

static ground-coupled antennas. The antennas were kept at a fixed position in the middle of the sand box.

The SFCW system was set up using a vector network analyzer (VNA - FSH8) combined with an off-ground monostatic horn antenna (BBHA 9120 A). The antenna axial length was 220 mm and the aperture area was 140×240 mm²; its nominal range of frequency is 0.8 - 5 GHz and its isotropic gain ranges from 6 to 15 dBi. The antenna was calibrated at the connection between the antenna feed point and the cable using a 50 Ω OSM (Open, Short, Match) series of high precision standard calibration kit. This established a reference calibration plane to which the frequency dependent complex scattering parameters, S_{11} , between the returned signal and the emitted signal was measured. The parameter S_{11} was measured sequentially at 631 stepped frequencies over the range 0.8 to 2.8 GHz using a frequency step of approximately 3.2 MHz.

In addition to the radar acquisition, electrical impedance measurements were taken. A tube equipped with 50 pin electrodes was vertically placed inside the sand. The electrodes were distributed every cm along the tube length and they were connected to an impedance analyzer (Wayne Kerr 6440A). Impedance measurements between near pair combinations of electrodes, for a total number of 49 pairs, allowed measuring the vertical electric impedance profile during the injection-drainage experiments. The first electrode pair corresponded to the sand box bottom, while the 49th pair is slightly above the sand surface, consequently the pair number is approximately representative of the sand height. The amplitude of the impedance was measured at a fixed frequency of 10 kHz. All the monitoring systems are shown in figure 4.2.

4.2.3 EM Forward and Inverse Modeling

The off-ground SFCW radar system has already been efficiently validated both in laboratory and field conditions (Lambot *et al.*, 2004, 2006, 2008a). The frequency domain measured transfer function S_{11} is expressed as the ratio between the reflected $Y(\omega)$ and emitted signal $X(\omega)$:

$$S_{11}(f) = \frac{Y(f)}{X(f)} = H_i(f) + \frac{H(f)G_{xx}^\uparrow(f)}{1 - H_f G_{xx}^\uparrow(f)}, \quad (4.1)$$

where $H_i(f)$, $H(f)$ and $H_f(f)$ account, respectively, for the antenna return loss, the antenna transmitting-receiving transfer function and the antenna feedback loss; $G_{xx}^\uparrow(f)$ is the Green's function, which accounts for the

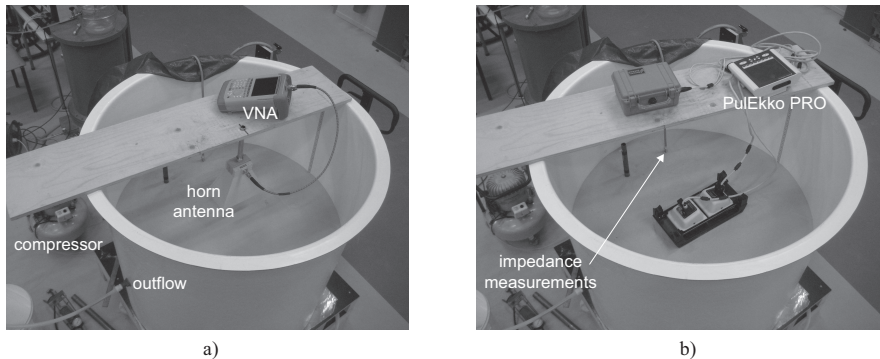


Figure 4.2: Off-ground SFCW radar system (a) and commercial impulse radar system (b). The outflow tube and the location of the electrodes for the impedance measurements are visible respectively in (a) and (b).

backscattered (denoted by the upward arrow) x -directed electric field component (first subscript x) at the antenna phase center for an x -directed electric source (second subscript x) situated at the same position. The air-subsurface system is modeled as a 3D multi-layered medium in which every layer is characterized by constant electric properties. The solution of Maxwell's equations for electromagnetic waves propagating in a multi-layered medium is well known (Michalski & Mosig, 1997; Slob & Fokkema, 2002). Following the approach developed in Slob & Fokkema (2002), the Green's function is derived using a recursive formula to compute the transverse electric and magnetic global reflection coefficients in the spectral domain. The transformation to the spatial domain is performed by evaluating numerically a semi-infinite complex integral (Lambot *et al.*, 2007).

The characterization of the subsurface parameters was performed through full-waveform inversion of the Green's function. An objective function was minimized in the least square sense:

$$\phi(\mathbf{b}) = \left[\frac{\sum_{f_{min}}^{f_{max}} |\mathbf{G}_{xx}^{\uparrow*} - \mathbf{G}_{xx}^{\uparrow}|^2}{\sum_{f_{min}}^{f_{max}} |\mathbf{G}_{xx}^{\uparrow*}|^2} \right]^{1/2}, \quad (4.2)$$

where $\mathbf{G}_{xx}^{\uparrow*} = G_{xx}^{\uparrow*}(f)$ and $\mathbf{G}_{xx}^{\uparrow} = G_{xx}^{\uparrow}(f, b)$ are vectors containing, respectively, the retrieved and the modeled air-subsurface reflection response, \mathbf{b} is the parameter vector to be estimated, and f_{min} and f_{max} stand, respectively, for the minimum and maximum frequency used. The objective function is

minimized by means of the global multilevel coordinate search algorithm (Huyer & Neumaier, 1999) sequentially combined with the Nelder-Mead simplex algorithm (Lagarias *et al.*, 1998).

4.2.4 Water flooding experiments

The water flooding experiments were performed under two types of saturation conditions: sand with an inhomogeneous residual water saturation and sand mainly oil saturated.

Experiments under inhomogeneous residual water saturation conditions

Initially, the sand was air dry; the first transition from dry to fully saturated conditions required the injection of 147 l of water. As a next step, the sand was drained applying a constant negative pressure of minus 0.1 bar through a suction pump (visible in figure 4.1). The drainage lead to an extraction of about 100 l of water and consequently to an inhomogeneous residual water saturation in the sand. Several repetitions of the water flooding experiments were performed under similar conditions and the injection and drainage resulted each time in the same amount of water, $100 \text{ l} \pm 5 \text{ l}$. In this chapter one representative case of this type of experiments is presented.

Experiments under oil saturated condition

To mimic an oil saturated reservoir, the following two steps have been followed: the sand was first fully water saturated, and then a solvent refined mineral oil was poured on the top of the sand surface. The oil slowly drained out the water at the bottom of the sand box and an oil saturated condition with residual water saturation was set. Afterwards, the drained water was injected back into the sand from the bottom and part of the oil was displaced out of the box through the outflow tube. The first time that an oil saturated condition was set, it was possible to inject 105 l of oil into the sand. The progressing oil front descending the sand box was tracked by the electrical impedance measurements along the vertical profile. After the water flooding experiment was performed, the sand was drained through the suction pump and a system presenting a residual water and oil saturation was established. The same procedure was repeated four times; for the following experiments a smaller amount of oil, approximately 80 l, was placed due to the fact that the pores were partially filled both with water and oil.

The water injection was performed in two ways: at constant pressure and at constant injection rate. The first experiment was conducted at a constant pressure of 70 mbar. This experiment was performed in steps, every 6 l of water injected, the injection was stopped and impedance measurements were taken. The total duration of the injection was 11 hours.

The following three experiments were performed at constant injection rate without interruptions; the electrical conductivity of the injected water was, respectively, 0.05, 0.3 and 1 S/m. The injection rate was approximately 0.32 ± 0.018 l per minute, the small variations were considered negligible for the purpose of the experiment. The total amount of water injected was 88 l and the injection time approximately 4.8 hours. When one experiment was finished, the system was drained and additional oil was recovered; afterwards, the sand was saturated with the water that was used during the flooding experiment. Therefore, the conductivity of the residual water saturation of the saline experiments had the same value of the water that was later injected. All the types of the water flooding/ oil displacement experiments are presented in this chapter.

4.3 Results and Discussion

4.3.1 Off-ground radar inversions

Following the approach described in Lambot *et al.* (2006), the transfer functions $H_i(\omega)$, $H(\omega)$ and $H_f(\omega)$ were determined solving a system of equation 4.1 for different model configurations that could be easily modeled. Measurements over a metal sheet at different heights were taken when the sand box was empty. The determination of the transfer functions allows to filter $S_{11}(\omega)$ from the antenna effects and obtain the air-subsurface system model $G_{xx}(\omega)$. Once the measured Green's function is reconstructed, it is possible to use the inversion procedure previously described in section 4.2.3 to retrieve both geometric and electromagnetic parameters of the investigated medium. The inversions were performed for three parameters: the electric permittivity of the dry sand layer, the antenna height above the sand surface and the sand height (i.e. total sand thickness). We repeated this procedure for different heights of the antenna and the sand layer. A good agreement between measured and modeled Green's function was found for all the investigated configurations. In figures 4.3 and 4.4 the comparison between the measured and modeled Green's functions are shown in the frequency and time domains for a dry sand layer of, respectively, 0.25 and 0.5 m.

In table 4.1 the inverted parameters for different heights of the antenna

Table 4.1: Inversion results.

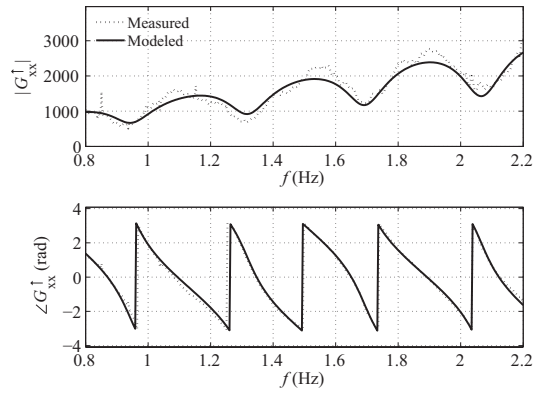
known		inverted		
h_{ant}	h_{sand}	h_{ant}	h_{sand}	ϵ_r
0.17	0.25	0.1759	0.2324	2.9531
0.17	0.3	0.1628	0.295	2.9392
0.15	0.4	0.1535	0.3812	2.9651
0.15	0.5	0.1527	0.4926	2.8236

and the sand layer are shown. The antenna height is considered to be the distance from the sand surface to the antenna phase center, located 7 cm from the antenna aperture. Both the inverted antenna and sand heights are in good agreement with the known heights. There is a small decrease of the permittivity with increasing sand thickness. This is probably due to small variations in compaction, i.e. less compaction for shallow sand layers.

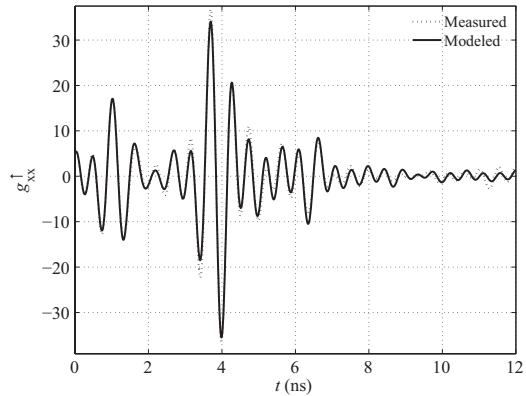
4.3.2 Impedance measurements

Impedance measurements were acquired during the two types of water flooding experiments, injection under residual water saturated conditions and under oil saturated conditions, and during the injection of the oil into the sand. These measurements provide dynamic profiles of the vertical fluid content of the sand, as the electrical impedance is inversely related to the water content of a medium. The measured impedance profiles were used to support the interpretation of the GPR reflections.

Figure 4.5 shows the impedance profiles acquired during a water flooding experiment under residual water saturation conditions. The total amount of water injected was 102 l and the impedance measurements were acquired every 6 l of water injected, so in total 17 profiles, numbered in ascending order. The first profile corresponds to the initial saturation conditions, showing a sharp increase from low to high impedance values for the first electrode pairs followed by a gradual increase. The low impedance of the first electrodes corresponds to the lower part of the sand box that could not be completely drained during the drainage process. In the upper part, the sand has a residual water saturation that results in a quite stable impedance profile. After the injection started, the consecutive profiles show a continuous decrease of the impedance until the sand is fully saturated and resulting in quite stable impedance values. The transition from residual to full saturation conditions in the lower part of the sand is quite gradual with respect to the upper part, which shows a sharper transition. Note that the impedance profiles show

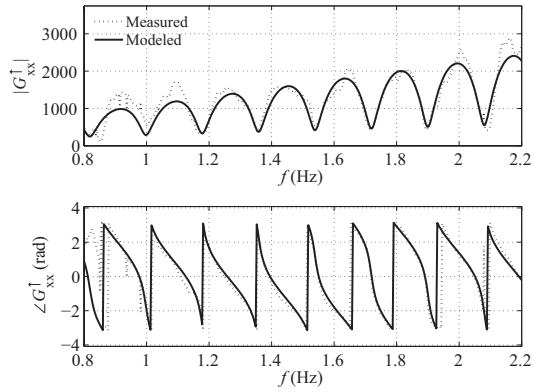


(a)

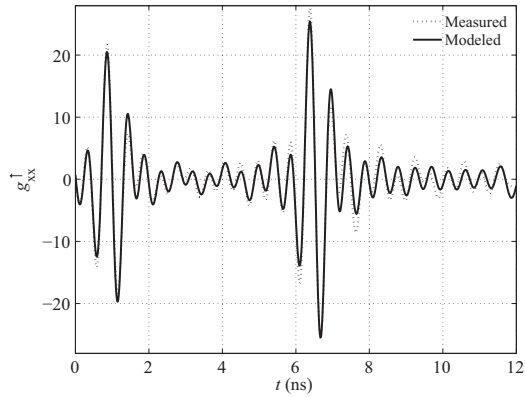


(b)

Figure 4.3: Measured and modeled Green's function for 25 cm of dry sand and the antenna phase center 17 cm off the ground. Data are presented both in frequency (a) and time domain (b).



(a)



(b)

Figure 4.4: Measured and modeled Green's function for 50 cm of dry sand and the antenna phase center 17 cm off the ground. Data are presented both in frequency (a) and time domain (b).

consistent peak values under the residual saturation conditions that are attributed to a poor contact between the sand and the electrodes. These peaks were noticed also for the other experiments and disappeared when the water reached the respective electrodes. The small oscillations in the last profiles, that corresponded to fully saturated conditions, were indicative of variations in the porosity of the sand. The superficial sand layer was less compacted than the underlying layers and presented a higher porosity, which results in a clear decrease of the last impedance profile.

Figure 4.6 shows the impedance profiles acquired during the placement of the oil. An amount of 105 l of oil was poured at the top of the water saturated sand and the profiles were measured every time 6 l of water came out from the bottom of the sand box. Impedance sharply increases from the low values corresponding to the fully water saturated conditions to higher values, indicative of high oil saturations. The impedance rise for the first electrode pairs of the last profile is an indication that the oil reached the bottom of the tank.

Figure 4.7 shows the impedance measurements during the water flooding experiment under oil saturated conditions. These profiles correspond to the experiment performed at constant pressure, which was performed in three runs. The profiles were acquired at the initial conditions of every run and at every 6 l of injected water. The first run included the impedance profile from 1 to 5, the second run from 6 to 16 and the final run from 17 to 19. A sharp impedance decrease is visible between the profiles 3 and 12, whereas the previous and following measurements present a slight reduction. It seems there was a clear oil displacement just after the deeper 20 cm of the sand box. The impedance values do not return to their initial fully water saturated values implying that part of the oil remained in the sand. Significant reorganization of the fluid distribution occurred during the experiment interruptions that were about 10 hours each; it can be observed both in the discontinuities of the radar section and in the impedance measurements, between lines 5 and 6 and 15-16.

4.3.3 Water flooding monitoring

The water flooding experiments were performed first under inhomogeneous residual water saturation and then under oil saturated conditions. The latter type of experiment was performed first at constant pressure and then at constant injection rate with three different electrical conductivity of the injected water. All the experiments were monitored either with the impulse or the SFCW GPR. In this chapter the monitoring results of the impulse system

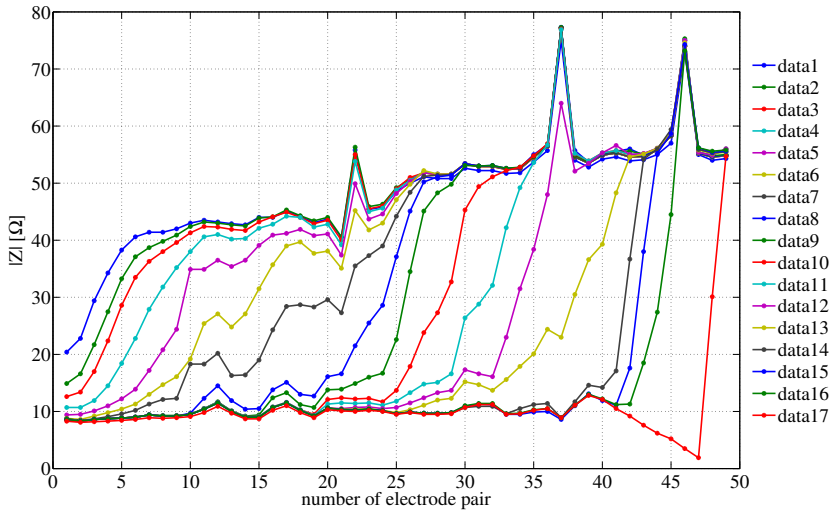


Figure 4.5: Impedance measurements between near pairs of electrodes during a water injection experiment in an inhomogeneous residual water saturation condition.

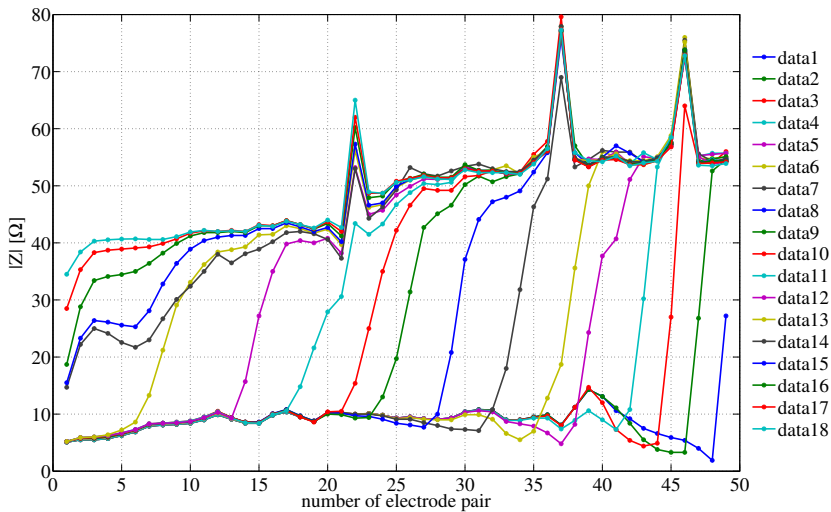


Figure 4.6: Impedance measurements between near pairs of electrodes during the first oil placement process.

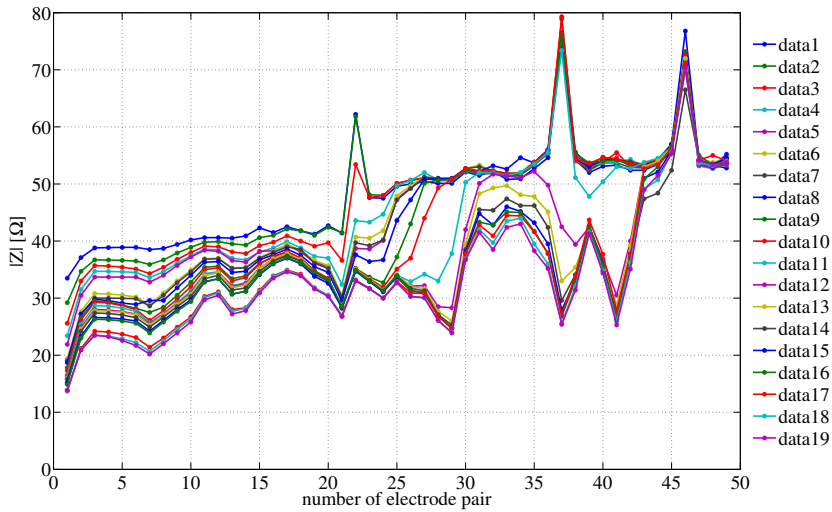


Figure 4.7: Impedance measurements between near pairs of electrodes during the first water flooding experiment in oil saturated condition.

are presented. Basic processing was applied to the raw data: dewow and dc removal. All the traces were aligned using as reference the 5 % of the instantaneous amplitude of the first arrival.

Experiment under inhomogeneous residual water saturation condition

Figure 4.8 shows the radar section of a water injection experiment when the sand box was partially water saturated. The GPR traces were acquired every 20 s. The water front can be clearly monitored in the upper portion of the sand and corresponds to up-dipping events, while in the deeper part, the sand presented higher water saturation at the initial stage and the water rise did not generate a sufficient EM contrast to create a clear reflection. The reflection at about 6 ns at the initial conditions (left section of figure 4.8) is an indication of higher water content in the deeper sand. This is also confirmed from the impedance measurement, in fact the first electrodes of the initial profiles show a significant increase in the impedance amplitude (figure 4.5). The clear down-dipping event correspond to the metal reflection, which was continuously delayed due to the increasing amount of water in the sand and consequent slowdown of the EM waves. Continuous down-dipping events characterize the initial deep sand reflections, indication that water did overpass that reflection events and delayed their arrivals.

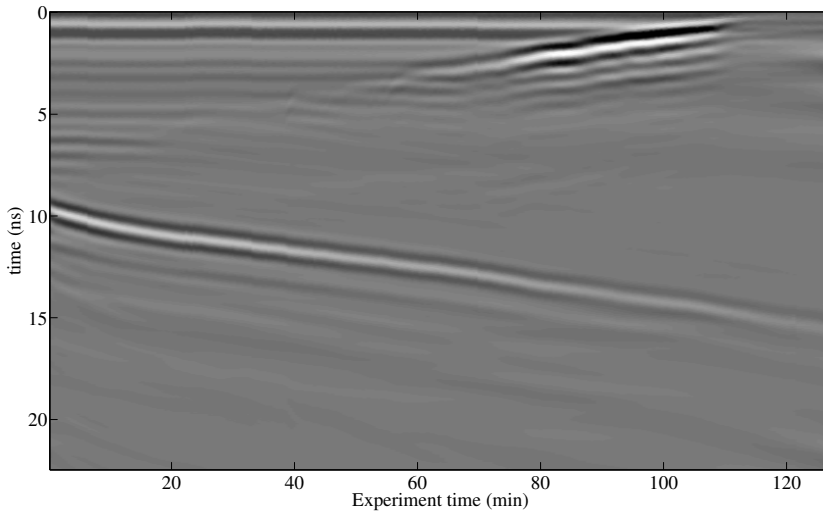


Figure 4.8: Radar section of all the oil displacement experiment in inhomogeneous residual water conditions.

Several experiments were performed under residual water saturation conditions and the GPR results showed a similar behavior. To re-establish the initial conditions for the residual water saturation, it was necessary to drain the system using the suction pump. Figure 4.9 shows the initial traces of different water flooding experiments under residual water saturation conditions. Although the traces do not overlap, there is a good correlation which implies that almost the same saturation conditions were re-established.

Experiments at constant pressure under oil saturated conditions

Figure 4.10 shows the radar section acquired during the water injection at constant pressure under oil saturated conditions. The GPR traces were acquired every 10 s during the injection, which was performed in steps corresponding each to an increase of 6 l of injected water. At each of these steps impedance measurements were acquired and the fluid outflow was measured. The numbered vertical lines visible in the radar section correspond to the respective impedance profiles depicted in figure 4.7. For every vertical line the cumulative step outflow is also reported. The outflow was stored in separate 20 l tanks. The evolution of the composition of the outflow is tracked this way and is reported in table 4.2.

Strong reflections occur in conjunction with the sharp impedance decrease. At later stages of the experiment time the radar response shows a

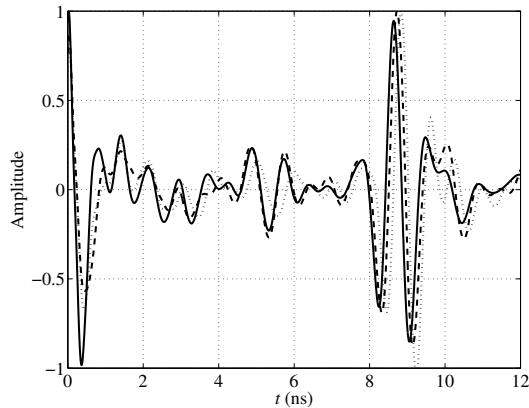


Figure 4.9: Normalized A scan of the initial residual saturation condition of consecutive water flooding experiments.

Table 4.2: Fluid outflow composition of the water flooding experiment at constant pressure in oil saturated condition. The outflow values are expressed in l.

tank outflow	22	22	20	20	20	tot	%
oil	22	22	17	6	3	70	67
water	-	-	3	14	17	34	33

stationary behavior, where just a continuous slight delay of the metal reflections is observed. The initial impedance profile in figure 4.7 indicates that in the deeper 20 cm, there is a higher water saturation compared to the upper 30 cm. In the initial stages of the experiment water slightly increases its volume in the pores and there is not enough contrast to generate EM reflections, as it was observed in the one-phase flow experiment. As water reaches the upper part of the oil saturated sand, observable radar reflections appear and the water front can be clearly monitored; later, it reaches the top, where it starts to spill out, and the radar response becomes almost constant. After the 12th impedance profile water was mainly spilling out of the sand box, as can be verified in table 4.2.

Experiments at constant injection rate under oil saturated conditions

This type of experiment was repeated three times with increasing values of the electrical conductivity of both the residual and injected water: 0.05, 0.3 and 1 S/m. Figure 4.11 shows the cumulative water injection and fluid production of the three experiments. The total fluid outflow of the three experiments

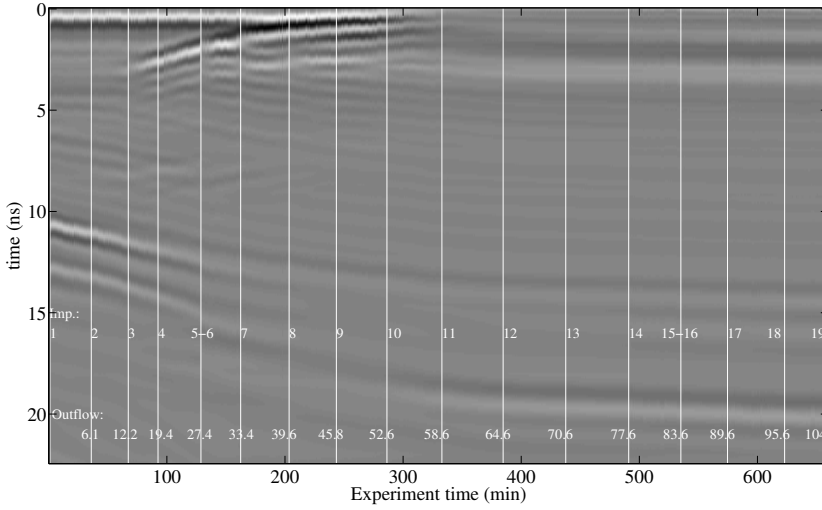


Figure 4.10: Radar section of all the oil displacement experiment performed at constant pressure. The numbered vertical lines correspond to the respective impedance profiles shown in figure 4.7b. The cumulative outflow in l is reported for every step of the injection.

resulted in few liters less than the total amount of injected water. This is due to the fact that the outflow tube was located a few centimeters below the sand surface, so part of the injected water remained in the superficial sand layer. The continuous fluid production through the outflow tube was stored in 10 l tanks, of which the composition is reported in table 4.3 for all three experiments. The different outflows show a similar trend: the first 50 l were composed mainly of oil while the later outflow was composed mainly of water.

Figure 4.12 shows the radar sections acquired during the experiments

Table 4.3: Composition of the outflow fluid during the water flooding experiments at constant injection rate. The outflow values are expressed in l.

		tank number									tot	%
		1	2	3	4	5	6	7	8	9		
Exp.1	oil	10	10	10	10	10	2	1	1	1.5	55.5	66.1
	wat	-	-	-	-	-	8	9	9	2.5	28.5	33.9
Exp.2	oil	10	10	10	10	9	1	0.8	0.4	2	52.2	62.7
	wat	-	-	-	-	1	9	9.2	9.6	2.2	31	37.3
Exp.3	oil	10	10	10	10	8.8	0.8	0.6	0.4	1.2	51.8	62.3
	wat	-	-	-	-	1.2	9.2	9.4	9.6	2	31.4	37.7

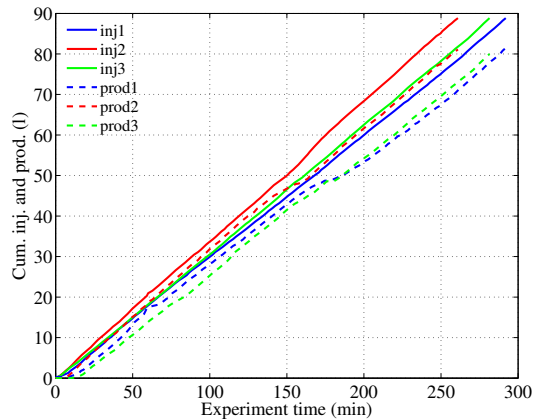


Figure 4.11: Cumulative injection (continuous lines) and production (dashed lines) of the three experiments performed at constant injection rate.

performed with the water at, respectively, 0.05 (a), 0.3 (b) and 1 (c) S/m. The vertical lines correspond to the times at which the 10 l outflow tanks were filled; the lines are numbered according to the respective tank number as reported in table 4.3. Figures 4.12a shows features similar to the ones that can be seen in figure 4.8. The water front is characterized by an up-dipping event in the upper part of the sand, while in the deeper layers it does not appear as a clear event; however, continuous down-dipping events are visible in the section. As in the flooding experiments under residual saturation conditions, the lower portion of the sand presented a higher water content and the water injection did not result in a clear reflection. The metal sheet, instead, appeared as a clear down-dipping event for the duration of the experiment.

All the reflection events of the three sections present a similar trend in agreement with the outflow composition behavior observed in table 4.3. The first part of the sections corresponding to outflows composed mainly by oil is characterized by down and up dipping reflection events, whereas stable reflection events characterize the second part of the sections when water is the main fluid spilling out from the sand box.

Although the same reflections can be recognized in the three experiments, the events visible in figure 4.12c (experiment with $\sigma_w=1$ S/m) are less pronounced or not visible; for example, the metal reflection in figure 4.12c is visible up to an experiment time of 50 minutes.

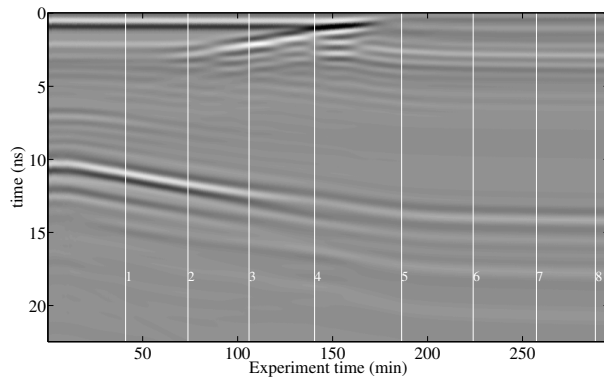
Figure 4.13 shows a comparison of the initial traces normalized by the maximum of the direct arrival for the three experiments. The traces present

a good correlation, which means that the initial conditions were quite similar. The main difference is given by the amplitudes of the events due to the effect of the conductivity. For the experiment at $\sigma_w = 1$ S/m, the metal reflection amplitude (at about 10 ns for all the experiments) is 40 % less than the direct arrival amplitude, whereas for the less saline experiments the metal reflections remain almost invariant.

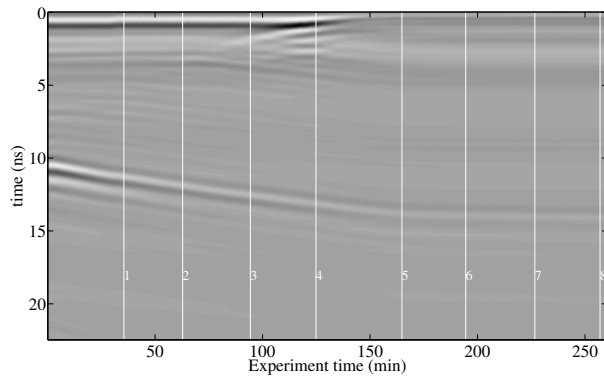
The conductivity effect can be better appreciated analyzing the variation of the instantaneous amplitude, i.e. an attribute of the complex trace (Barnes, 2007), during the three experiments (figure 4.14). The instantaneous amplitude is calculated for the different dataset and normalized by the respective maximum values. This attribute representation allows to get a quantitative estimation of the signal attenuation for the specific GPR system used. The amplitude of the metal reflection remain almost constant during all the water injection (figure 4.14a), whereas it presents a clear attenuation during the saline waterflooding (figures 4.14b and 4.14c). In the extreme case of $\sigma = 1$ S/m, the metal reflection is visible up to an experiment time of 130 minutes and 13 ns in the GPR time, approximately the time at which water reaches the top of the sandbox and start to spill out. At water breakthrough time the amplitude undergoes an attenuation of about 12, 22 and 37 dB, respectively, for the experiments performed with $\sigma_w = 0.05, 0.3$ and 1 S/m.

The water front results in down or up-dipping events, forming wedge-shaped features. In both types of flooding experiments, these features are visible in the radar section. A delay of a reflection indicates that water has gone beyond that event; as soon as water goes into a medium that present sufficient contrast that generates a measurable reflection, an up-dipping event appears over a down-dipping one. The monitoring of these features can be enhanced by analyzing the instantaneous frequency of the complex trace, i.e. the time derivative of the instantaneous phase (Taner *et al.*, 1979; Barnes, 2007). The instantaneous frequency is a useful tool to enhance the visualization of wedge-shaped reflections, as it is used in seismic interpretation to display similar features such as pinch-outs or angular unconformities.

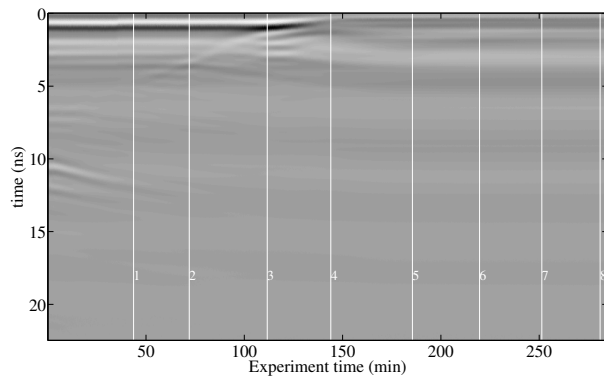
Figures 4.15a and 4.15b show the instantaneous frequency of the radar section acquired during the water injection experiment under residual water saturation conditions, represented in figure 4.8, and under oil saturated conditions, represented in figure 4.12a. The wedge-shaped reflections, not visible on the radar section, are clearly discernible. This can be explained by the fact that the instantaneous frequency is independent of the reflection strength and makes weaker events clearer.



(a)



(b)



(c)

Figure 4.12: Radar section of the displacement experiments performed at constant injection rate. The electrical conductivity of the injected water was $\sigma = 0.05$ S/m (a), $\sigma = 0.3$ S/m (b) and $\sigma = 1$ S/m (c).

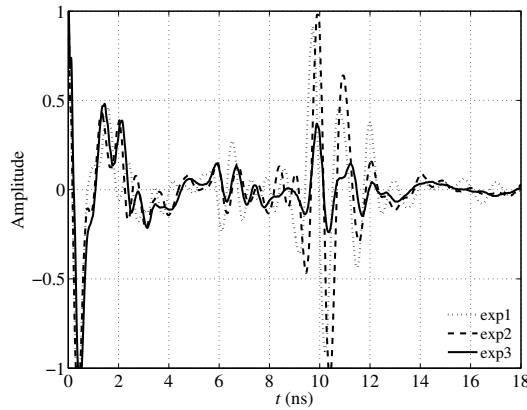
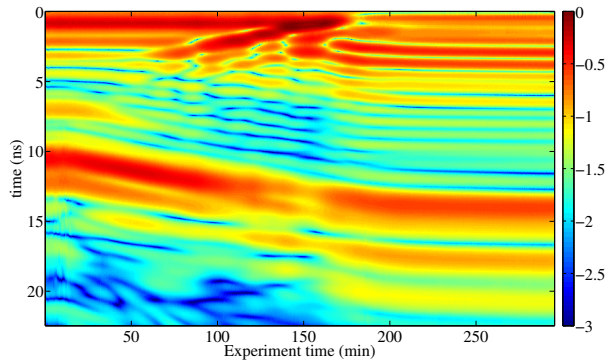


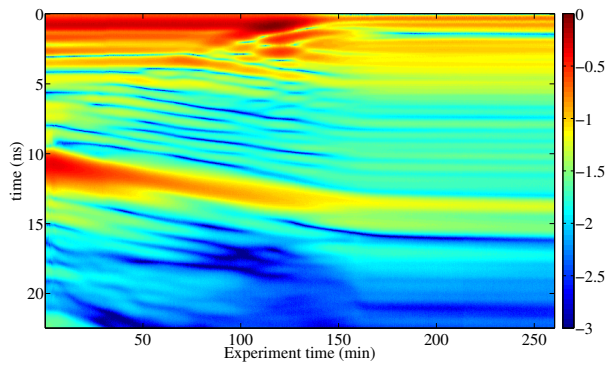
Figure 4.13: Normalized A scan of the initial residual saturation condition of water flooding experiment performed at constant injection rate. The electrical conductivity of the residual water was 0.05, 0.3 and 1 S/m, respectively, for exp1, exp2 and exp3.

4.4 Conclusions

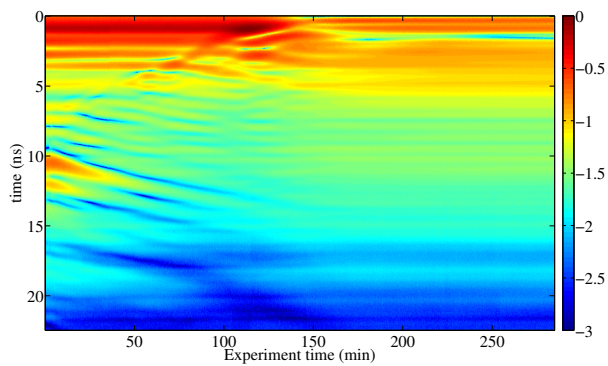
The experimental results presented in this study provide good insights of the potential for GPR to monitor oil displacement by waterflooding in near-well environments. Both the waterflooding experiments conducted under residual water saturation conditions and under oil saturated conditions showed similar characteristics. The water front appears as down or up-dipping reflection events, forming wedge-shaped features, depending on the initial water saturation and porosity distribution. Interpretation of the monitoring data containing the flow reflection features is facilitated by attribute transformation. Instantaneous frequency proved to be a powerful tool to enhance wedge-shaped events. The main limiting factor of GPR monitoring seems to be the electrical conductivity of the residual water. The experiments at high salinity water injection showed a strong attenuation of the signal and a severe reduction of the resolution. Instantaneous amplitude was used to quantify the signal attenuation as a function of the water conductivity for the waterflooding experiments under oil saturated condition. The metal reflection at the water breakthrough time, when water started spilling out of the sand box, for the most saline experiment ($\sigma_w = 1$ S/m) resulted to be 35 dB higher than the experiment performed with a water conductivity of 0.05 S/m. Impedance measurements were used to support the interpretation of the GPR data and the two types of data agreed in describing the flow process, although it is not necessary to measure the resistivity profile.



(a)

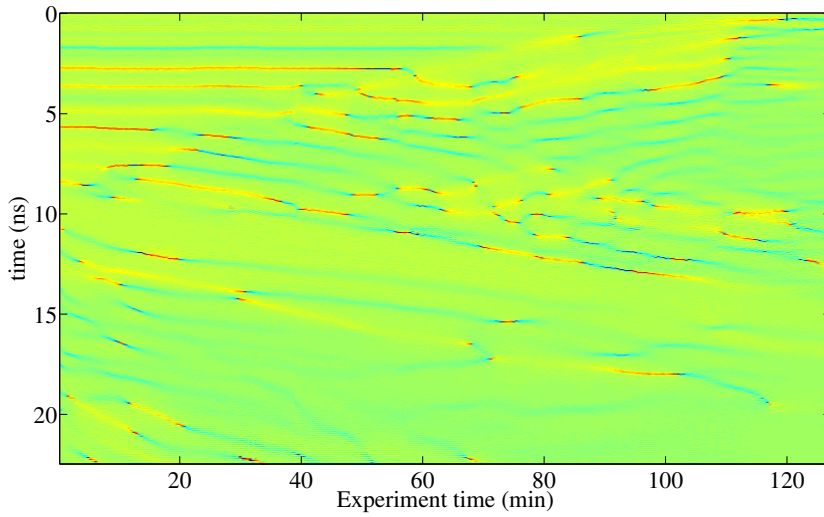


(b)

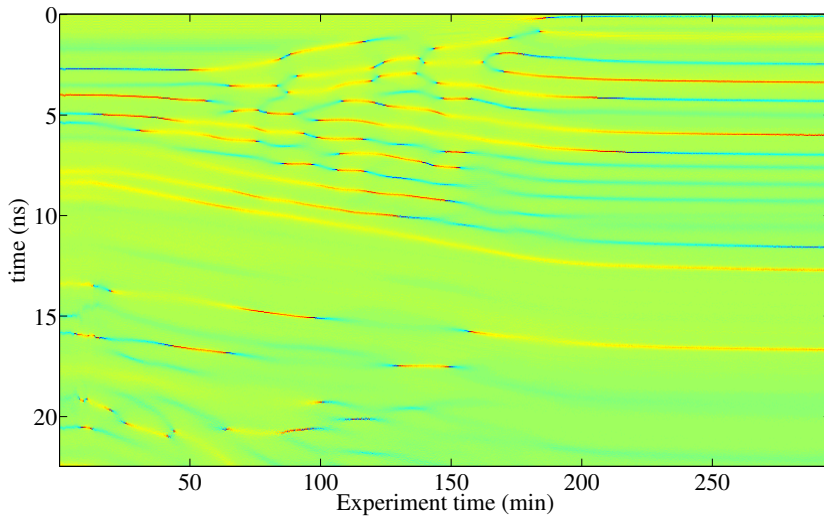


(c)

Figure 4.14: Normalized instantaneous amplitude of the experiments performed at constant injection rate expressed in log scale. The electrical conductivity of the injected water was $\sigma = 0.05$ S/m (a), $\sigma = 0.3$ S/m (b) and $\sigma = 1$ S/m (c).



(a)



(b)

Figure 4.15: Instantaneous frequency of the water flooding experiment performed under residual water saturation condition (a) and under oil saturated condition with $\sigma_w = 0.05$ S/m (b).

Chapter 5

Uncertainty in GPR

5.1 Introduction

Over the last decades ground penetrating radar (GPR) has received increasing attention in environmental research and engineering applications. This is due to the sensitivity of electromagnetic (EM) waves to electric changes in the subsurface, which can be detected, imaged and characterized. The high resolution with which it is possible to image and characterize the subsurface made GPR techniques very suitable for hydro-geophysical problems, such as identifying soil stratigraphy (Davies & Annan, 1989), measuring soil water content (Huisman *et al.*, 2003; Galagedara *et al.*, 2005), following water front movement (Vellidis *et al.*, 1990; Tsoflias *et al.*, 2001; Talley *et al.*, 2005; Deiana *et al.*, 2008), as well as for engineering applications, such as pavement and railroad monitoring (Liu *et al.*, 2008; Olhoeft *et al.*, 2004), and fracture mapping in historical buildings (Grandjean & Gourry, 1996; Leucci *et al.*, 2007).

Quantitative characterization of the EM properties of the subsurface is one of the most challenging issues in GPR applications. With the increased computer power, the recent trend is inverting the GPR scattering data for the desired subsurface using tomographic (Bradford *et al.*, 2009; Cordua *et al.*, 2009; Crocco *et al.*, 2010) and full-waveform inversion methods (Gloaguen *et al.*, 2007; Minet *et al.*, 2010; Moghadas *et al.*, 2010; Meles *et al.*, 2010). These techniques rely on forward EM modeling, therefore, it is essential to know how well the model can reproduce the physics of the problem and what is the degree of uncertainties in the model. Model errors propagate in all the processing steps of the inversion and can result in significant errors in the estimation of the subsurface parameters. Another source of errors is related to the acquisition of the GPR data. In some models, operational calibration

measurements are carried out to account for antenna effects (Chanzy *et al.*, 1996; Lambot *et al.*, 2004; Oden *et al.*, 2008). Applying these calibration procedures it is possible to filter the measured data and obtain a new set of data which can be directly modeled as the impulse response (Green's function) of the subsurface. Again it is crucial to evaluate the uncertainties involved in these calibrations.

We took in consideration an off-ground monostatic ultrawideband (UWB) stepped-frequency continuous-wave (SFCW) radar system for which forward and inverse model formulations exist (Lambot *et al.*, 2004). The forward model is based on linear system transfer functions and on the exact solution of the 3D Maxwell's equations for wave propagation in a multi-layered medium representing the subsurface. Full-waveform inversion is carried out iteratively using global in combination with local optimization. The inversion procedure was demonstrated to be successful in several applications, such as determining the soil water content profile (Lambot *et al.*, 2004, 2008a), and monitoring dynamic water flow processes both in laboratory and field environments (Lambot *et al.*, 2009; Jadoon *et al.*, 2008). A preliminary study addressing the uncertainties in the EM forward model and in the calibration procedure has been carried out in (Patriarca *et al.*, 2010). In this paper we discuss a statistical analysis of a large number of calibration measurements and we analyze the effect of the transfer function accuracy on measured and computed Green's functions. Moreover, we investigate the uncertainties on real measurement inversion results.

5.2 Material and Methods

5.2.1 EM Forward and Inverse Modeling

For a far-field antenna connected to a vector network analyzer, a well established radar antenna model (Lambot *et al.*, 2004) is expressed as:

$$S_{11}(f) = \frac{Y(f)}{X(f)} = H_i(f) + \frac{H(f)G_{xx}^\uparrow(f)}{1 - H_f G_{xx}^\uparrow(f)}, \quad (5.1)$$

where $S_{11}(f)$ is the ratio between the reflected $Y(f)$ and incident $X(f)$ signal; $H_i(f)$, $H(f)$ and $H_f(f)$ account, respectively, for the antenna return loss, the antenna transmitting-receiving transfer function and the antenna feedback loss; $G_{xx}^\uparrow(f)$ is the Green's function, which accounts for the back-scattered (denoted by the upward arrow) x -directed electric field component (first subscript x) at the antenna phase center for an x -directed electric source (second subscript x) situated at the same position. The air-subsurface system

is modeled as a 3D multi-layered medium in which every layer is characterized by constant electric properties. The solution of Maxwell's equations for electromagnetic waves propagating in a multi-layered medium is well known (Chew, 1995; Michalski & Mosig, 1997; Slob & Fokkema, 2002). Following the approach developed in Slob & Fokkema (2002), the Green's function is derived using a recursive formula to compute the transverse electric and magnetic global reflection coefficients in the spectral domain. The transformation to the spatial domain is performed by evaluating numerically a semi-infinite complex integral (Lambot *et al.*, 2007).

The characterization of the subsurface parameters is performed through full-waveform inversion of the Green's function. An objective function is minimized in the least square sense:

$$\phi(\mathbf{b}) = \left[\frac{\sum_{f_{min}}^{f_{max}} |\mathbf{G}_{\mathbf{xx}}^{\uparrow*} - \mathbf{G}_{\mathbf{xx}}^{\uparrow}|^2}{\sum_{f_{min}}^{f_{max}} |\mathbf{G}_{\mathbf{xx}}^{\uparrow*}|^2} \right]^{1/2}, \quad (5.2)$$

where $\mathbf{G}_{\mathbf{xx}}^{\uparrow*} = G_{xx}^{\uparrow*}(f)$ and $\mathbf{G}_{\mathbf{xx}}^{\uparrow} = G_{xx}^{\uparrow}(f, b)$ are vectors containing, respectively, the retrieved and the modeled air-subsurface reflection response, \mathbf{b} is the parameter vector to be estimated, and f_{min} and f_{max} stand, respectively, for the minimum and maximum frequency used. The objective function is minimized by means of the global multilevel coordinate search algorithm (Huyer & Neumaier, 1999) sequentially combined with the Neelder-Mead simplex algorithm (Lagarias *et al.*, 1998).

5.2.2 GPR equipment

The radar system was set up using a vector network analyzer (VNA) combined with an off-ground monostatic horn antenna. We used two types of VNA (ZVT8 and FSH8, Rhode&Schwarz, Germany) and two types of linear polarized double ridged broadband TEM horn antenna (BBHA 9120 A and C, Schwarzbeck Mess-Elektronik). The BBHA 9120 A has an axial length of 0.22 m and the aperture area is $0.14 \times 0.24 \text{ m}^2$; its nominal range of frequency is 0.8-5 GHz and its isotropic gain ranges from 6 to 15 dBi. The BBHA 9120 C has an axial length of 0.136 m and the aperture is $0.066 \times 0.091 \text{ m}^2$; its nominal frequency range is 3-18 GHz and its isotropic gain ranges from 5 to 16 dBi. The antennas were connected to the reflection port of the VNA via an N-type 50Ω coaxial cable. The VNA was calibrated at the connection between the antenna feed point and the cable using a 50Ω OSM (Open, Short, Match) series of the high precision standard calibration kit. This establishes a reference calibration plane at which $S_{11}(f)$ is measured. For the

antenna BBHA 9120 A, S_{11} was sampled at 631 evenly distributed operating frequencies over the range 0.8 - 2.8 GHz; for the antenna BBHA 9120 C, the signal was measured over 3-8 GHz at 2501 operating frequencies, using 2 MHz frequency step.

5.2.3 Antenna transfer function determination

The characteristic antenna transfer functions H_i , H and H_f can be determined by solving a system of equation (5.1) for at least three different model configurations. This is achieved by performing calibration measurements over a known reflector, such as a perfect electric conductor, for which the Green's functions $G_{xx,k}^\uparrow(f)$ can be computed (k denotes the model configurations ranging from 1 to n), while $S_{11,k}(f)$ is readily measured. The characterization of the antenna transfer functions improves when the system is overdetermined, i.e., with an increasing number of model configurations m (Lambot *et al.*, 2006). This is because for some frequencies the solution of the system may not be numerically stable. The system of equations is rewritten as:

$$S_{11,k} = H_i + S_{11,k}G_{xx,k}^\uparrow H_f + G_{xx,k}^\uparrow(H - H_i H_f). \quad (5.3)$$

Equation (5.3) can be expressed in matrix form as (Lambot *et al.*, 2006; Jadoon *et al.*, 2011):

$$\mathbf{b} = \mathbf{A}\mathbf{x}, \quad (5.4)$$

where

$$\mathbf{b} = (S_{11,1}, \dots, S_{11,k} \dots, S_{11,n})^T, \quad (5.5)$$

$$\mathbf{A} = \begin{bmatrix} 1 & S_{11,1}G_{xx,1}^\uparrow & G_{xx,1}^\uparrow \\ \vdots & \vdots & \vdots \\ 1 & S_{11,k}G_{xx,k}^\uparrow & G_{xx,k}^\uparrow \\ \vdots & \vdots & \vdots \\ 1 & S_{11,n}G_{xx,n}^\uparrow & G_{xx,n}^\uparrow \end{bmatrix}, \quad (5.6)$$

$$\mathbf{x} = (H_i, \dots, H_f \dots, H - H_i H_f)^T, \quad (5.7)$$

and T stands for matrix transposition. The vector of unknowns is computed in the least-square sense as:

$$\mathbf{x} = (\mathbf{A}^H \mathbf{A})^{-1} \mathbf{A}^H \mathbf{b}, \quad (5.8)$$

where the symbol H denotes the Hermitian, or the complex conjugate transpose.

Table 5.1: Heights of the calibration measurements for the two antenna

antenna	heights (mm)							
0.8-2.8 GHz	244	254	264	274	294	314	334	351
3-8 GHz	205	215	225	235	245	255	265	275

5.2.4 Uncertainties in the calibration method

The calibration of the off-ground GPR system is performed measuring the scattering functions $S_{11}(f)$ over a metal sheet for different antenna heights. This procedure introduces uncertainties that result in variations in the transfer functions. The origin of the uncertainties is twofold: gross errors, which can be controlled by proper measurement setup/protocol, e.g., presence of scattering objects, and random errors, which cannot be controlled, such as, e.g., VNA noise. We acquired calibration measurements with both the VNAs described in the GPR equipment section, in environments where the setup/protocol was satisfied and in noisy environments characterized by the presence of dielectric and metallic scattering objects. The calibration measurements were performed over different sizes of square metal sheets (9 m², 2.25 m² and 0.64 m²). The objective was to carry out a statistical analysis of the antenna transfer functions and to evaluate how they are affected by noisy environments.

We present a specific analysis that was performed using both the BBHA 9120 A and C antennas over the same 9 m² metal plate and connected to the same VNA, ZVT8. In this case the calibration was performed in an ideal environment without scattering objects in a range of 3 m from the antennas. For both the antennas 8 calibration measurements were acquired; table 5.1 shows the heights of the measurements.

The transfer functions were determined using 5 scattering functions $S_{11}(f)$ out of the 8 measured $S_{11}(f)$ and all the possible combinations were considered, so that it was possible to invert for 56 distinct sets of $H_i(f)$, $H(f)$ and $H_f(f)$ and quantify the uncertainties in the retrieved transfer functions. The number of possible combinations is given by

$$\binom{n}{k} = \frac{n!}{k!(n-k)!}, \quad (5.9)$$

where n indicates the total number of calibration measurements and k corresponds to the actual number of measurements used for the transfer function determination, in our case $n = 8$ and $k = 5$.

An important aspect of the calibration is the determination of the antenna heights with respect to the metal plate. These are usually measured manually, however, accurate measurements are difficult to achieve, especially over soft and irregular surface. Inaccurate heights result in systematic errors that affect all the following processing steps. The height steps Δh can be calculated via the time difference between following metal reflections as:

$$\Delta h = \frac{S_{11,n+1}(t) - S_{11,n}(t)}{2} c_0, \quad (5.10)$$

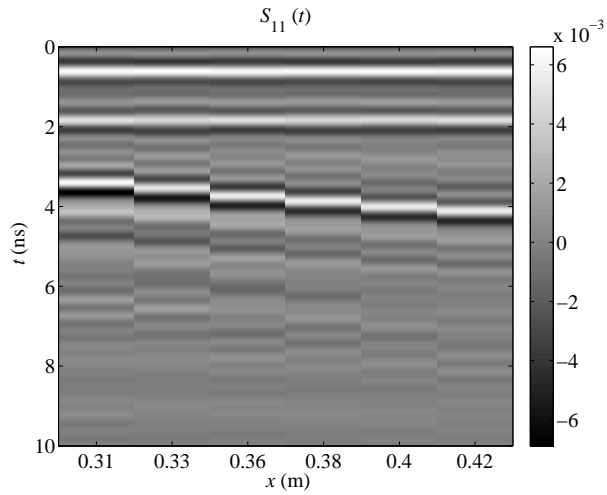
where $S_{11}(t)$ is the time domain signal, the subscript n indicates the antenna height and c_0 is the speed of light. In this way it is necessary to measure just one height manually, while the rest of the heights are calculated through equation (5.10). This is an approximate method that is valid when the antenna is in the far-field and the metal reflections are clearly discernible.

Fig. 5.1 shows the time domain representation of $S_{11}(f)$ for both the frequency ranges. The first events between 0-2 ns correspond to the reflections within the antenna, i.e., the return loss. The metal plate reflections arrive at later times as the antenna height increases: between 3-5 ns for the 0.8-2.8 GHz antenna and between 2.5-3.5 ns for the 3-8 GHz antenna. Multiple reflections, due to the feedback loss of the antenna, are observable at later times, respectively, between 6-9 ns and 5-6 ns for the low and high frequency antennas.

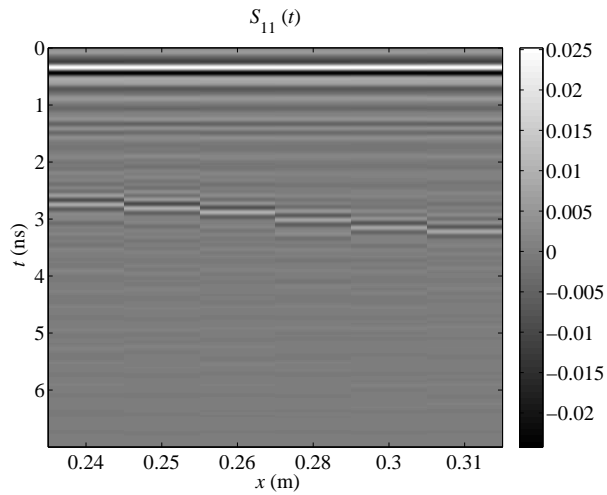
5.2.5 Measured and computed Green's functions

A comparison between measured and modeled Green's functions discussed in the previous session was performed. The objective was to quantify and analyze the relative error present in the measurements in relation to the transfer function uncertainties. We used the calibration measurements analyzed in the previous session, where a number of transfer function sets were determined using different combinations of k scattering functions $S_{11}(f)$ out of n $S_{11}(f)$. The scattering functions $S_{11,k}(f)$ (k denotes the different antenna heights ranging from 1 to n) were filtered into $G_{xx}^{\uparrow*}(f)$ through Equation (5.3). This operation was performed using the sets of transfer functions determined without including the respective $S_{11}(f)$ height ($n - k$). In this way, it was possible to retrieve $\binom{n}{k} \times (n - k) = 168$ Green's functions $G_{xx}^{\uparrow*}(f)$ ($n = 8$ and $k = 5$) and calculate the relative error, with respect to the modeled $G_{xx}^{\uparrow}(f)$ as the following:

$$\delta_1 = \left| \frac{|G_{xx}^{\uparrow*}(f)| - |G_{xx}^{\uparrow}(f)|}{|G_{xx}^{\uparrow}(f)|} \right|. \quad (5.11)$$



(a)



(b)

Figure 5.1: Time domain representation of the scattering functions $S_{11}(f)$ measured at different heights over a metal sheet with the 0.8-2.8 GHz antenna (a) and the 3-8 GHz antenna (b).

For every height we could compute one $G_{xx}^\uparrow(f)$ and retrieve $\binom{n}{k} \times (n-k)/n = 21$ measured $G_{xx}^{\uparrow*}(f)$. The relative error δ_1 include all the different heights.

To better understand the propagation of the transfer function uncertainties in the measured $G_{xx}^{\uparrow*}(f)$, a computed Green's function $G_{xx_{mod}}^\uparrow(f)$ was back-transformed into scattering functions $S_{11}(f)$ through n transfer function sets. These scattering functions were then filtered with $n-1$ transfer function sets, excluding the one used to initially obtain $S_{11}(f)$. All the 56 transfer function sets were used to generate $n \times (n-1) = 3080$ Green's functions $G_{xx_{gen}}^{\uparrow*}(f)$, $n = 56$, and calculate the relative error with respect to the original $G_{xx}^\uparrow(f)$. In this case the Green's functions are not directly measured but generated by filtering a computed $G_{xx}^\uparrow(f)$ with the measured sets of transfer functions. This relative error contains just the transfer function uncertainties and is expressed as following:

$$\delta_2 = \left| \frac{|G_{xx_{gen}}^{\uparrow*}(f)| - |G_{xx_{mod}}^\uparrow(f)|}{|G_{xx_{mod}}^\uparrow(f)|} \right|. \quad (5.12)$$

As a term of comparison between the two types of relative errors, the following coefficient of correlation was used:

$$\rho = \frac{\sum_{f_{min}}^{f_{max}} (\delta_1 - \bar{\delta}_1)(\delta_2 - \bar{\delta}_2)}{\sqrt{\sum_{f_{min}}^{f_{max}} (\delta_1 - \bar{\delta}_1)^2 \sum_{f_{min}}^{f_{max}} (\delta_2 - \bar{\delta}_2)^2}}. \quad (5.13)$$

Higher values of ρ indicate that the error of the filtered $G_{xx}^{\uparrow*}(f)$ is mainly due to the transfer function uncertainties.

The same analysis was performed for both antennas in their respective frequency ranges. The computed Green's functions $G_{xx_{mod}}^\uparrow(f)$ model the calibration measurements as if they were taken over an infinite perfect electric conductor. The source height was placed at 0.35 m for the 0.8-2.8 GHz range and at 0.25 for the 3-8 GHz range.

In addition, we considered computed Green's function, which modeled the laboratory experiments described in the next session, and calibration measurements acquired in noisy environment. The computed $G_{xx_{mod}}^\uparrow(f)$ modeled the real measurement taken with the 0.8-2.8 GHz antenna (Fig. 5.2a): the source is placed over a sand layer located above a metal sheet. The source height, h_0 , is set to 0.17 m, the sand layer is 0.235 m and the relative permittivity and conductivity of the sand is set respectively to 3 and 0 S/m. We used 14 sets of transfer functions so we could generate $14 \times 13 = 182$ $G_{xx_{gen}}^{\uparrow*}(f)$. The aim was to investigate if averaging sets of generated Green's function allows to retrieve the original one.

5.2.6 Inversion experiments

The objective of the inversion experiments was to investigate the effects of the antenna transfer function uncertainties on the retrieval of the medium parameters through inversion. The inversions were performed using different transfer function sets; every set consisted of 56 transfer functions and allowed for the same number of inversions. A statistical analysis of the inverted parameters has then been carried out. The real data consisted of measurements over a dry sand layer and a plaster layer, respectively, with the 0.8-2.8 GHz antenna and the 3-8 GHz antenna. In both cases the investigated media were located above a metal sheet and three inverted parameters were retrieved: the medium electric permittivity, the antenna height and the layer thickness. Fig. 5.2 represents a sketch of the two experimental scenarios.

The 0.8-2.8 GHz antenna was placed 0.175 ± 0.005 m over 0.235 ± 0.005 m of sand, which was located in a meter-scale cylindrical box; the experimental set up is described in chapter 4. $S_{11}(f)$ was acquired with the FSH8 and the inversions were performed using two transfer function sets. The first one was determined from calibration measurements acquired inside the experimental setup where a 0.8 m^2 metal plate was placed below the sand box and the antenna was surrounded by the sand box wall at about 0.6 m distance. The second type was determined from measurements acquired over a 1.5 m^2 metal sheet with no objects in the antenna proximity, a less noisy environment. The 3-8 GHz antenna was placed 0.187 ± 0.001 m and the plaster thickness was 0.04 ± 0.001 m, as described in Patriarca *et al.* (2011). The antenna was connected to the ZVT8 VNA and the transfer functions were determined from measurements over 9 m^2 metal plate with no scattering object surrounding the antenna. Both the plaster and the calibration measurements were acquired in the same location.

5.3 Results and Discussion

5.3.1 Uncertainties in the calibration method

Fig. 5.3 shows the 56 sets of $H_i(f)$, $H(f)$ and $H_f(f)$ determined with the ZVT8 for both antennas, the red line displays the mean. Despite the different frequency responses, both the frequency ranges present common characteristics. The return losses $H_i(f)$, depicted in Fig. 5.3(a) and 5.3(b), are characterized by a small standard variation; this is an important observation because variations in $H_i(f)$ would strongly affect the filtered $G_{xx}^\uparrow(f)$. Moreover, both $H_i(f)$ functions are above 0.5 in the lower frequency range, which means that more than half of the signal is reflected back to the VNA,

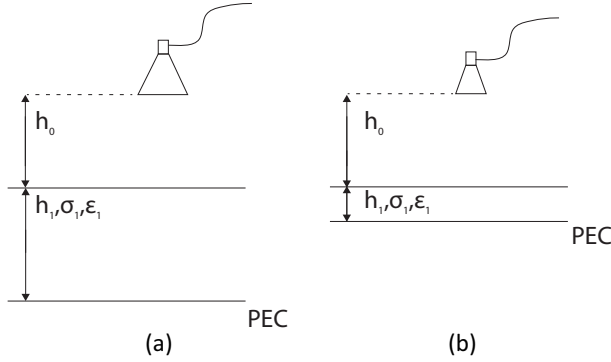


Figure 5.2: Representation of the experimental scenarios used for the inversion experiments of the 0.8-2.8 GHz range (a) and 3-8 GHz range (b).

Table 5.2: Coefficient variation of transfer function sets

H ant.	0.8-2.8 GHz	3-8 GHz
H_i	0.031	0.018
H	0.025	0.024
H_f	0.147	0.351

therefore, the antenna performance improves at higher frequencies. $H(f)$ presents a linear behavior with a constant standard deviation for the whole frequency range, as shown in Figs. 5.3(c) and 5.3(d). The more complex forms of $H_f(f)$, Fig. 5.3(e) and 5.3(f), are caused by the geometry of the antenna whose different parts constitutes multiple reflections. This explains why H_f presents the largest variation. Table 5.2 presents the coefficient of variation averaged over frequency of the two antenna transfer function (H ant.) sets. The coefficients of variation of H_i and H are in the same order while the one of H_f is much larger, especially for H_f in the 3-8 GHz. The same behavior is confirmed for transfer function sets acquired in different environments. However, a higher coefficient of variation is observed in the presence of several scattering objects and for smaller size of the metal plate. Using the FSH8 VNA with the 0.8-2.8 GHz antenna in a noisy environment results in a coefficient of variation in the order of 4 % for H_i and H and 25 % for H_f . This indicates that the variance of the transfer function increases in noisier environments.

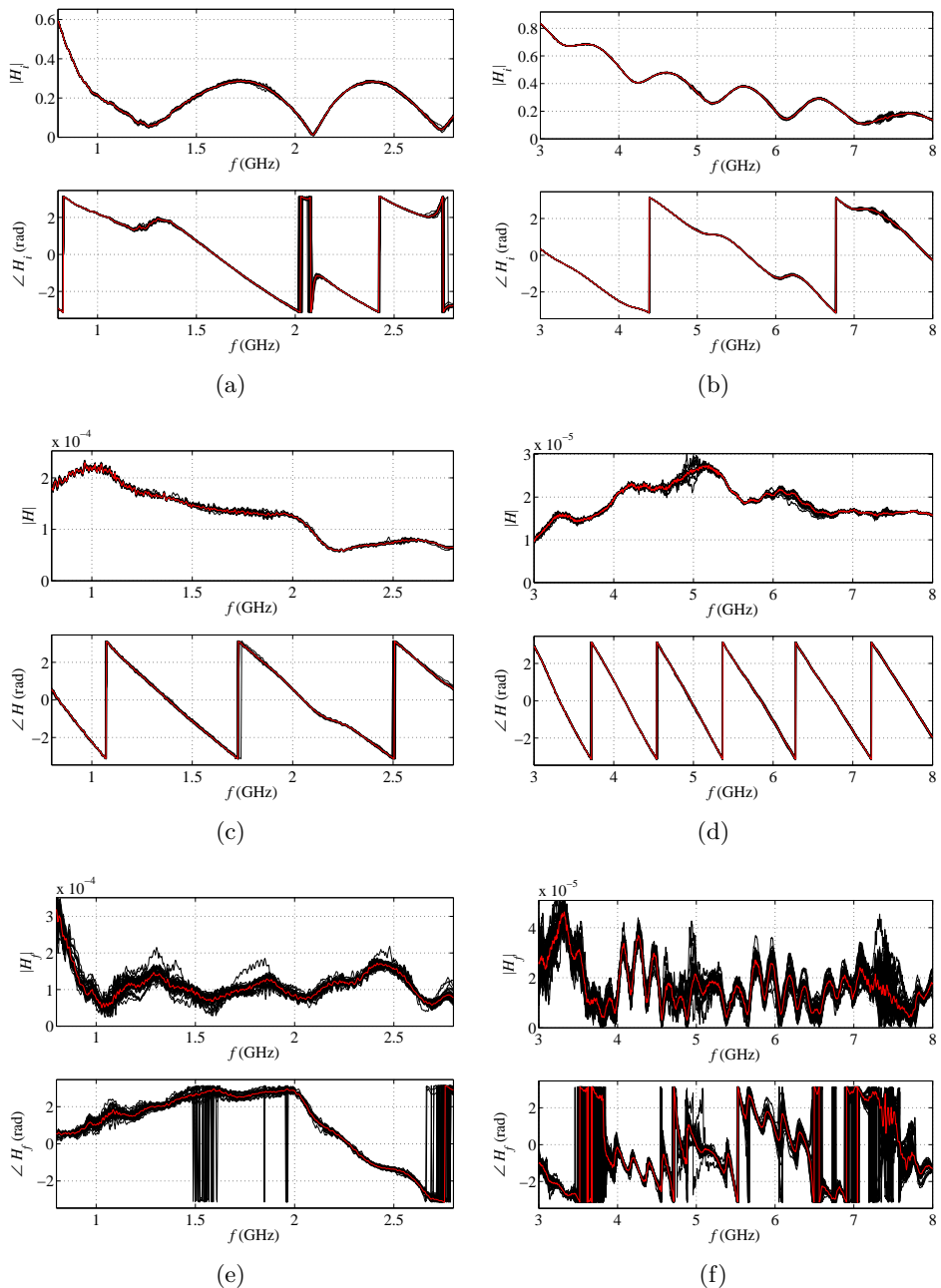


Figure 5.3: Amplitude and phase of the transfer functions for the two antennas. The return losses $H_i(f)$ are in Fig. 5.3(a) and 5.3(b), the antenna transmitting and receiving transfer functions $H(f)$ are in Fig. 5.3(c) and 5.3(d) and the feedback losses $H_f(f)$ are in Fig. 5.3(e) and 5.3(f), respectively, for the 0.8-2.8 and 3-8 GHz antenna. The black dotted lines represent all the transfer function sets and the red line is the mean.

5.3.2 Measured and computed Green's functions

Fig. 5.4(a) and 5.4(b) show the relative errors δ_1 between all the 168 retrieved $G_{xx}^{\uparrow*}(f)$ and the respective modeled $G_{xx}^{\uparrow}(f)$ for the two antennas. The mean of the relative error averaged over all frequencies for the 0.8-2.8 GHz antenna is slightly below 2 %, while for the 3-8 GHz antenna is slightly above 2 %. This is attributed to a constant systematic error generated by the antenna model, which assumes a point source over an infinitely large metal sheet with no external scattering. This condition cannot be reproduced exactly. Nevertheless, the model seems to be remarkably accurate. For some frequencies the relative error shows peaks, which can reach values of about 20%. This random behavior is not directly related to the antenna transfer function. The coefficient of variations of H_i , H and H_f over frequency are uncorrelated with the relative errors. This is explained by the non-linear relation between $G_{xx}^{\uparrow*}(f)$ and the antenna transfer functions as expressed in Equation (5.3).

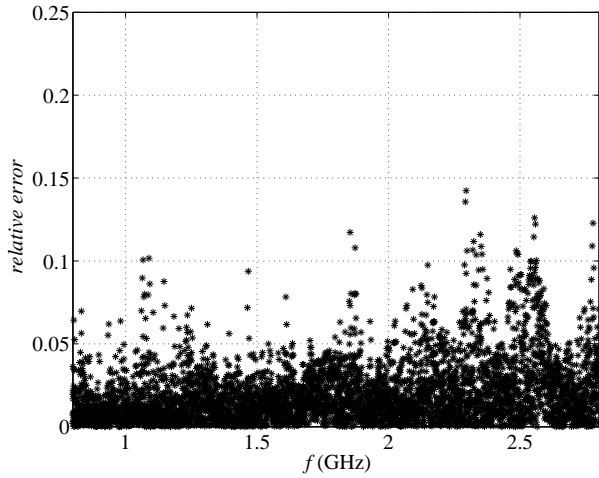
Figs. 5.5(a) and 5.5(b) show that there is a good correlation between δ_1 and δ_2 , the relative errors of, respectively, the measured and generated $G_{xx}^{\uparrow*}(f)$. The coefficient of correlation ρ is 0.88 for the 0.8-2.8 GHz range and 0.95 for the 3-8 GHz range. This proves that most of the uncertainties in the filtered $G_{xx}^{\uparrow*}(f)$ come from the transfer functions.

Averaging all the generated $G_{xx_{gen}}^{\uparrow*}(f)$ yields the computed $G_{xx_{mod}}^{\uparrow}(f)$. This averaging procedure has the potential to remove the transfer function uncertainties (Patriarca *et al.*, 2010). We tested different transfer function sets and computed Green's function, it was always possible to retrieve the original $G_{xx_{mod}}^{\uparrow}(f)$. This is an important observation due to the fact that an uncertainties reduction through averaging is not obvious in a non-linear system as the one described in equation 5.3.

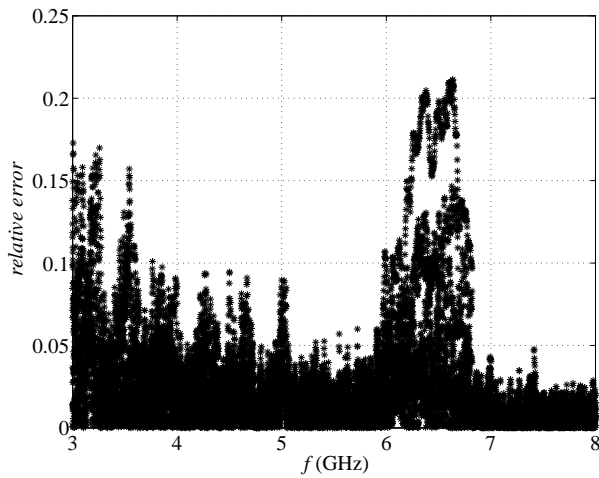
Fig. 5.6(a) shows the effect of transfer functions acquired in a laboratory environment, which present a higher coefficient of variation. Fig. 5.6 shows that the mean of all the generated $G_{xx_{gen}}^{\uparrow*}(f)$ matches almost exactly the original computed $G_{xx_{mod}}^{\uparrow}(f)$. The same behavior occurred for the 3-8 GHz frequency range.

5.3.3 Inversion results

Tables 5.3 and 5.4 show a statistics of all the inversion results for the 0.8-2.8 GHz antenna. The inversions of Table 5.3 are performed using the 56 antenna transfer functions determined in the experimental set up, while for Table 5.4 we used the 56 transfer functions determined in an environment with less scattering objects. Table 5.4 presents lower coefficients of variation

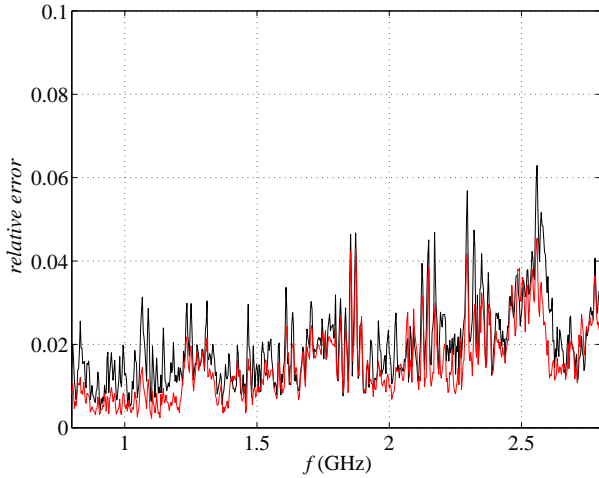


(a)

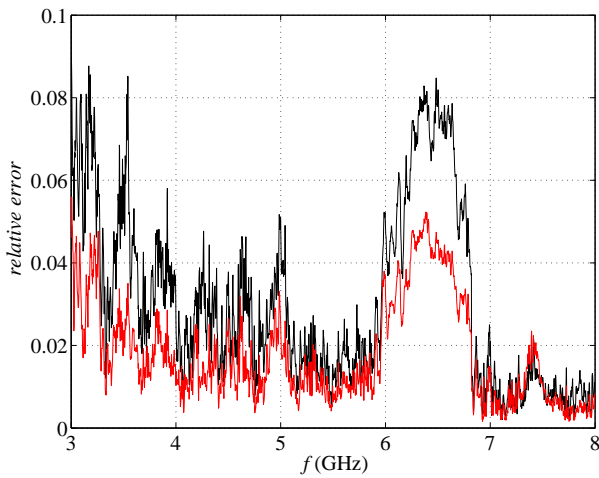


(b)

Figure 5.4: Relative error δ_1 between the model $G_{xx}^\uparrow(f)$ and retrieved $G_{xx}^{\uparrow*}(f)$ for the 0.8-2.8 GHz antenna (a) and for the 3-8 GHz antenna (b).



(a)



(b)

Figure 5.5: Comparison of the mean of δ_1 in black and the mean of δ_2 in red for the 0.8-2.8 GHz antenna (a) and for the 3-8 GHz antenna (b).

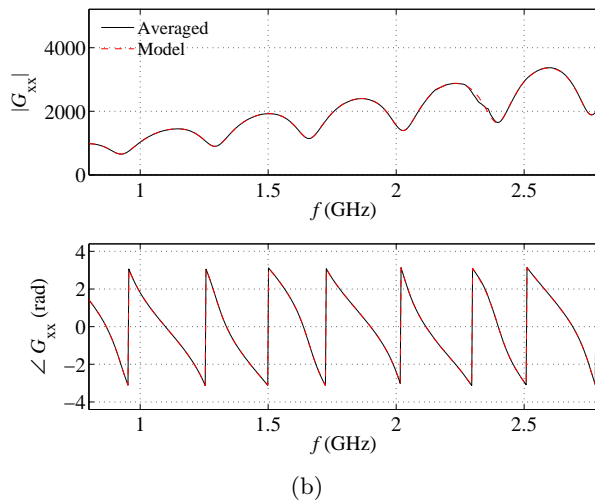
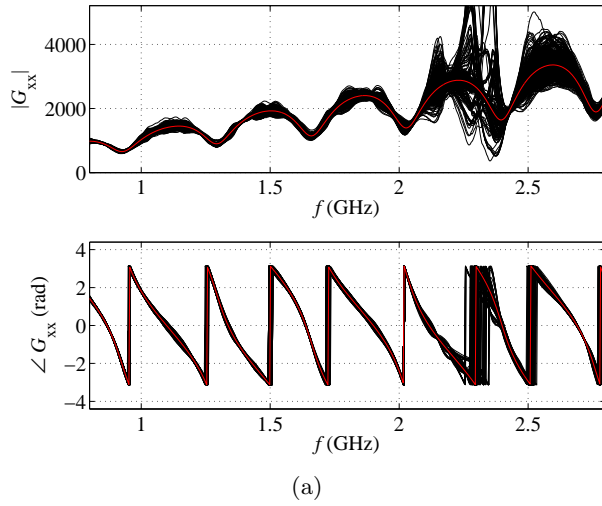


Figure 5.6: Generated Green's function (red line) and average of the Green's functions obtained using all sets of transfer functions (black lines) for the 0.8-2.8 GHz antenna.

Table 5.3: Inversion results of the 0.8-2.8 GHz antenna

Param.	mean	coef. var.	min	max	median
ε	2.9239	0.0168	2.8405	3.0893	2.9269
h_1 [m]	0.1762	0.0025	0.1752	0.01771	0.1763
h_2 [m]	0.2333	0.0553	0.2268	0.2366	0.2331
$\Phi(b)$	0.1964	0.0553	0.1573	0.2059	0.1817

mean $G_{xx}^{\uparrow*}(f)$	mean H_{ant}
2.9226	2.9240
0.1762	0.1762
0.2333	0.2332
0.1739	0.1750

of the inverted parameters and of the objective function, however, the results are less accurate. The antenna height is overestimated by 0.023 ± 0.005 m, while h_2 is inside the error of the measurement. The exact value of the sand permittivity is unknown but the overestimation of h_1 implies an underestimation of ε to fit the sand surface reflection. This indicates that the accuracy of the inversions improves with transfer functions acquired as close as possible to the measurement location and it is not related to the quality of the transfer functions.

The inversion results of the 3-8 GHz antenna are shown in Table 5.5. In this case the accuracy of the antenna height and the thickness of the plaster were submillimetric. The relative error of the inverted h_1 is below 1 % and it varies between 2 % and 6 % for h_2 .

As shown in the previous section, the transfer function uncertainties could be removed by averaging the retrieved $G_{xx}^{\uparrow*}(f)$. Therefore we performed inversions using the mean $G_{xx}^{\uparrow*}(f)$ to analyze the effect on the inverted parameters. We see that the results are close to the mean of the 56 inversion sets and the objective function is always lower. The same behavior occurs using the mean of the antenna transfer functions. This averaging procedure can therefore reduce the uncertainties of the estimated parameters obtained from full-waveform inversion.

Table 5.4: Inversion results of the 0.8-2.8 GHz antenna

Param.	mean	coef. var.	min	max	median
ε	2.7606	0.0071	2.7175	2.8154	2.7611
h_1 [m]	0.1937	0.0002	0.1936	0.1939	0.1937
h_2 [m]	0.24	0.0034	0.2378	0.2417	0.24
$\Phi(b)$	0.1621	0.0595	0.1549	0.2172	0.1587

mean $G_{xx}^{\uparrow*}(f)$	mean H_{ant}
2.7605	2.7583
0.1937	0.1937
0.24	0.2401
0.1577	0.158

Table 5.5: Inversion results of the 3-8 GHz antenna

Param.	mean	coef. var.	min	max	median
ε	2.5481	0.0185	2.4722	2.6796	2.54
h_1 [m]	0.1876	0.001	0.1873	0.1880	0.1877
h_2 [m]	0.0387	0.0101	0.0375	0.0393	0.0387
$\Phi(b)$	0.1974	0.0441	0.1822	0.2213	0.1962

mean $G_{xx}^{\uparrow*}(f)$	mean H_{ant}
2.5427	2.5507
0.1876	0.1876
0.0387	0.0387
0.1913	0.1918

5.4 Conclusion

Subsurface characterization through full-waveform inversion relies heavily on the accuracy with which the forward model represents the actual GPR-subsurface system. Model errors can propagate through the inversion procedure resulting in wrong parameter estimates. Calibration measurements are necessary to filter the antenna effects and retrieve the Green's functions that are then used in the inversion to obtain the desired subsurface parameters. We performed a large set of calibration measurements from which it was possible to better understand and evaluate the relation between the relative errors of the measured Green's function and the antenna transfer functions. The relative errors in the measured Green's function is mainly determined by the antenna transfer functions uncertainties. Averaging over a large number of transfer function sets leads to a high-accuracy Green's function estimate from the data, which leads to small errors in the estimated parameters obtained from full-waveform inversion. Although averaging sets of transfer function reduces the uncertainties, it is highly recommended to follow specific measurement protocols, including, e.g., accurate positioning of the antenna, absence of external reflectors, large size of the metal sheet and calibration of the VNA. Provided the measurement condition are respected, the inversion experiment adequately reproduce the estimated parameters. As soon as the measurement conditions are not completely respected, e.g., noisy environment characterized by the presence of scattering objects in the proximity of the antenna, inversion experiments indicated that the accuracy of the estimates improves with transfer functions acquired as close as possible to the measurement location.

Chapter 6

Conclusions

In the first chapter we have introduced the challenge the oil industry is facing of imaging the near well area in terms of fluid flow in specific production environments. Although technologies sensing the reservoir dynamic conditions are already in use, all of them poorly image the near-well region in the order of ten meters. In specific reservoir environments, e.g. thin oil rim reservoirs or heavy oil reservoirs produced with steam assisted gravity drainage, the monitoring of the near-well region is essential to mitigate premature breakthrough of unwanted fluids, such as water and gas, which can drastically affect the oil production. Such processes can be controlled through the inflow control devices and the combination of measurement and control allows for an implementation of effective control strategies. We have proposed ground penetrating radar technology as a potential tool to monitor the near well region and we formulated two approaches to investigate the GPR feasibility for oilfield applications: numerical modeling and laboratory experiments. Here the main conclusions following from the two approaches are discussed.

From the numerical simulations we conclude that a borehole radar system can be used as a monitoring tool to image the near-well region for several meters. The main constraint is the formation water electrical conductivity; high conductivity makes attenuation and phase distortion too strong for wave propagation. Water/steam front reflections are detectable in low conductivity reservoir ($\sigma < 0.02$ S/m). A system performance above 80 dB is necessary to detect reflections in the range of 10 m (chapter 2-3).

Additional reservoir constraints to be considered are a high degree of time-lapse heterogeneity changes of the EM properties and the length of the transition zone from oil to water bearing rocks. The reservoir change issue can be solved by increasing the data acquisition frequency relative to the rate of the local temporal changes or by enhancing the up-dipping events through

signal processing techniques. Note that a gradual transition zone reduces the water reflection, up to not detectable when the transition is in the order of the dominant wavelength of the EM signal (chapter 2-3).

The metal components of the wellbore casing can destructively interfere with the signal emitted by the radar sensor; however a high dielectric medium around the sensor can increase the amplitude of the reflected signal and overcome the interference problem (chapter 2).

The laboratory experiments mimic a near-borehole environment by measuring radar reflections and transmissions of moving fluid fronts in a vessel filled with sand. All the water flooding experiments presented similar characteristics. The water front appears as down or up-dipping reflection events, forming wedge-shaped features, depending on the initial water saturation and porosity distribution. The monitoring of the flow reflection features can be supported by attribute analysis, in particular, instantaneous frequency demonstrated to be a powerful tool to enhance wedge-shaped events. The analysis of the GPR data matched with impedance measurements taken simultaneously during the water flooding experiments. The most critical feature to the GPR monitoring potential appears to be the electrical conductivity of the residual water. The experiments at high salinity water injection showed a strong attenuation of the signal and a reduction of the resolution (chapter 4).

Through an analysis of measured and modeled GPR signal it is possible to take into consideration the effect of uncertainties on subsurface characterization through full-waveform inversion. Subsurface characterization through full-waveform inversion relies heavily on the accuracy with which the forward model represents the actual GPR-subsurface system. Model errors can propagate through the inversion procedure resulting in erroneous parameter estimates. The relative errors in the measured Green's function are mainly determined by the antenna transfer function uncertainties. Averaging over a large number of transfer function sets leads to a high-accuracy Green's function estimate from the data, which leads to small errors in the estimated parameters obtained from full-waveform inversion. Provided the measurement condition are respected, the inversion experiment adequately reproduces the estimated parameters. As soon as the measurement conditions are not completely respected, e.g., presence of extraneous objects, inversion experiments indicate that the accuracy of the estimates improves with transfer functions acquired as close as possible to the measurement location (chapter 5).

6.1 Recommendations

Borehole radar technology has the potential to image and characterize the near well region of production wells in specific environments. However, the technical challenges of implementing a radar tool have not been addressed in this thesis, the design of a borehole radar antenna that can work as a permanent sensor is the main challenge for an implementation of this technology.

In favorable conditions, i.e. low electrical conductivity of the formation water, radar measurements can be used to improve well control strategies and to constrain reservoir models with semi-continuous monitoring data. Suitable oilfield environments are thin oil rims and heavy oil reservoirs produced with steam assisted gravity drainage. In these types of reservoirs the radar investigation depth fits the requirements for front detection.

Nevertheless, the use of this technology is recommended in geological or production scenarios where irregular flow fronts are expected to breakthrough in localized segments of the well. The added value of implementing a potential radar sensor is proportional to the need of monitoring phenomena that can be mitigated through proper and timely control. Irregular fronts develop along the wellbore, for example due to permeability differences, sedimentary or stratigraphic compartmentalization, different strength of the aquifer/gas-cap pressure, pressure drop along the completion due to friction. These conditions justify the use of additional sensing technologies.

Additional laboratory experiments under high pressure and temperature condition are recommended to study the EM wave propagation under conditions closer to the reservoir. Then a field case study should be taken in consideration. A borehole radar wireline tool could be first used as a prototype. Consequently, in case of successful results, a design for a permanent sensor including application required for the well completion should be realized.

Bibliography

- Addiego-Guevara, E. A., & Jackson, M. D. 2008. Insurance Value of Intelligent Well Technology against Reservoir Uncertainty. Paper SPE 113918 presented at the SPE/DOE Symposium on Improved Oil Recovery, Tulsa, Oklahoma, USA, 19-23 April.
- Aggrey, G. H., Davies, D. R., & Skarsholt, L. T. 2007. A Novel Approach of Detecting Water Influx Time in Multizone and Multilateral Completions Using Real-Time Downhole Pressure Data. Paper SPE 105374 presented at the 15th SPE Middle East Oil & Gas Show and Conference, Kingdom of Bahrain, 11-14 March.
- al Hagrey, S. A. 2004. GPR application for mapping toluene infiltration in a heterogeneous sand model. *Journal of Environmental and Engineering Geophysics*, **9**(2), 79–85.
- Al-Khelaiwi, F. T., Birchenko, V. M., Konopczynski, M. R., & Davies, D. R. 2008. Advanced Wells: A Comprehensive Approach to the Selection between Passive and Active Inflow Control Completions. Paper IPTC 12145 presented at the International Petroleum Technology Conference, Kuala Lumpur, Malaysia, 3-5 December.
- Almutairi, F. H., & Davies, D. R. 2008. Detection of Scale Deposition Using Distributed Temperature Sensing. Paper SPE 113595 presented at the SPE International Oilfield Scale Conference, Aberdeen, UK, 28-29 May.
- Annan, A. P. 2005a. *Hydrogeophysics*. Springer. Chap. GPR methods for hydrogeological studies, pages 185–213.
- Annan, A. P. 2005b. *Near Surface Geophysics*. Society of Exploration Geophysics. Chap. Ground Penetrating Radar, pages 357–438.

- Archie, G. E. 1942. The electrical resistivity log as an aid in determining some reservoir characteristics. *Transactions of the American Institute of Mining and Metallurgical Engineers*, **146**, 54–61.
- Asprion, U., & Aigner, T. 1997. Aquifer architecture analysis using ground-penetrating radar: Triassic and Quaternary examples (S Germany). *Environmental Geology*, **31**(1-2), 66–75.
- Aziz, K., & Settari, A. 1979. *Petroleum Reservoir Simulations*. Applied Science Publishers.
- Bachrach, R., Tura, A., & Wilkinson, D. 2008. Introduction to this special section: Permanent monitoring, smart oil fields, and reservoir surveillance. *The Leading Edge*, **27**(12), 1614–1614.
- Bano, M., Loeffler, O., & Girard, J. F. 2009. Ground penetrating radar imaging and time-domain modelling of the infiltration of diesel fuel in a sandbox experiment. *Comptes Rendus Geoscience*, **341**(10-11), 846–858.
- Barnes, A. E. 2007. A tutorial on complex seismic trace analysis. *Geophysics*, **72**(6), 33–43.
- Beamish, D., & Peart, R. J. 1998. Electrokinetic geophysics - a review. *Terra Nova*, **10**(1), 48–55.
- Bernabe, Y. 1998. Streaming potential in heterogeneous networks. *Journal of Geophysical Research-Solid Earth*, **103**(B9), 20827–20841.
- Biegert, E., Ferguson, J., & Li, X. 2008. 4D gravity monitoring — Introduction. *Geophysics*, **73**(6), WA1–WA2.
- Birchak, J. R., Gardener, C. G., Hipp, J. E., & Victor, J. M. 1974. High dielectric constant microwave probes for sensing soil-moisture. *Proceedings of the IEEE*, **62**(1), 93–98.
- Bradford, J. H., McNamara, J. P., Bowden, W., & Gooseff, M. N. 2005. Measuring thaw depth beneath peat-lined arctic streams using ground-penetrating radar. *Hydrological Processes*, **19**(14), 2689–2699.
- Bradford, J. H., Clement, W. P., & Barrash, W. 2009. Estimating porosity with ground-penetrating radar reflection tomography: A controlled 3-D experiment at the Boise Hydrogeophysical Research Site. *Water Resources Research*, **45**(Feb).

- Brouwer, D. R., & Jansen, J. D. 2004. Dynamic Optimization of Water Flooding with Smart Wells Using Optimal Control Theory. *SPE Journal*, **9**(4), 391–402.
- Brouwer, D. R., Naevdal, G., Jansen, J. D., Vefring, E. H., & Kruijdsdijk, C. 2004. Improved Reservoir Management through Optimal Control and Continuous Model Updating. Paper SPE 90149 presented at the SPE Annual Technical Conference and Exhibition, Houston, Texas, 26-29 September.
- Bryant, I. D., Raghuraman, M. Y., Schroeder, R., Supp, M., Navarro, J., Raw, I., Smith, J., & Scaggs, M. 2004. Real-time monitoring and control of water influx to a horizontal well using advanced completion equipped with permanent sensors. *SPE Drilling & Completion*, **19**(4), 253–264.
- Butler, R. M. 1991. *Thermal Recovery of Oil and Bitumen*. Prentice Hall.
- Campbell, D. L., Lucius, J. E., Ellefsen, K. J., & DeszczPan, M. 1996. Monitoring of a controlled LNAPL spill using ground-penetrating radar. *Pages 511–517 of: Proceedings of the Symposium on the Application of Geophysics Engineering and Environmental Problems*. Keystone, USA, Apr 28 - May 2.
- Carlson, M. R. 2003. *Practical Reservoir Simulation*. PennWell.
- Cassidy, N. J. 2007. Evaluating LNAPL contamination using GPR signal attenuation analysis and dielectric property measurements: Practical implications for hydrological studies. *Journal of Contaminant Hydrology*, **94**(1-2), 49–75.
- Chanzy, A., Tarussov, A., Judge, A., & Bonn, F. 1996. Soil water content determination using a digital ground-penetrating radar. *Soil Science Society of America Journal*, **60**(5), 1318–1326.
- Charara, M., Manin, Y., Bacquet, C., & Delhomme, J. P. 2002. Use of permanent resistivity and transient-pressure measurement for time-lapse saturation mapping. *SPE Reservoir Evaluation & Engineering*, **5**(6), 472–479.
- Chen, M. Y., Raghuraman, B., Bryant, I., & Supp, M. 2006. Streaming Potential Applications in Oil Fields. Paper SPE 102106 presented at the SPE Annual Technical Conference and Exhibition, San Antonio, Texas, USA, 24-27 September.

- Chen, Y. H., & Oristaglio, M. L. 2002. A modeling study of borehole radar for oil-field applications. *Geophysics*, **67**(5), 1486–1494.
- Chew, W. C. 1995. *Waves and Fields in Inhomogeneous Media*. IEEE Press.
- Chute, F. S., Vermeulen, F. E., Cervenán, M. R., & McVea, F. J. 1979. Electrical properties of Athabasca oil sands. *Canadian Journal of Earth Science*, **16**(10), 2009–2021.
- Constable, S. 2010. Ten years of marine CSEM for hydrocarbon exploration. *Geophysics*, **75**(5), A67–A81.
- Cordua, K. S., Nielsen, L., Looms, M. C., Hansen, T. M., & Binley, A. 2009. Quantifying the influence of static-like errors in least-squares-based inversion and sequential simulation of cross-borehole ground penetrating radar data. *Journal of Applied Geophysics*, **68**(1, Sp. Iss. SI), 71–84.
- Crocco, L., Soldovieri, F., Millington, T., & Cassidy, N. J. 2010. Bistatic Tomographic GPR Imaging for Incipient Pipeline Leakage Evaluation. *Progress in Electromagnetics Research-Pier*, **101**, 307–321.
- Daniels, J. J., Roberts, R., & Vendl, M. 1995. Ground penetrating radar for the detection of liquid contaminants. *Journal of Applied Geophysics*, **33**(1-3), 195–207.
- Davies, D., Al-Khelaiwi, F., Muradov, K., Qing, Y., Rafiei, Y., Aggrey, G., & Al-Mutairi, F. 2008. Applications of permanent sensors for real-time well management. *The Leading Edge*, **27**(12), 1654–1661.
- Davies, J. L., & Annan, A. P. 1989. Ground-penetrating radar for high-resolution mapping of soil and rock stratigraphy. *Geophysical Prospecting*, **37**(5), 531–551.
- Day-Lewis, F. D., Lane, J. W., & Gorelick, S. M. 2006. Combined interpretation of radar, hydraulic, and tracer data from a fractured-rock aquifer near Mirror Lake, New Hampshire, USA. *Hydrogeology Journal*, **14**(1-2), 1–14.
- de Castro, D. L., & Branco, R. M. 2003. 4-D ground penetrating radar monitoring of a hydrocarbon leakage site in Fortaleza (Brazil) during its remediation process: a case history. *Journal of Applied Geophysics*, **54**(1-2), 127–144.
- Deiana, R., Cassiani, G., Villa, A., Bagliani, A., & Bruno, V. 2008. Calibration of a vadose zone model using water injection monitored by GPR and electrical resistance tomography. *Vadose Zone Journal*, **7**(1), 215–226.

- Drakeley, B. K., Johansen, E. S., Zisk, E. J., & Bostick, F.X. 2006. In-Well Optical Sensing - State of the Art Applications and Future Direction for Increasing Value in Production Optimization Systems. Paper SPE 99696 presented at the SPE Intelligent Energy Conference and Exhibition, Amsterdam, The Netherlands, 11-13 April.
- Ebadi, F., & Davies, D. R. 2006. Should Proactive or Reactive Control Be Chosen for Intelligent Well Management? Paper SPE 99929 presented at the Intelligent Energy Conference and Exhibition, Amsterdam, The Netherlands, 11-13 April.
- Ebihara, S., Nagoya, K., Abe, N., & Toida, M. 2006. Experimental studies for monitoring water-level by dipole-antenna array radar fixed in the subsurface. *Near Surface Geophysics*, **4**(2), 89–96.
- Eidsvik, J., Bhattacharjya, D., & Mukerji, T. 2008. Value of information of seismic amplitude and CSEM resistivity. *Geophysics*, **73**(4), R59–R69.
- Ellis, D. V., & Singer, J. M. 2007. *Well Logging for Earth Scientists*. Springer.
- Engdahl, N. B., Weissmann, G. S., & Bonal, N. D. 2010. An integrated approach to shallow aquifer characterization: combining geophysics and geostatistics. *Computational Geosciences*, **14**(2), 217–229.
- Fagerlund, F., & Heinson, G. 2003. Detecting subsurface groundwater flow in fractured rock using self-potential (SP) methods. *Environmental Geology*, **43**(7), 782–794.
- Gaffney, C. 2008. Detecting trends in the prediction of the buried past: A review of geophysical techniques in archaeology. *Archaeometry*, **50**(Part 2), 313–336.
- Galagedara, L. W., Parkin, G. W., Redman, J. D., von Bertoldi, P., & Endres, A. L. 2005. Field studies of the GPR ground wave method for estimating soil water content during irrigation and drainage. *Journal of Hydrology*, **301**(1-4), 182–197.
- Gao, C., Rajeswaren, T., & Nakagawa, E. 2007. A literature review of smart-well technology. Paper SPE 106011 presented at the SPE Production and Operations Symposium, Oklahoma City, Oklahoma, USA, 31 March - 3 April.
- Giannopoulos, A. 1997. The investigation of Transmission-Line Matrix and Finite-Difference Time-Domain Methods for the Forward Problem of

- Ground Penetrating Radar. Ph.D. thesis, Department of Electronic, University of York, UK.
- Giannopoulos, A. 2005. Modelling ground penetrating radar by GprMax. *Construction and Building Materials*, **19**(10), 755–762.
- Giannopoulos, A. 2008. An improved new implementation of complex frequency shifted PML for the FDTD method. *IEEE Transactions on Antennas and Propagation*, **56**(9), 2995–3000.
- Glandt, C. A. 2005. Reservoir Management Employing Smart Wells: A Review. *SPE Drilling and Completion*, **20**(4), 281–288.
- Gloaguen, E., Giroux, B., Marcotte, D., & Dimitrakopoulos, R. 2007. Pseudo-full-waveform inversion of borehole GPR data using stochastic tomography. *Geophysics*, **72**(5), J43–J51.
- Grandjean, G., & Gourry, J. C. 1996. GPR data processing for 3D fracture mapping in a marble quarry (Thassos, Greece). *Journal of Applied Geophysics*, **36**(1), 19–30.
- Grasmueck, M. 1996. 3-D ground-penetrating radar applied to fracture imaging in gneiss. *Geophysics*, **61**(4), 1050–1064.
- Gregoire, C., Joesten, P. K., & Lane, Jr., J. W. 2006. Use of borehole radar reflection logging to monitor steam-enhanced remediation in fractured limestone - results of numerical modelling and a field experiment. *Journal of Applied Geophysics*, **60**(1), 41–54.
- Gulamali, M. Y., Leinov, E., & Jackson, M. D. 2011. Self-potential anomalies induced by water injection into hydrocarbon reservoirs. *Geophysics*, **76**(4), F283–F292.
- Halabe, U. B. 1996. Ground penetrating radar for infrastructure condition assessment and geophysical applications: A review. *Pages 812–819 of: Proceedings of the 14th Structures Congress*. Chicago, USA, Apr 14-18.
- He, X. Q., Zhu, Z. Q., Liu, Q. Y., & Lu, G. Y. 2009. Review of GPR Rebar Detection. *Pages 804–813 of: Proceedings of the Progress in Electromagnetics Research Symposium*. Beijing, China, Mar 23-27.
- Heigl, W. M., & Peeters, M. 2005. Can we obtain invasion depth with directional borehole radar? *Petrophysics*, **46**(1), 52–61.

- Hoversten, G. M., Gritto, R., Washbourne, J., & Daley, T. 2003. Pressure and fluid saturation prediction in a multicomponent reservoir using combined seismic and electromagnetic imaging. *Geophysics*, **68**(5), 1580–1591.
- Huisman, J. A., Hubbard, S. S., Redman, J. D., & Annan, A. P. 2003. Measuring Soil Water Content with Ground Penetrating Radar: A Review. *Vadose Zone Journal*, **2**(4), 476–491.
- Huyer, W., & Neumaier, A. 1999. Global optimization by multilevel coordinate search. *Journal of Global Optimization*, **14**(4), 331–355.
- Hwang, Y. K., Endres, A. L., Piggott, S. D., & Parker, B. L. 2008. Long-term ground penetrating radar monitoring of a small volume DNAPL release in a natural groundwater flow field. *Journal of Contaminant Hydrology*, **97**(1–2), 1–12.
- Jaafar, M. Z., Vinogradov, J., & Jackson, M. D. 2009. Measurement of streaming potential coupling coefficient in sandstones saturated with high salinity NaCl brine. *Geophysical Research Letters*, **36**(NOV 10).
- Jack, I., & Singer, J. M. 1997. *Time-lapse seismic in reservoir management*. Society of Exploration Geophysicists.
- Jackson, M. D., Saunders, J. H., & Addiego-Guevara, E. A. 2005. Development and Application of New Downhole Technology to Detect Water Encroachment Toward Intelligent Wells. Paper SPE 97063 presented at the SPE Annual Technical Conference and Exhibition, Dallas, Texas, USA, 9–12 October.
- Jadoon, K. Z., Slob, E., Vanclooster, M., Vereecken, H., & Lambot, S. 2008. Uniqueness and stability analysis of hydrogeophysical inversion for time-lapse ground-penetrating radar estimates of shallow soil hydraulic properties. *Water Resources Research*, **44**(9).
- Jadoon, K. Z., Lambot, S., Slob, E. C., & Vereecken, H. 2011. Analysis of Horn Antenna Transfer Functions and Phase-Center Position for Modeling Off-Ground GPR. *Geoscience and Remote Sensing, IEEE Transactions on*, **PP**(99), 1–14.
- Jansen, J. D., Wagenvoort, A. M., Droppert, V. S., Daling, R., & Glandt, C. A. 2002. Smart Well Solutions for Thin Oil Rims: Inflow Switching and the Smart Stinger Completion. Paper SPE 77942 presented at the SPE Asia Pacific Oil and Gas Conference and Exhibition, Melbourne, Australia, 8–10 October.

- Jansen, J. D., Bosgra, O. H., & Van den Hof, P. M. J. 2008. Model-based control of multiphase flow in subsurface oil reservoirs. *Journal of Process and Control*, **18**(9, Sp. Iss. SI), 846–855.
- Jansen, J. D., Douma, S. D., Brouwer, D. R., van den Hof, P. M. J., Bosgra, O. H., & Heemink, A. W. 2009. Closed-loop reservoir management. Paper SPE 119098 presented at the SPE Reservoir Simulation Symposium, The Woodlands, Texas, USA, 2-4 February.
- Kharghoria, A., Zhang, F., Li, R., & Jalali, Y. 2002. Application of Distributed Electrical Measurements and Inflow Control in Horizontal Wells under Bottom-Water Drive. Paper SPE 78275 presented at the SPE 13th European Petroleum Conference, Aberdeen, Scotland, U.K., 29-31 October.
- Kim, C., Daniels, J. J., Guy, E. D., Radzevicius, S. J., & Holt, J. 2000. Residual hydrocarbons in a water saturated medium: a detection strategy using ground penetrating radar. *Environmental Geosciences*, **7**, 169–176.
- Kluth, E. L., P., Varnham M., Clowes, J. R., Kutlik, R. L., Crawley, C. M., & Heming, R. F. 2000. Advanced Sensor Infrastructure for Real Time Monitoring. Paper SPE 65152 presented at the SPE European Petroleum Conference, Paris, France, 24-25 October.
- Knight, R. 2001. Ground penetrating radar for environmental applications. *Annual Review of Earth and Planetary Science*, **29**, 229–255.
- Knoll, M. D., Knight, R. J., & Brown, E. 1994. Dielectric and hydro-geologic properties of sand-clay mixtures. *Pages 45–61 of: Proceedings of the 5th International Conference on GPR*.
- Kragas, T. K., Turnbull, B. F., & Francis, M. J. 2004. Permanent fiber-optic monitoring at northstar: Pressure/temperature system and data overview. *SPE Production & Facilities*, **19**(2), 86–93.
- Kuchuk, F., Zhan, L., Ma, S. M., Al-Shahri, A. M., Ramakrishnan, T.S., Altundas, Y., Bilgin, Zeybek, M., de Loubens, R., & Chugunov, N. 2010. Determination of In Situ Two-Phase Flow Properties Through Downhole Fluid Movement Monitoring. *SPE Reservoir Evaluation & Engineering*, **13**(4), 575–587.
- Kuroda, S., Jang, H., & Kim, H. J. 2009. Time-lapse borehole radar monitoring of an infiltration experiment in the vadose zone. *Journal of Applied Geophysics*, **67**(4, Sp. Iss. SI), 361–366.

- Lagarias, J. C., Reeds, J. A., Wright, M. H., & Wright, P. E. 1998. Convergence properties of the Nelder-Mead simplex method in low dimensions. *SIAM Journal on Optimization*, **9**(1), 112–147.
- Lambot, S., Slob, E. C., van den Bosch, I., Stockbroeckx, B., & Vanclooster, M. 2004. Modeling of ground-penetrating radar for accurate characterization of subsurface electric properties. *IEEE Transactions on Geoscience and Remote Sensing*, **42**(11), 2555–2568.
- Lambot, S., Antoine, M., Vanclooster, M., & Slob, E. C. 2006. Effect of soil roughness on the inversion of off-ground monostatic GPR signal for noninvasive quantification of soil properties. *Water Resources Research*, **42**(3).
- Lambot, S., Slob, E., & Vereecken, H. 2007. Fast evaluation of zero-offset Green's function for layered media with application to ground-penetrating radar. *Geophysical Research Letters*, **34**(21).
- Lambot, S., Slob, E., Chavarro, D., Lubczynski, M., & Vereecken, H. 2008a. Measuring soil surface water content in irrigated areas of southern Tunisia using full-waveform inversion of proximal GPR data. *Near Surface Geophysics*, **6**(6, Sp. Iss. SI), 403–410.
- Lambot, S., Slob, E., Vanclooster, M., Huisman, J. A., & Vereecken, H. 2008b. Hydrogeophysical techniques for site characterization and monitoring: Recent advances in ground-penetrating radar. *Pages 183–202 of: Soil Chemical Pollution, Risk Assessment, Remediation and Security*.
- Lambot, S., Slob, E., Rhebergen, J., Lopera, O., Jadoon, K. Z., & Vereecken, H. 2009. Remote Estimation of the Hydraulic Properties of a Sand Using Full-Waveform Integrated Hydrogeophysical Inversion of Time-Lapse, Off-Ground GPR Data. *Vadose Zone Journal*, **8**(3), 743–754.
- Lauritzen, J. E., Shahreyar, N., & Jacob, S. 2011. Selection Methodology for Passive, Active and Hybrid Inflow Control Completions. Paper SPE 21910 presented at the Offshore Technology Conference, Houston, Texas, USA, 2-5 May.
- Leucci, G., Persico, R., & Soldovieri, F. 2007. Detection of fractures from GPR data: the case history of the Cathedral of Otranto. *Journal of Geophysics and Engineering*, **4**(4), 452–461.

- Liu, J., Zollinger, D. G., & Lytton, R. L. 2008. Detection of Delamination in Concrete Pavements Using Ground-Coupled Ground-Penetrating Radar Technique. *Transportation Research Record*, 68–77.
- Liu, S. X., Sato, M., & Takahashi, K. 2004. Application of borehole radar for subsurface physical measurement. *Journal of Geophysics and Engineering*, **1**(3), 221–227.
- M., Zumberge, Alnes, H., Eiken, O., Sasagawa, G., & Stenvold, T. 2008. Precision of seafloor gravity and pressure measurements for reservoir monitoring. *Geophysics*, **73**(6), WA133–WA141.
- Mason, I. M., Bray, A. J., Sindle, T. G., Simmat, C. M., & Cloete, J. H. 2008. The effect of conduction on VHF radar images shot in water-filled boreholes. *IEEE Geoscience and Remote Sensing Letters*, **5**(2), 304–307.
- Meles, G. A., Van der Kruk, J., Greenhalgh, S. A., Ernst, J. R., Maurer, H., & Green, A. G. 2010. A New Vector Waveform Inversion Algorithm for Simultaneous Updating of Conductivity and Permittivity Parameters From Combination Crosshole/Borehole-to-Surface GPR Data. *IEEE Transactions on Geoscience and Remote Sensing*, **48**(12).
- Michalski, K. A., & Mosig, J. R. 1997. Multilayered media Green's functions in integral equation formulations. *IEEE Transactions on Antennas and Propagation*, **45**(3), 508–519.
- Minet, J., Lambot, S., Slob, E. C., & Vanclooster, M. 2010. Soil Surface Water Content Estimation by Full-Waveform GPR Signal Inversion in the Presence of Thin Layers. *IEEE Transactions on Geoscience and remote sensing*, **48**(3, Part 1), 1138–1150.
- Miorali, M., Slob, E., & Arts, R. 2011. A feasibility study of borehole radar as permanent downhole sensor. *Geophysical Prospecting*, **59**(1), 120–131.
- Miorali, M., Zhou, F., Slob, E., & Arts, R. 2011. Coupling ground penetrating radar and fluid flow modeling for oilfield monitoring applications. *Geophysics*, **76**(3), A21–A25.
- Miorali, M., Slob, E., & Arts, R. 2011. *GPR monitoring of oil displacement by waterflooding: A laboratory study*. Submitted to Geophysics.
- Moghadas, D., Andre, F., Slob, E. C., Vereecken, H., & Lambot, S. 2010. Joint full-waveform analysis of off-ground zero-offset ground penetrating

- radar and electromagnetic induction synthetic data for estimating soil electrical properties. *Geophysical Journal International*, **182**(3), 1267–1278.
- Nadri Pari, M., & Kabir, A. H. 2009. Smar well- Benefit, Types of Sensors, Challenges, Economic Consideration, and Application in Fractured Reservoir. Paper SPE 126093 presented at the SPE Saudi Arabia Technical Symposium and Exhibition, Alkhobar, Saud Arabia, 9-11 May.
- Noon, D. A., Stickley, G. F., & Longstaff, D. 1998. A frequency-independent characterization of GPR penetration and resolution performance. *Journal of Applied Geophysics*, **40**, 127–137.
- Nyhavn, F., Vassenden, F., & Singstad, P. 2000. Reservoir Drainage With Downhole Permanent Monitoring and Control Systems: Real-Time Integration of Dynamic Reservoir Performance Data and Static Reservoir Model Improves Control Decisions. Paper SPE 62937 presented at the SPE Annual Technical Conference and Exhibition, Dallas, Texas, 1-4 October.
- Oden, C. P., Olhoeft, G. R., Wright, D. L., & Powers, M. H. 2008. Measuring the electrical properties of soil using a calibrated ground-coupled GPR system. *Vadose Zone Journal*, **7**(1), 171–183. General Assembly of the European-Geosciences-Union, Vienna, Austria, APR 02-07, 2006.
- Olhoeft, G. R., Smith, S., Hyslip, J. P., & Selig, E. T. 2004. GPR in railroad investigations. *Pages 635–638 of: Proceedings of the 10th International Conference on Ground Penetrating Radar*. Delft, Netherlands, June 21-24.
- Patriarca, C., Mahmoudzadeh, M. R., Lambot, S., & Slob, E. 2010. Influence of acquisition related uncertainties on ground penetrating radar inversion results. *In: Proceedings of the 13th International Conference on Ground Penetrating Radar*.
- Patriarca, C., Lambot, S., Mahmoudzadeh, M. R., Minet, J., & Slob, E. 2011. Reconstruction of sub-wavelength fractures and physical properties of masonry media using full-waveform inversion of proximal penetrating radar. *Journal of Applied Geophysics*, **74**(1), 26–37.
- Pettinelli, E., Burghignoli, P., Pisani, A. R., Ticconi, F., Galli, A., Vannaroni, G., & Bella, F. 2007. Electromagnetic propagation of GPR signals in Martian subsurface scenarios including material losses and scattering. *IEEE Transactions on Geoscience and Remote Sensing*, **45**(5, Part 1), 1271–1281.

- Plewes, L. A., & Hubbard, B. 2001. A review of the use of radio-echo sounding in glaciology. *Progress in Physical Geography*, **25**(2), 203–236.
- Raw, I., & Tenold, E. 2007. Achievements of Smart Well Operations: Completion case studies . Paper SPE 107117 presented at the SPE Europec/EAGE Annual Conference and Exhibition, London, UK, 11-14 June.
- Revil, A., Pezard, P. A., & Glover, P. W. J. 1999. Streaming potential in porous media 1. Theory of the zeta potential. *Journal of Geophysical Research-Solid Earth*, **104**(B9), 20021–20031.
- Robison, C. E. 1997. Overcoming the Challenges Associated With the Life-Cycle Management of Multilaterals Wells: Assessing Moves Towards the Intelligent Completion. Paper SPE 38497 presented at the Offshore Europe Conference, Aberdeen, UK, 9-12 September.
- Roth, K., Schulin, R., Fluhler, H., & Attinger, W. 1990. Calibration of time domain reflectometry for water-content measurements using a composite dielectric approach. *Water Resources Research*, **26**(10), 2267–2273.
- Saintenoy, A., Schneider, S., & Tucholka, P. 2008. Evaluating ground penetrating radar use for water infiltration monitoring. *Vadose Zone Journal*, **7**(1), 208–214.
- Sarma, P., Durlafsky, L. J., & Aziz, K. 2008. Kernel principal component analysis for efficient, differentiable parameterization of multipoint geostatistics. *Mathematical Geosciences*, **40**(1), 3–32.
- Sato, M., & Takayama, T. 2007. A novel directional borehole radar system using optical electric field sensors. *IEEE Transactions on Geoscience and Remote Sensing*, **45**(8), 2529–2535.
- Saunders, J. H., Jackson, M. D., & Pain, C. C. 2006. A new numerical model of electrokinetic potential response during hydrocarbon recovery. *Geophysical Research Letters*, **33**(15).
- Saunders, J. H., Jackson, M. D., & Pain, C. C. 2008. Fluid flow monitoring in oilfields using downhole measurements of electrokinetic potential. *Geophysics*, **73**(5), E165–E180.
- Schön, J. H. 1998. *Physical properties of rocks*. Pergamon. Chap. Electrical properties of rocks.

- Seleznev, N.V., Body, A., Habashy, T., & Luthi, S. 2004. Dielectric mixing laws for partially saturated carbonate rocks. *In: Proceedings of the SPWLA 45th Annual Logging Symposium.*
- Slater, L., & Comas, X. 2009. Ground Penetrating Radar: Theory and Applications. Elsevier. Chap. The contribution of Ground Penetrating Radar to water resource research, pages 203–246.
- Slob, E., & Fokkema, J. 2002. Coupling effects of two electric dipoles on an interface. *Radio Science*, **37**(5).
- Splajt, T., Ferrier, G., & Frostick, L. E. 2003. Application of ground penetrating radar in mapping and monitoring landfill sites. *Environmental Geology*, **44**(8), 963–967.
- Stenvold, T., Eiken, O., & Landrø, M. 2008. Gravimetric monitoring of gas-reservoir water influx — A combined flow- and gravity-modeling approach. *Geophysics*, **73**(6), WA123–WA131.
- Talley, J., Baker, G. S., Becker, M. W., & Beyrle, N. 2005. Four dimensional mapping of tracer channelization in subhorizontal bedrock fractures using surface ground penetrating radar. *Geophysical Research Letters*, **32**(4), 1–4.
- Taner, M. T., Koehler, F., & Sheriff, R. E. 1979. Complex seismic trace analysis. *Geophysics*, **44**(6), 1041–1063.
- Tsofias, G. P., & Becker, M. W. 2008. Ground-penetrating-radar response to fracture-fluid salinity: Why lower frequencies are favorable for resolving salinity changes. *Geophysics*, **73**(5), J25–J30.
- Tsofias, G. P., Halihan, T., & Sharp, J. M. 2001. Monitoring pumping test response in a fractured aquifer using ground-penetrating radar. *Water Resource Research*, **37**(5), 1221–1229.
- van Dongen, K. W. A., van Waard, R., & van der Baan, S. 2002. A Directional Borehole Radar System. *Subsurface Sensing Technologies and Applications*, **3**(4), 327–346.
- van Kleef, R., Hakvoort, R., Bhushan, V., Al-Khodhori, S., Boom, W., de Bruin, C., Babour, K., Chouzenoux, C., Delhomme, J. P., Manin, Y., Pohl, D., Rioufol, E., Charara, M., & Harb, R. 2001. Water Flood Monitoring in an Oman Carbonate Reservoir Using a Downhole Permanent

- Electrode Array. Paper SPE 68078 presented at the SPE Middle East Oil Show, Bahrain, 17-20 March.
- Vellidis, G., Smith, M. C., Thomas, D. L., & Asmussen, L. E. 1990. Detecting wetting front movement in a sandy soil with Ground-Penetrating Radar. *Transactions of the ASAE*, **33**(6), 1867–1874.
- Vinogradov, J., & Jackson, M. D. 2011. Multiphase streaming potential in sandstones saturated with gas/brine and oil/brine during drainage and imbibition. *Geophysical Research Letters*, **38**(JAN 7).
- Watts, G., Barkved, O., & Dickens, J. 2006. Seismic Surveillance in the Field of the Future. Paper SPE 99827 presented at the SPE Intelligent Energy Conference and Exhibition, Amsterdam, The Netherlands, 11-13 April.
- Webster, M., Richardson, S., Gabard-Cuoq, C., Fitzgerald, J. B., & Stephenson, K. E. 2006. Well surveillance with a permanent downhole multiphase flowmeter. *SPE Production & Operations*, **21**(3), 388–393. 2004 SPE Annual Technical Conference and Exhibition, Houston, TX, SEP 26-29, 2004.
- Wilson, V., Power, C., Giannopoulos, A., Gerhard, J., & Grant, G. 2009. DNAPL mapping by ground penetrating radar examined via numerical simulation. *Journal of Applied Geophysics*, **69**(3-4), 140–149.
- Zhan, L., Kuchuk, F., Al-Shahri, A. M., Ma, S. M., Ramakrishnan, T.S., Altundas, Y.B., Zeybek, M., Manin, Y., Tartaras, E., de Loubens, R., & Chugunov, N. 2010. Characterization of Reservoir Heterogeneity Through Fluid Movement Monitoring With Deep Electromagnetic and Pressure Measurements. *SPE Reservoir Evaluation & Engineering*, **13**(3), 509–522.
- Zhanxiang, H., Weibing, D., & Yuhong, L. 2007. Joint processing and integrated interpretation of EM and seismic data—an effective method for detecting complicated reservoir targets. *The Leading Edge*, **26**(3), 336–340.

Summary

The area of smart well technology, or closed-loop reservoir management, aims at enhancing oil recovery through a combination of monitoring and control. Monitoring is performed with a wide range of sensors deployed downhole or at the surface. These sensors allow for capturing changes in the reservoir conditions, mainly the fluid movement, at different resolutions. Downhole sensors give information of the fluid entering the well and sample only the region immediately adjacent to the well. Reservoir-imaging techniques are based on downhole or surface sensors and image large reservoir volumes typically with a resolution at the ten meter scale. Control is performed by installation of downhole flow control devices that can regulate the fluid inflow from the reservoir into the well ranging from on/off to a large number of settings. Combining monitoring and inflow technology allows using control strategies that mitigate undesired events such as premature water or gas breakthrough. Premature breakthrough of undesired fluids can reduce drastically the oil production and may cause the production well to be shut down.

Generally the near-well region in the order of ten meters is poorly imaged. However, in specific reservoir environments the monitoring of the near-well region is strongly required. For example, thin oil rim reservoirs usually have a thickness in the order of few tens of meters and are characterized by early water breakthrough in individual segments of the well. Steam Assisted Gravity Drainage (SAGD) is an enhanced oil recovery technique used in heavy oil reservoirs, where oil is extremely viscous and steam injection is used to facilitate the oil flow. A pair of horizontal wells is drilled into the reservoir only a few meters apart to allow for steam injection and oil production; however, the steam chamber growth and the oil flow are largely unknown. In both these examples a better understanding of the oil displacement process in the first ten meters from the production well could help preventing early breakthrough of unwanted fluids and allow for an implementation of more effective control strategies.

We have investigated radar technology as a potential tool able to cover the monitoring requirements needed in specific oilfield environments. This feasibility study was carried out through numerical modeling and laboratory experiments.

Through the numerical simulations we conclude that a borehole radar system can be used as a monitoring tool to probe the near-well region of several meters. The main constraint is the formation water electrical conductivity; high conductivity makes attenuation and phase distortion too high for wave propagation. Water/steam front reflections are detectable in low conductivity reservoirs ($\sigma < 0.02$ S/m). A system performance above 80 dB is necessary to detect reflections in the range of 10 m (chapters 2-3).

Additional reservoir constraints are given by a high degree of time-lapse heterogeneity changes of the EM properties and the length of the transition zone from oil to water bearing rocks. The effects of changes in the reservoir can be solved by increasing the data acquisition frequency relative to the rate of the local temporal changes. A gradual transition zone reduces the water reflections, which are not detectable when the transition is in the order of the dominant wavelength of the EM signal (chapters 2-3).

Numerical simulations were performed for both simple and complex geological scenarios. A sophisticated analysis was performed coupling electromagnetic and reservoir simulations. This allowed to evaluate the GPR performance in a realistic reservoir environment. Plotting the amplitude of the two-way-time reflected signal as the water advances toward the production well, where the radar system was located, appeared in clear up-dipping events (chapter 3).

The metal components of the wellbore casing can destructively interfere with the signal emitted by the radar sensor; however a high dielectric medium around the sensor can increase the amplitude of the reflected signal and overcome the interference problem (chapter 2).

Through the laboratory experiments we conclude general considerations on the GPR ability in monitoring oil displacement process governed by water. Water was injected in a meter-scale sand box and all the water flooding experiments presented similar characteristics. As for the modeling results, the amplitude of the two-way-time reflected signal as a function of the experiment time resulted in up-dipping events ascribable to the water front advance. According to the initial water saturation and porosity distribution continuous down-dipping events were associated to the up-dipping ones, forming wedge-shaped reflection features. The monitoring of the flow reflection features could be supported by attribute analysis, in particular, instantaneous frequency demonstrated to be a powerful tool to enhance wedge-shaped events.

The analysis of the GPR data agreed with impedance measurements taken simultaneously during the water flooding experiments. The main limitation to the GPR monitoring potential is the electrical conductivity of the residual water. The experiments at a high salinity water injection showed a strong attenuation of the signal and a reduction of the resolution (chapter 4).

Through an analysis of measured and modeled GPR signal it was possible to take in consideration the effect of uncertainties on subsurface characterization through full-waveform inversion. Subsurface characterization through full-waveform inversion relies heavily on the accuracy with which the forward model represents the actual GPR-subsurface system. Model errors can propagate through the inversion procedure resulting in wrong parameter estimates. The relative errors in the measured Green's function are mainly determined by the antenna transfer functions uncertainties. Averaging over a large number of transfer function sets leads to a high-accuracy Green's function estimate from the data, which leads to small errors in the estimated parameters obtained from full-waveform inversion. Provided the measurement conditions are respected, the inversion experiment adequately reproduces the estimated parameters. As soon as the measurement conditions are not completely respected, e.g., presence of extraneous objects, inversion experiments indicated that the accuracy of the estimates improves when calibration measurements to determine the transfer functions are acquired as close as possible to the measurement location (chapter 5).

Samenvatting

Slimme boorgattechnologie, of gesloten-lus reservoir beheer, beoogt de olie productie te verbeteren door een combinatie van monitoren en regelen. Monitoren wordt gedaan met een grote verscheidenheid aan sensoren die in het boorgat of aan het oppervlak worden ingezet. Deze sensoren maken het mogelijk veranderingen in het reservoir, voornamelijk vloeistof stroming, op verschillende resoluties in kaart te brengen. Boorgatsensoren geven informatie over de vloeistof die het boorgat instroomt en ze bemonsteren alleen het gebied in de directe omgeving van het boorgat. Reservoir afbeeldingstechnieken zijn gebaseerd op boorgat of oppervlakte sensoren en maken afbeeldingen van reservoir volumes met typisch een resolutie in de orde van tien meter. De regeling geschiedt door de installatie van boorgat stroming controlerende kleppen waarmee de vloeistofstroming kan worden geregeld, variërend van aan/uit tot een groot aantal standen. Het combineren van monitoren en instroomregelingstechnologie maakt het vermijden van ongewenst vroege doorbraak van water of gas mogelijk. Deze ongewenste gebeurtenissen kunnen tot sterke vermindering van olieproductie leiden en het kan leiden tot het moeten sluiten van het boorgat.

Over het algemeen wordt het gebied van tien meter rondom het boorgat slecht afgebeeld. Echter, in specifieke reservoir omstandigheden is het afbeelden van dat gebied zeer noodzakelijk. Bijvoorbeeld olie reservoirs in lagen met een dikte van een of enkele tientallen meters worden gekarakteriseerd door vroege doorbraak van water in individuele segmenten van het boorgat. Stoom Ondersteunde Gravitatie Drainage (SOGD) is een verbeterde olie productiemethode die wordt toegepast in met zware olie gevulde reservoirs, waar de olie extreem viskeus is en stoominjectie wordt toegepast om de olie beter te laten stromen. Twee horizontale boorgaten worden op onderlinge afstand van enkele meters geboord in het reservoir zodat vanuit het ene boorgat stoom kan worden genjecteerd en met het andere de olie kan worden geproduceerd. Echter is de ontwikkeling van het stoom volume en de oliestroom grotendeels onbekend. Bij beide voorbeelden zou een beter be-

grip van de verplaatsing van de olie kunnen bijdragen aan het vermijden van het vroegtijdig doorbreken van ongewenste vloeistoffen en de implementatie toelaten van effectieve meeten regeltechnieken.

Wij hebben radartechnologie onderzocht als een potentieel gereedschap dat in staat is om te voldoen aan de vereisten t.a.v. monitoring in specifieke olievelden. Deze haalbaarheidsstudie werd uitgevoerd gebruikmakend van numerieke modelering en laboratoriumexperimenten.

Uit numerieke simulaties concluderen wij dat een boorgat radarsysteem kan worden gebruikt als een monitoring gereedschap waarmee het gebied van enkele meters rondom het boorgat in kaart gebracht kan worden. De belangrijkste randvoorwaarde is de elektrische geleidbaarheid van het water in de porieruimte van het gesteente; hoge geleidbaarheid leidt tot te hoge demping en faseverstoring voor golfvoortplanting. Reflecties van de water/stoom overgang zijn detecteerbaar in een reservoir met lage geleidbaarheid ($\sigma < 0.02$ S/m). Een prestatievermogen van meer dan 80 dB is nodig voor een systeem om reflecties op een afstand van 10 m te detecteren (hoofdstukken 2 en 3).

Extra beperkingen t.a.v. het reservoir komen van de hoge veranderingsgraad over de tijd in de heterogeniteit van de EM eigenschappen en de lengte van het overgangsgebied van olie- naar waterhoudende gesteentes. Het probleem van veranderingen in het reservoir kan worden ondervangen door de frequentie van de data-acquisitie op te voeren ten opzichte van de snelheid van locale veranderingen over de tijd. Geleidelijke overgangsgebieden leiden tot zwakkere reflecties, die niet meetbaar zijn wanneer de orde van grootte van de overgang gelijk is aan die van de dominante golflengte van het EM signaal (hoofdstuk 2-3).

Numerieke simulaties zijn uitgevoerd voor eenvoudige en complexe geologische scenario's. Ingewikkelde data analyse werd uitgevoerd waarbij elektromagnetische en reservoir simulaties werden gekoppeld. Deze analyse maakte het mogelijk de prestatie van de grondradar in een realistische reservoir omgeving te evalueren. De tweeweg looptijd van de reflecties aan het olie/water contact treden op als duidelijke omhoog hellende aankomsten wanneer het water steeds dichterbij de productieput stroomt (hoofdstuk 3).

De metaalcomponenten van de boorbehuizing kunnen destructief interfereren met het signaal, dat wordt uitgezonden door de radarsensor; een hoog dielektrisch medium rond de sensor kan de amplitude van het gereflecteerde signaal echter vergroten zodat het interferentieprobleem wordt ondervangen (hoofdstuk 2).

Uit de laboratoriumexperimenten trekken we algemene conclusies met betrekking tot het vermogen van GPR tot monitoring van het door water gestuurde olieverplaatsingsproces. Alle waterinstroomexperimenten laten

dezelfde karakteristieken zien. Het waterfront kan zichtbaar worden als omhoog of omhoog hellende aankomsten, met wigvormige kenmerken, afhankelijk van de initiale waterverzadiging en porositeit verdeling. Het monitoren van de aan de waterstroom gerelateerde reflectie kenmerken werd vergemakkelijkt door gebruik te maken van de zogenaamde attributen analyse. De instantane frequentie data bleek in het bijzonder een krachtig gereedschap te zijn, waarmee de wigvormige kenmerken werden versterkt. De analyse van de GPR data was in overeenstemming met de impedantiemeting die gelijktijdig met de waterinstroomexperimenten is uitgevoerd. De belangrijkste beperkingen voor de inzet van GPR voor monitoring is het elektrische geleidingsvermogen van het restwater. De experimenten voor waterinjectie met hoog zoutgehalte lieten een sterke signaaldemping zien en een reductie van de resolutie (hoofdstuk 4).

Op basis van de analyse van de gemeten en gemodelleerde GPR signalen was het mogelijk om het effect van onzekerheden op de karakterisering van de ondergrond door middel van volledige-golfvorm inversie in beschouwing te nemen. Karakterisering van de ondergrond door middel van volledige-golfvorm inversie steunt in hoge mate op de nauwkeurigheid, waarmee het voorwaartse model het werkelijke GPR-ondergrond systeem representeert. Modelfouten kunnen propageren door de inversieprocedure en verkeerde parameterschattingen tot gevolg hebben. De relatieve fouten in de gemeten Greense functies worden hoofdzakelijk bepaald door de onzekerheden in de overdrachtsfunctie van de antennes. Het middelen van een groot aantal verzamelingen van overdrachtsfuncties leidt tot een grote nauwkeurigheid in de uit de data geschatte Greense functie, hetgeen kleine fouten in de geschatte parameters in de volledige-golfvorm inversie tot gevolg heeft. Wanneer aan de experimentele condities wordt voldaan, reproduceert het inversie-experiment nauwkeurig de geschatte parameters. Wanneer niet volledig aan de experimentele condities wordt voldaan, bijvoorbeeld bij de aanwezigheid van externe objecten, laten de inversie-experimenten zien dat de nauwkeurigheid van de schattingen verbetert met de kwaliteit van de overdrachtsfuncties; deze moeten zo dicht mogelijk bij de locatie van de meting worden verkregen. (hoofdstuk 5)

Acknowledgements

These few pages of my thesis are for all the people who have supported me during my PhD and have shared with me this long experience.

Many thanks go to my promoters Rob Arts and Evert Slob. I thank you for the belief you gave me at the beginning and during all these years. I have appreciated very much all discussions with Rob and all the reviews to papers and this thesis. Many thanks go to Evert, I have experienced you as copromotor, friend and now also promotor! I could learn a lot during all our meetings and there could be much more to learn.

I am grateful to my committee members Wim Mulder, Cor van Kruisjdijk, Sebastien Lambot, Jan van der Kruk and Antonis Giannopoulos. Special thanks go to Sebastien and Antonis because I had the opportunity to work with them directly. I have appreciated the time spent by Sebastian explaining me the GPR model and the possibility to use the laboratory equipment in Louvain-la-Neuve. I am very grateful to Antonis for giving me the opportunity to spend few months in Edinburgh and for suggestions and explanations about GprMax.

Half of this thesis is based on laboratory measurements, which would have not been possible without the help of several people. Karel Heller was essential for the development of the experimental set up and during all the experimental activity. Moreover, I am very grateful to Kees van Beek and Suze-Anne Korteland for helping me with the electrical measurements.

I am very grateful for all colleagues that helped me directly to carry out my research and finally this thesis. I have to mention Andrea di Matteo for the introduction to matlab, Jürg Hunziker for various advices in matlab, latek and illustrator, Karel van Dalen for latex thesis template and the translation of the summery. My great thanks go to Feng Zhou, we have worked together on the numerical simulations and your dedication was extremely helpful for the publication of one paper and the development of this research. I am very thankful to Claudio Patriarca for discussion about laboratory measurements and for sharing his results in the study about the GPR uncertainty.

All the years spent in the university would have not been so pleasant without many colleagues: Elisa, Andrea, Michel, Claudio, Christiaan, Sanaz, Saskia, Roozbeh, Negar, Ali, Jürg, Mohsen, Gosia, Daniele, Panos, Marwan, Nihed, Menne, Hamidreza, Duddy, Pantelis, Mario, Karel, Daria, Araz, Joost, Niels, Carlos, Ralph, Deyan, Wiebke, Wieske, Mohammad, Amin, Narjes, Elham, Farzad, Alex, Alimzhan, Elmer, Patrick, Tristan, Dennis. I thank you for the enjoyable time during lunches, coffee breaks, conference, trips...

Many friends have kept me alive also outside the university and here I mention few of them: Fabian, you have been a great friend but let me clarify here in response to the preface of your thesis that waterpolo is not your sport! My dear housemates Gregorio and Aristidis, in the last months you have seen me in a stressed mood but we had great time before. The Indian community Shreyes, Sidd, Rajeev, Prem, Dushyant, Ashutosh, Venkat, the Greek community George, Panos, Petros, Kostas, native and adopted Italians, Giorgio, Barbara, Mario, Francesco, Martijn, Federica, Luca, Marcello, Piero, Giuseppe, Paolo, Olindo, Joel, all the Marcushof and Binnenhof people. There would be much more people to mention, hopefully I will meet you soon and I will thank you alive!

Finally, I am very grateful to my parents and my brother for their support in good and bad times. I would have never reached this point without your help. The last words are for Eva, I thank you for your love and understanding in all the difficult times.

Mattia Miorali
December 2011

About the authour

Mattia Miorali was born on November 17, 1980 in Milan, Italy. He finished his secondary education in 1999 at Liceo Scientifico Primo Levi in San Donato Milanese, Italy. He started a B.Sc in Geological Science and Geotechnology in October 1999 at the Università degli Studi Milano-Bicocca, where he graduated in February 2004. He received the M.Sc. in the same field from the same institute in April 2006. From December 2006 to July 2011 he was a PhD student in the section of Applied Geophysics and Petrophysics of the department of Geotechnology in Delft University of Technology. He was a visiting student at the Center of Wave Phenomena in Colorado School of Mines during spring 2009 and at the Edinburgh Parallel Computing Center (EPCC) during spring 2010. During his Ph.D. he took several post graduate courses at the Centre for Technical Geoscience (CTG) and he received the CTG Research School Certificate. Since August 2011, he has started working as a geophysicist with CGGVeritas.

Journal papers and conference proceedings

- Miorali, M., E. Slob, R. Arts. GPR monitoring of oil displacement by waterflooding: A laboratory study. *Geophysics*, (undergoing review).
- Miorali, M., F. Zhou, E. Slob, and R. Arts. Coupling GPR and fluid flow modeling for oilfield monitoring applications. *Geophysics*, 76(3): A21–A25. 2011.
- Miorali, M., E. Slob and R. Arts. GPR monitoring of oil displacement: A laboratory study. In *Proceedings of 73rd EAGE Conference and Exhibition*, Vienna, Austria, May 2011.
- Miorali, M., E. Slob, and R. Arts. A feasibility study of borehole radar as a permanent downhole sensor. *Geophysical Prospecting*, 59(1): 120–131. January 2011.

-
- Miorali, M., F. Zhou, E. Slob and R. Arts. Water front monitoring by ground penetrating radar technology. In *Proceedings of 80th SEG Annual International Meeting*, Denver, USA, October 2010.
 - Miorali, M., E. Slob and R. Arts. A controlled experiment for water front monitoring using GPR technology. In *Proceedings of XIII International Conference on Ground Penetrating Radar*, Lecce, Italy, June 2010.
 - Miorali, M., E. Slob and R. Arts. Borehole radar modeling for reservoir monitoring applications. In *Proceedings of 72nd EAGE Conference and Exhibition*, Barcelona, Spain, June 2010.
 - Miorali, M., E. Slob and R. Arts. Borehole radar measurements in shallow oilfield applications. In *Proceedings of 1st International Conference on Frontiers in Shallow Subsurface Technology*, Delft, January 2010.
 - Miorali, M., E. Slob and R. Arts. A modeling study of a borehole radar system as a permanent down-hole sensor. In *Proceedings of 79th SEG Annual International Meeting*, Houston, USA, October 2009.
 - Miorali, M., E. Slob and R. Arts. Feasibility of borehole radar measurements to monitor water/steam front in EOR applications. In *Proceedings of 71st EAGE Conference and Exhibition*, Amsterdam, The Netherlands, June 2009.
 - Miorali, M., E. Slob and R. Arts. Borehole radar measurements to detect steam/water breakthrough in individual horizontal well segments. In *Proceedings of SEG/EAGE Unconventional Resources Workshop*, Vancouver, Canada, September 2008.